
Unterschrift Betreuer



TECHNISCHE
UNIVERSITÄT
WIEN
Vienna University of Technology

DIPLOMARBEIT

Dissipative Few-Body Quantum Systems

Ausgeführt am
Atominstitut der Technischen Universität Wien
in Zusammenarbeit mit dem
Institute of Science and Technology Austria

unter der Anleitung von
Assistant Prof. Dr. rer. nat. Mikhail Lemeshko
und **Assistant Prof. Dr. rer. nat. Peter Rabl**

durch

Clemens Jochum, B.Sc.

Schlagergasse 1/3
1090 Wien

Wien, 6. November 2016

Unterschrift Student

Abstract

Within the scope of this thesis, we show that a driven-dissipative system with few ultracold atoms can exhibit dissipatively bound states, even if the atom-atom interaction is purely repulsive. This bond arises due to the dipole-dipole interaction, which is restricted to one of the lower electronic energy states, resulting in the distance-dependent coherent population trapping. The quality of this already established method of dissipative binding is improved and the application is extended to higher dimensions and a larger number of atoms. Here, we simulate two- and three-atom systems using an adapted approach to the Monte Carlo wave-function method and analyse the results. Finally, we examine the possibility of finding a setting allowing trimer states but prohibiting dimer states. In the context of open quantum systems, such a three-body bound states corresponds to the driven-dissipative analogue of a Borromean state. These states can be detected in modern experiments with dipolar and Rydberg-dressed ultracold atomic gases.

Kurzfassung

Im Rahmen dieser Diplomarbeit wird gezeigt, dass ein getrieben-dissipatives System mit wenigen ultrakalten Atomen zu einem dissipativ gebundenen Zustand führen kann, auch wenn die interatomare Wechselwirkung rein abstoßend ist. Diese Bindung entsteht aufgrund der Dipol-Dipol Wechselwirkung, die auf einen der elektronischen Grundzustände beschränkt ist. Mittels dieser Beschränkung kann erreicht werden, dass der kohärente Besetzungseinfang von der interatomaren Distanz abhängt. Die Güte dieser bereits etablierten dissipativen Bindungsmethode wurde im Laufe dieser Arbeit verbessert und auf eine höhere Anzahl von Atomen in höherdimensionalen optischen Fallen angewendet. In dieser Arbeit werden Zwei- und Drei-Atom Systeme mittels einer adaptierten Version der Monte Carlo Wave-Function Methode simuliert und die Ergebnisse analysiert. Schließlich wird die Möglichkeit eines Parameterbereichs, in dem Trimere gebildet werden können aber Dimere verhindert werden, diskutiert. Solch ein dreiatomiger Bindungszustand entspricht dem getrieben-dissipativen Analogon eines Borromäischen Zustands im Kontext offener Quantensysteme. Diese neuartigen Zustände können in modernen Quantenoptik-Experimenten mit dipolaren ultrakalten Quantengasen im Rydbergzustand nachgewiesen werden.

Acknowledgments

First, I want to express my sincere gratitude to Professor Mikhail Lemeshko for giving me the opportunity to work under his supervision and in his group at the Institute of Science and Technology Austria. Not only was I provided with an inspiring and productive working environment, but I also gained many insights into the world of academic research. I am thankful for his patience and for his scientific and moral support I continuously received during the many ups and downs of this thesis, which allowed me to finally finish my studies. I wish him success in his future scientific endeavors.

Furthermore, I would also like to thank Professor Peter Rabl for his support, his supervision, and for making this collaboration of the University of Technology and the Institute of Science and Technology Austria possible while keeping bureaucracy at a minimum.

My gratitude for many hours of pleasant company while working together belongs to all members of the Lemeshko group at the Institute of Science and Technology Austria, whose friendly and kind atmosphere made me feel immediately welcome.

Additionally, I want to express my special thanks to my colleague Dr. Jan Kaczmarczyk. His experienced advice whenever I got stuck on a programming problem was crucial to the success of this thesis. I wish him all the best in his new role as a father.

Creating this thesis was made possible by using many amazing open source projects, in particular the document preparation system \LaTeX and the plotting library “matplotlib” [1].

I would also like to express my heartfelt appreciation for the company of my friends, with many of whom I have come a long way since starting our physics studies together. Our undertakings, often spurred by our shared interests, never cease to excite me.

Finally, I am sincerely grateful for the support I received by my family and the encouragement to pursue my interests. I am especially thankful for the shelter my parents offered, whenever spirits were low and hunger was high.

Contents

1. Introduction	1
2. Model	3
2.1. Setup	3
2.2. Coherent Population Trapping	6
2.3. Dissipative Binding Mechanism	9
3. Numerical Methods	11
3.1. Monte Carlo Wave-Function Method	11
3.2. Adapted MCWF Method	14
3.3. Effective Dissipative Potentials for Two Atoms	16
3.4. Effective Dissipative Potentials for Three Atoms	20
4. Dissipative Two-Atom Systems	25
4.1. Choosing the Parameter Values	25
4.2. Simulation of the Two-Atom System	30
5. Dissipative Three-Atom Systems	35
5.1. Choosing the Parameter Values	35
5.2. Simulation of the Three-Atom System	40
6. Dissipative Borromean States	45
6.1. Borromean States	45
6.2. Finding Borromean Parameter Values	47
6.3. Simulation	48
7. Conclusion	51
A. Supplementary Theory	53
A.1. Rabi Oscillations	53
B. Caesium Data	57
C. Supplementary Results	59
List of Symbols and Abbreviations	69
List of Figures	70

List of Tables	73
Bibliography	77

1. Introduction

*„Begin at the beginning“, the King said, very gravely,
„and go on till you come to the end: then stop.“*

—Lewis Carroll, *Alice in Wonderland* [2]

In physics, dissipation usually presents an undesirable obstacle in the experimental realisation of coherent quantum systems, which physicists have to overcome. However, the tremendous progress in designing and controlling quantum setups during the last decades [3] has marked a change of paradigm by shifting the notion of dissipation from an adverse secondary effect to an important tool for the preparation of quantum states. This development gave rise to many novel ideas in form of theoretical proposals for dissipative preparation of quantum states [4–21]. In these proposals the interplay between dissipative and coherent dynamics is exploited in order to guide the system to a desired steady state. There have already been many successful experimental advances [22–29], defying the challenging nature of these complex setups.

More recently, dissipative binding mechanisms between atoms have been predicted in a variety of settings [30–33]. In this thesis the method proposed by Weimer and Lemeshko, where pairs of atoms in driven-dissipative open quantum systems can form dissipatively bound metastable states [32, 33], is investigated and improved. Additionally, the method is extended to three atoms in order to examine few-body effects in the dissipative setting. Although few- and many-body effects have been a well researched topic since Isaac Newton [34], even today most physicists still rely on the same approach: they assume additive pairwise interactions between the constituent particles and neglect intrinsic higher-order effects. By doing so, however, they ignore that effective many-particle interactions often play an essential role in the emergence of rich and complex behaviours in a large range of systems [35]. Notable three-body phenomena can be found in diverse systems such as ultracold atoms [36], atomic nuclei [37], colloids [38], and even neutron stars [39]. Condensed matter systems, which constitute a true playground for many-body physics, exhibit fascinating phases such as fractional quantum Hall states when three-atom interaction terms are included in the Hamiltonian [40–42]. Some of these novel phases even show promise to further the field of topological quantum computation [43].

In the context of controllable quantum systems, a wide variety of intrinsic few-body phenomena have already been studied [44–46], but one of the most intriguing manifestations of few-atom physics, the emergence of Borromean states,

has so far remained a topic of closed systems in an equilibrium setting [47, 48]. These trimer states appear in settings which do not allow any dimer states to form. In classical scenarios such as biology [49] and chemistry [50] they can be observed as Borromean rings [51], while in atomic physics they are known as Efimov states [52] and have been subject to successful experimental investigation [53–59]. The possibility of finding Borromean states in a dissipative setting using the aforementioned method by Leshchko and Weimer is treated within the scope of this thesis.

The examined systems and the underlying theory are introduced in the next chapter (Chap. 2), whereas computational and numerical methods used in this thesis are presented in Chap. 3. Two- and three-atom systems are examined separately in Chap. 4 and Chap. 5, respectively. Parameter regimes, where trimer states can emerge, but dimer states can not form, are investigated in Chap. 6. The final chapter (Chap. 7) gives a short summary of this thesis and an outlook for further development of this topic. Besides some supplementary results (Appendix C), the appendix contains important quantum optic theory (Appendix A) and reference data on caesium (Appendix B).

2. Model

*In One Dimension, did not a moving Point
produce a Line with two terminal points?
In Two Dimensions, did not a moving Line
produce a Square with four terminal points?*

—Edwin A. Abbott, *Flatland* [60]

In the scope of this thesis, several setups are examined and simulated. These setups vary in the number of their dimensions and in the number of the involved atoms. While initially a one-dimensional two-atomic system is used as a toy model, this system is extended to a two-dimensional two-atomic system, before finally a two-dimensional three-atomic system is investigated. In Sec. 2.1 the different systems are introduced and explained in detail. Furthermore, a thorough account of the individual atoms' electronic energy structure is given. The mechanism giving rise to the dissipative bond is treated in Sec. 2.3. Whereas a description of some of the theoretical aspects, which are crucial for this mechanism, is included in Sec. 2.2 and in Appendix A, the reader is referred to the literature for a more detailed account of the underlying theory [61–65].

2.1. Setup

Trapping Geometry

All systems considered in this thesis consist of two or three identical atoms, which are confined to one- or two-dimensional geometries by optical traps at ultracold temperatures. In order to study few-body phenomena, the densities of the proposed systems have to be such that only few-body processes play a significant role. This is realisable using the current experimental methods [66–72]. The atom species was chosen to be caesium, whose relevant properties can be seen in Appendix B. The advantage of choosing caesium atoms is their popularity within the experimental few-body physics community [53, 55–59].

The novel dynamics of the proposed systems emerge due to several different effects, which are induced by laser excitation of the atoms. The atoms' electronic transitions are driven by counterpropagating laser beams resulting in coherent population trapping (CPT), a similar effect to the well-known electromagnetically induced transparency (EIT [61]), which is the main mechanism exploited in

this thesis and which will be explained in detail in Sec. 2.2. Another consequence of this laser irradiation is that the atoms are provided with an electric dipole moment d , if the valence electron is in a certain state. Additionally, a weak electric field aligns the induced electric dipole moments parallel to each other and perpendicular to the trapping plane guaranteeing that the dipole-dipole interaction between two atoms only depends on the set of interatomic distances $\{r_{ij}\}$. Together, these concurring effects yield the dissipative binding mechanism.

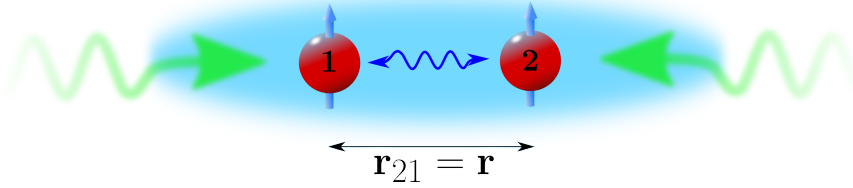


Figure 2.1.: Schematics of the one-dimensional two-atom system: two ultracold atoms (red) are confined by an appropriate one-dimensional optical trap (light blue) while counterpropagating laser beams (green) drive the atoms' electronic transitions. The atomic interaction is caused by the electric dipole moments (dark blue), which have parallel alignment due to a weak electric field.

A quasi-one-dimensional system with two atoms, which was used by Lemesko and Weimer [32, 33], is used as a simple model to explain the interatomic binding mechanism in Sec. 2.3. The setup of this system is shown in Fig. 2.1. Due to the simplicity of this constellation, the interatomic distance $r_{21} = r$ is sufficient to fully determine the relative configuration of the atoms.

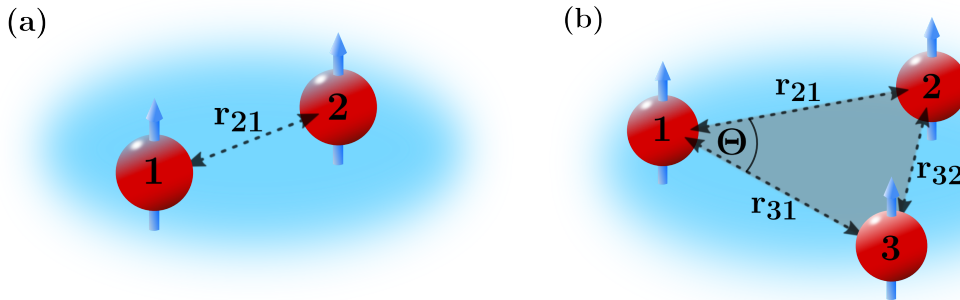


Figure 2.2.: (a) Representation of the two-atom system in two dimensions with interatomic distance $r_{21} = r$. (b) Representation of the three-atom system in two dimensions with indicated opening angle Θ and relative distances r_{21} , r_{31} , and r_{32} . The two-dimensional optical trap is indicated in light blue.

This model is expanded in Chap. 4, where the motion of the two atoms is now restricted to two dimensions as displayed in Fig. 2.2(a). By orienting the weak electric field, which aligns the dipole moments, perpendicular to the trapping plane, the atoms' interaction becomes invariant under rotations in the trapping plane. Consequently, only the interatomic distance $r_{21} = r$ is needed to completely characterise the arrangement of the atoms.

Finally, three identical ultracold atoms confined to a two-dimensional geometry by an optical dipole trap are considered in Chap. 5. This setup is schematically illustrated in Fig. 2.2(b). The relative distances between the three atoms are determined by r_{21} , r_{31} , and r_{23} or by r_{21} , r_{31} , and Θ . Applying the law of cosines to r_{21} , r_{31} , and Θ yields r_{23} :

$$r_{23}^2 = r_{21}^2 + r_{31}^2 - 2 \cdot r_{21} \cdot r_{31} \cdot \cos \Theta. \quad (2.1)$$

Electronic Level Structure

In this thesis the system's states will be referred to as follows: $|x\rangle_1$ for atom 1 being in state $|x\rangle$. In case of two atoms, state $|x, y\rangle = |x\rangle_1 \otimes |y\rangle_2$ denotes atom 1 being in state $|x\rangle$ and atom 2 being in state $|y\rangle$, whereas in the three-atom case $|x, y, z\rangle = |x\rangle_1 \otimes |y\rangle_2 \otimes |z\rangle_3$ indicates atoms 1, 2, and 3 being in states $|x\rangle$, $|y\rangle$, and $|z\rangle$, respectively. If an aspect of the level structure is being described which appears in each atom individually, then the notation $|x\rangle_a$ will be used and it is assumed that index a runs over all atoms in the system.

A graphical depiction of the level structure of one individual atom is shown in Fig. 2.3. Here, the two ground states, $|1\rangle_a$ and $|3\rangle_a$, are chosen as two fine or hyperfine components of the ground electronic state. State $|2\rangle_a$ is an electronically excited state. In the examined few-atom systems, which consist of caesium atoms, two different hyperfine components of the $6^2S_{1/2}$ state are chosen as states $|1\rangle_a$ and $|3\rangle_a$, whereas state $6^2P_{3/2}$ is chosen as state $|2\rangle_a$. For detailed information on the cesium D₂ line ($6^2S_{1/2} \rightarrow 6^2P_{3/2}$) see Tab. B.2 in Appendix B.

Due to the driving of the transitions, each atom's electronic energy level structure can be reduced to these three relevant states $|1\rangle_a$, $|2\rangle_a$, and $|3\rangle_a$, which compose a Λ -configuration. Additionally, a highly excited Rydberg state $|\text{Ry}\rangle_a$ is coupled to state $|1\rangle_a$ of the Λ -configuration, providing each atom in state $|1\rangle_a$ with the electric dipole moment d pointing perpendicular to the trapping plane in the weak electric field. Coupling to the environment provides the electronically excited state $|2\rangle_a$ with a decay of rate γ , which is assumed to be equal for both decays $|2\rangle_a \rightarrow |1\rangle_a$ and $|2\rangle_a \rightarrow |3\rangle_a$. Furthermore, interaction with three external electric fields gives rise to Rabi oscillations with Rabi frequencies Ω_{21} , Ω_{23} , and Ω_{Ry} . The concept of Rabi oscillations is explained in detail in Appendix A. It is assumed that the direct transition $|3\rangle_a \leftrightarrow |1\rangle_a$ between the ground states is electric dipole forbidden.

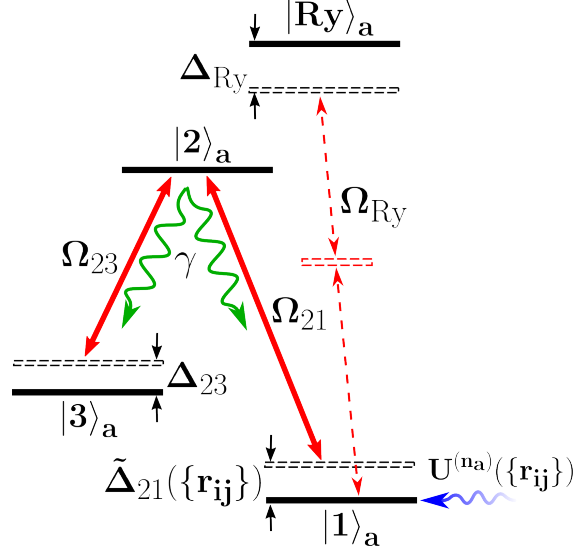


Figure 2.3.: The electronic energy structure of one of the atoms arranged in a Λ -system with all relevant system parameters. The combination of detuning Δ_{21} and dipole-dipole interaction $U^{(n_a)}(\{\mathbf{r}_{ij}\})$ yields a distance-dependent detuning $\tilde{\Delta}_{21}(\{\mathbf{r}_{ij}\}) = \Delta_{21} + U^{(n_a)}(\{\mathbf{r}_{ij}\})$.

While the two transitions $|1\rangle_a \leftrightarrow |2\rangle_a$ and $|3\rangle_a \leftrightarrow |2\rangle_a$ are driven with Rabi frequencies Ω_{21} and Ω_{23} and detunings Δ_{21} and Δ_{23} , respectively, state $|1\rangle_a$ is weakly coupled to the Rydberg state $|\text{Ry}\rangle_a$ using a two-photon transition in presence of a far-off-resonant field with Rabi frequency Ω_{Ry} [73–75]. For $\Delta_{\text{Ry}} \gg \Omega_{\text{Ry}}$ state $|\text{Ry}\rangle_a$ can be adiabatically eliminated and an effective dipole moment d is assigned to $|1\rangle_a$, while states $|2\rangle_a$ and $|3\rangle_a$ do not display any dipole moment. The strength of this dipole moment d is determined by the dipole moment d_0 of the highly-excited Rydberg state $|\text{Ry}\rangle_a$, Δ_{Ry} , and Ω_{Ry} [74]:

$$d = d_0 \left(\frac{\Omega_{\text{Ry}}}{\Delta_{\text{Ry}}} \right)^2. \quad (2.2)$$

This dipole moment generates a dipole-dipole interaction $U^{(n_a)}(\{r_{ij}\})$, where n_a stands for the number of involved atoms, if more than one atom is in state $|1\rangle_a$. Consequently the detuning of the transition $|1\rangle_a \leftrightarrow |2\rangle_a$ is rendered distance-dependent: $\tilde{\Delta}_{21}(\{r_{ij}\}) = \Delta_{21} + U^{(n_a)}(\{r_{ij}\})$.

2.2. Coherent Population Trapping

The phenomenon of CPT, which is caused by the coherent superposition of atomic states, is crucial to the dissipative binding method employed in this thesis. In the following the causes and the effect of CPT are examined [76].

A three-level atom interacting with two fields of frequencies ω_1 and ω_2 coupling the two lower states to a single excited state, as shown in Fig. 2.4, is considered. It is assumed that the transition $|a\rangle \leftrightarrow |b\rangle$ is electric dipole forbidden. The resulting electronic level structure is called Λ -configuration due to its shape.

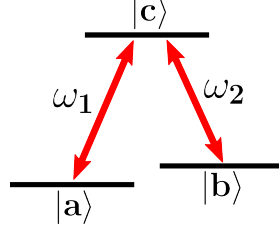


Figure 2.4.: Three-level atom in a Λ -configuration interacting with two resonant fields of frequencies ω_1 and ω_2 .

In the rotating-wave approximation the system's Hamiltonian \hat{H} writes as:

$$\begin{aligned} \hat{H} &= \hat{H}_0 + \hat{H}_I, \\ \text{with } \hat{H}_0 &= \hbar\omega_a |a\rangle \langle a| + \hbar\omega_b |b\rangle \langle b| + \hbar\omega_c |c\rangle \langle c| \\ \text{and } \hat{H}_I &= -\frac{\hbar}{2} (\Omega_1^* e^{i\omega_1 t} |a\rangle \langle c| + \Omega_1 e^{-i\omega_1 t} |c\rangle \langle a|) \\ &\quad -\frac{\hbar}{2} (\Omega_2^* e^{i\omega_2 t} |b\rangle \langle c| + \Omega_2 e^{-i\omega_2 t} |c\rangle \langle b|) . \end{aligned} \quad (2.3)$$

Here, the complex Rabi frequencies Ω_1 and Ω_2 are assumed to change slowly in time so that they can be treated as constant. These Rabi frequencies are associated with the coupling of the laser radiation with frequencies ω_1 and ω_2 to the atomic transitions $|a\rangle \leftrightarrow |c\rangle$ and $|b\rangle \leftrightarrow |c\rangle$, respectively. The driving of these transitions is assumed to be in resonance ($\omega_1 = \omega_c - \omega_a$ and $\omega_2 = \omega_c - \omega_b$). See Appendix A for a more detailed explanation of Rabi frequencies.

The state of the three-level atom can be written as $|\psi(t)\rangle = \alpha(t) |a\rangle + \beta(t) |b\rangle + \gamma(t) |c\rangle$, where $\alpha(t)$, $\beta(t)$, and $\gamma(t)$ are complex coefficients. In order to find a steady-state solution of the considered system, we insert $|\psi(t)\rangle$ in the well-known Schrödinger equation:

$$i\hbar \frac{\partial}{\partial t} |\psi(t)\rangle = \hat{H} |\psi(t)\rangle, \quad (2.4)$$

where the Planck constant is represented by \hbar . Doing so results in the following set of differential equations:

$$\begin{aligned}
 i\dot{\alpha}(t) &= \omega_a \alpha(t) - \frac{1}{2} \Omega_1^* e^{i\omega_1 t} \gamma(t) , \\
 i\dot{\beta}(t) &= \omega_b \beta(t) - \frac{1}{2} \Omega_2^* e^{i\omega_2 t} \gamma(t) , \\
 i\dot{\gamma}(t) &= \omega_c \beta(t) - \frac{1}{2} \Omega_1 e^{-i\omega_1 t} \alpha(t) - \frac{1}{2} \Omega_2 e^{-i\omega_2 t} \beta(t) .
 \end{aligned} \tag{2.5}$$

We introduce new complex coefficients in order to rewrite these equations:

$$\begin{aligned}
 A(t) &= \alpha(t) e^{i\omega_a t} , \\
 B(t) &= \beta(t) e^{i\omega_b t} , \\
 \Gamma(t) &= \gamma(t) e^{i\omega_c t} ,
 \end{aligned} \tag{2.6}$$

resulting in the simple set of differential equations seen in Eq. (2.7).

$$\begin{aligned}
 \dot{A}(t) &= \frac{i\Omega_1^*}{2} \Gamma(t) \\
 \dot{B}(t) &= \frac{i\Omega_2^*}{2} \Gamma(t) \\
 \dot{\Gamma}(t) &= \frac{i\Omega_1}{2} A(t) + \frac{i\Omega_2}{2} B(t)
 \end{aligned} \tag{2.7}$$

We set the time-derivatives of all coefficients to zero ($\dot{A}(t) = \dot{B}(t) = \dot{\Gamma}(t) = 0$) and use the normalisation condition ($|\alpha(t)|^2 + |\beta(t)|^2 + |\gamma(t)|^2 = 1$ and $|A(t)|^2 + |B(t)|^2 + |\Gamma(t)|^2 = 1$) to find the solution to a steady state. The resulting steady-state coefficients are:

$$\begin{aligned}
 A(t) &= \frac{\Omega_2}{\Omega} , \\
 B(t) &= -\frac{\Omega_1}{\Omega} , \\
 \Gamma(t) &= 0 .
 \end{aligned} \tag{2.8}$$

Here the variable Ω stands for $\sqrt{|\Omega_1|^2 + |\Omega_2|^2}$. Due to $\Gamma(t) = 0$ it is already obvious that the steady-state solution will not contain any population in the excited level $|c\rangle$. Using Eq. (2.6) and inserting the resulting coefficients into the original state $|\psi(t)\rangle$, we obtain the steady state:

$$|\psi_{\text{dark}}(t)\rangle = \frac{\Omega_2 e^{-i\omega_b t}}{\Omega} |a\rangle - \frac{\Omega_1 e^{-i\omega_c t}}{\Omega} |b\rangle , \tag{2.9}$$

where the global phase has been neglected without loss of generality. Because the lack of population in the excited state $|c\rangle$ renders emission and absorption of photons impossible, state $|\psi_{\text{dark}}(t)\rangle$ is called a dark state. The explanation for this phenomenon of coherent population trapping in the two lower levels is the destructive quantum interference of transitions $|a\rangle \leftrightarrow |c\rangle$ and $|b\rangle \leftrightarrow |c\rangle$. This means that, if the atom is prepared in the initial state:

$$|\psi_{\text{dark}}(0)\rangle = \frac{\Omega_2}{\Omega} |a\rangle - \frac{\Omega_1}{\Omega} |b\rangle , \quad (2.10)$$

the considered atom does not absorb any photons and becomes transparent to the incident light fields, even though these fields drive the transitions resonantly.

Thus, we have shown that, if an atom is prepared in a certain coherent superposition of states, it is possible to cancel any absorption even in the presence of resonant transitions. Once the atom is in the dark state $|\psi_{\text{dark}}(t)\rangle$, it remains in that state at all times t .

2.3. Dissipative Binding Mechanism

Usually, interatomic binding is caused by conservative interactions acting among electrons and nuclei. The resulting equilibrium configuration is determined by the minimum of the interaction potential. In this section we show that bonding can also occur due to interaction-induced coherent population trapping, which results from non-conservative forces. This dissipatively bound metastable state appears as a stationary state at a preordained interatomic distance. Remarkably, such a dissipatively bound state can arise even when the interactions between the atoms are purely repulsive.

In order to explain the dissipative binding mechanism, we assume a one-dimensional two-atom system, as shown in Fig. 2.1, with the atoms' electronic energy structure outlined in Fig. 2.3 . We simplify the system by assuming equal Rabi frequencies $\Omega_{21} = \Omega_{23}$ and a resonant transition $|3\rangle_a \leftrightarrow |2\rangle_a$ ($\Delta_{21} = 0$). The interaction-induced coherent population trapping, which is the integral aspect of the dissipative binding mechanism, emerges due to the combination of regular CPT in a Λ -system, as described in Sec. 2.2, and the distance-dependent detuning of transition $|1\rangle_a \leftrightarrow |2\rangle_a$. The condition for the stationary two-atom state $|\psi_{\text{grey}}^{(2)}\rangle$ is satisfied at the distance of minimal dissipation r_{min} . At this distance the two-atom dipole-dipole interaction $U^{(2)}(r_{21})$ approximately cancels out the detuning of transition $|1\rangle_a \leftrightarrow |2\rangle_a$: $U^{(2)}(r_{\text{min}}) + \Delta_{21} \approx 0$.

It is noted that due to the restriction of the dipole-dipole interaction to state $|1\rangle_a$ a true two-atom dark state $|\psi_{\text{dark}}^{(2)}\rangle$ corresponding to zero dissipation can not be achieved. Therefore, the obtained state is a so-called grey state $|\psi_{\text{grey}}^{(2)}\rangle$, where photon absorption is not totally suppressed, but significantly reduced at distance r_{min} .

Under this condition the two atoms are almost completely decoupled from photon absorption-emission thereby strongly increasing the probability of finding the atoms separated by distance r_{\min} . In the corpuscular approach, this can be explained by the photon scattering and the corresponding photon recoil due to which the atoms are randomly kicked around until they are in the two-atom grey state $|\psi_{\text{grey}}^{(2)}\rangle$, where there is almost no photon scattering. When the dipole-dipole interaction is strong enough to push the atoms apart, they end up in a brighter state, where they experience more photon kicks and are randomly kicked around again until they return to the grey state $|\psi_{\text{grey}}^{(2)}\rangle$ at distance r_{\min} . This metastable bond is continuously broken and formed by photon scattering and the dipole-dipole interaction. On average, however, there will be a clear peak in the two-body correlation function at distance r_{\min} . When treating the atoms as a wave-function, the leaking of population in the excited state $|2\rangle_a$ due to dissipation is minimised at r_{\min} , resulting in the aforementioned peak of the two-body correlation function. This confinement of the atoms corresponds to the formation of a dissipatively bound state.

The examined two-dimensional two- and three-atom systems, which have no restrictions on the parameter values, exhibit similar dynamics, but on a more complex level. By setting the parameters Ω_{21} , Ω_{23} , Δ_{21} , Δ_{23} , and d to fixed values the photon absorption rate of our system only depends on the interatomic distances $\{r_{ij}\}$. Different sets of parameter values then yield different distance-dependent behaviours of the photon absorption rate $V^{(n_a)}(\{r_{ij}\})$, which will be introduced in the next chapter. In Chaps. 4 and 5 we search for shapes of $V^{(n_a)}(\{r_{ij}\})$ that enhance probability of finding the atoms separated by r_{\min} the most.

3. Numerical Methods

Physics is mathematical not because we know so much about the physical world, but because we know so little; it is only its mathematical properties that we can discover.

—Bertrand Russell, *An Outline of Philosophy*[77]

Generally, the time evolution of a quantum system is determined by the initial state of the system and the appropriate quantum master equation, which is a set of differential equations for every element of the system's density matrix [78]. Due to the complexity and the high computational cost of numerically calculating the time evolution of the systems presented in Sec. 2.1, a more efficient numerical method is necessary. The numerical approach taken in this thesis is based on the Monte Carlo wave-function method (MCWF), which will be treated in Sec. 3.1. In Sec. 3.2 this stochastic method is developed further into an adapted MCWF technique, which was ultimately used to calculate time evolution in this thesis. The novelty of this adapted version is the use of effective dissipative potentials, which will be introduced in Secs. 3.3 and 3.4. The reader is referred to Appendix A and the established literature for more information on the theoretical background of quantum optics [61, 62], statistical physics [78], and quantum mechanics [63–65].

3.1. Monte Carlo Wave-Function Method

Under the assumption of weak coupling between the environment and the system (Born approximation) and the assumption of an environmental correlation time much shorter than the timescale of the system's evolution (Markov approximation), the time dependence of the system's reduced density operator $\hat{\rho}_S$ can be calculated by employing the following quantum master equation:

$$\frac{d\hat{\rho}_s}{dt} = -\frac{i}{\hbar} \left[\hat{H}_s, \hat{\rho}_s \right] + \mathcal{L}(\hat{\rho}_s) , \quad (3.1)$$

where \hbar is the reduced Planck constant and $\hat{\rho}_s$ and \hat{H}_s denote the reduced density operator and the reduced Hamiltonian, which only account for the dissipative system we want to examine. These operators are derived by tracing over the reservoir variables. By doing so the Lindblad superoperator $\mathcal{L}(\hat{\rho}_s)$ is obtained

simultaneously [79]. This Lindbladian term $\mathcal{L}(\hat{\rho}_s)$ is responsible for dissipative processes due to system-environment coupling, while unitary evolution of the system is determined by the system's Hamiltonian \hat{H}_s . Equation (3.1) is also known as the Kossakowski-Lindblad equation. A very general form of this Lindblad superoperator $\mathcal{L}(\hat{\rho}_s)$, which is valid for most quantum optics problems involving dissipation, writes as:

$$\mathcal{L}(\hat{\rho}_s) = \sum_n \gamma_n \left(\hat{c}_n \hat{\rho}_s \hat{c}_n^\dagger - \frac{1}{2} \{ \hat{c}_n^\dagger \hat{c}_n, \hat{\rho}_s \} \right). \quad (3.2)$$

Here, the operators \hat{c}_n correspond to the jump operators of the system's decay channels and γ_n are the respective decay rates. In this thesis the jump operators \hat{c}_n represent spontaneous emission of a photon.

Solving this quantum master equation of a system with N states involves calculations with the density matrix ρ , which contains $N \times N$ terms. For example, the density matrix ρ_s of the system examined in Chap. 5 contains $27 \times 27 = 729$ elements only considering the electronic energy structure. In order to describe the time evolution of such a dissipative system more efficiently, the Monte Carlo wave-function method (MCWF) developed by K. Mølmer, Y. Castin, and J. Dalibard [80, 81] is an excellent candidate. The application of the MCWF method, which is mathematically equivalent to solving the master equation [81], only involves the wave-function, which is described by N instead of $N \times N$ terms. Therefore, the MCWF method is computationally preferable to the density-matrix treatment for any system with a number of states larger than one ($N \ll N \times N$). Thus, applying the MCWF method is a great way of avoiding costly computation when calculating the time evolution of the systems considered in this thesis.

The integral steps of the MCWF method are applied to a generic system in the following. Assuming an initial state of the system $|\psi(t)\rangle$ at time t , we want to evolve this wave-function in time by a time increment δt and obtain the final state $|\psi'(t + \delta t)\rangle$. At first we calculate an intermediary state $|\psi'(t + \delta t)\rangle$, which is obtained by evolving state $|\psi(t)\rangle$ using the non-Hermitian Hamiltonian \hat{H} with quantum jump operators \hat{c}_n [81]:

$$\hat{H} = \hat{H}_s - \frac{i\hbar}{2} \sum_n \gamma_n \hat{c}_n^\dagger \hat{c}_n. \quad (3.3)$$

We calculate $|\psi'(t + \delta t)\rangle$ using the series expansion of the time evolution operator. By choosing δt sufficiently small, the terms of order $\mathcal{O}(\delta t^2)$ and higher can be dropped:

$$|\psi'(t + \delta t)\rangle = \left(1 - \frac{i\hat{H}\delta t}{\hbar} + \mathcal{O}(\delta t^2) \right) |\psi(t)\rangle. \quad (3.4)$$

The second term on the right side of Eq. (3.3) is responsible for the decrease of population in the excited level. In case of the systems introduced in Sec. 2.1 this leads to the reduction of the wave-function wherever the condition for CPT is not satisfied. The square of the time-evolved state $|\psi'(t + \delta t)\rangle$ is given by:

$$\langle \psi'(t + \delta t) | \psi'(t + \delta t) \rangle = \langle \psi(t) | \left(\mathbb{1} + \frac{i\hat{H}^\dagger \delta t}{\hbar} \right) \left(\mathbb{1} - \frac{i\hat{H} \delta t}{\hbar} \right) | \psi(t) \rangle . \quad (3.5)$$

The following calculation shows that the wave-function $|\psi'(t + \delta t)\rangle$ is obviously not normalised:

$$\begin{aligned} \langle \psi'(t + \delta t) | \psi'(t + \delta t) \rangle &= 1 - \frac{i\delta t}{\hbar} \langle \psi(t) | \left(\hat{H} - \hat{H}^\dagger \right) | \psi(t) \rangle \\ &= 1 - \delta t \sum_n \langle \psi(t) | \gamma_n \hat{c}_n^\dagger \hat{c}_n | \psi(t) \rangle \\ &= 1 - \sum_n \delta p_n = 1 - \delta p \end{aligned} \quad (3.6)$$

$$\text{with } \delta p_n = \delta t \langle \psi(t) | \gamma_n \hat{c}_n^\dagger \hat{c}_n | \psi(t) \rangle \geq 0 .$$

A consequence of choosing the size of timestep δt so that this first-order calculation is valid and that the terms of order $\mathcal{O}(\delta t^2)$ and higher can be dropped is that $\langle \psi'(t + \delta t) | \psi'(t + \delta t) \rangle$ will be close to one and δp will be small ($\delta p \ll 1$).

After evolving state $|\psi(t)\rangle$ in time by an increment of δt , the possibility of a quantum jump is examined. Due to the stochastic nature of this step the MCWF method is considered to be part of the Monte Carlo methods. The probability of decay and thus of the wave-function collapsing to a final ground state is given by δp and depends on the amount of population in the excited state. The decision whether a quantum jump happens is done by generating a quasi-random number ϵ , which is uniformly distributed between 0 and 1. Then the generated number ϵ is compared to δp leading to two cases:

- $\epsilon < \delta p$: In this case a quantum jump happens. The new wave-function is then chosen among the different final states:

$$|\psi(t + \delta t)\rangle = \hat{c}_n |\psi(t)\rangle \cdot (\delta p_n / \delta p)^{-\frac{1}{2}} . \quad (3.7)$$

The quantum jump associated with operator \hat{c}_n occurs with a probability of $P_n = \delta p_n / \delta p$. Summing all probabilities P_n yields 1, because $\delta p = \sum_n \delta p_n$.

- $\epsilon > \delta p$: In this case, which will be the majority of the cases since $\delta p \ll 1$, no quantum jump occurs. The new normalised wave-function at $t + \delta t$ is calculated by:

$$|\psi(t + \delta t)\rangle = |\psi'(t + \delta t)\rangle \cdot (1 - \delta p)^{-\frac{1}{2}} . \quad (3.8)$$

After the stochastic step the obtained normalised wave-function $|\psi(t + \delta t)\rangle$ becomes the new initial wave-function and the procedure is repeated from the beginning.

The reader is referred to the publication “Monte Carlo wave-function in quantum optics” by K. Mølmer, Y. Castin, and J. Dalibard [81] for a detailed review of the MCWF method, of its equivalence to the master-equation treatment, and of its physical interpretation.

3.2. Adapted MCWF Method

The adapted Monte Carlo method, which will be introduced in this section, was developed in order to simulate the systems in Chaps. 4 and 5. This method is based on the MCWF method discussed in Sec. 3.1. While the MCWF method fully considers the inner electronic energy-level structure of the system, this aspect is integrated out in our approach. This is done by replacing the inner structure with the effective dissipative potential, which will be derived in Secs. 3.3 and 3.4 for two- and three-atom systems, respectively.

Replacing the internal level structure of a n_a -atom system with the effective dissipative potential $V_d^{(n_a)}(\{r_{ij}\})$ reduces the size of the Hilbert space by a factor of 3^{n_a} . Whether the kicks due to photon recoil are accounted for in reference to the center-of-mass frame or in reference to the laboratory frame is unimportant due to the stochastic nature of the photon scattering process. Assuming many photon scattering events the effect on the particle dynamics becomes equivalent in both frames. This enables a further size reduction of the Hilbert space after transforming to relative coordinates.

In the following our adapted MCWF method is applied to the quasi-one-dimensional system with two atoms presented in Sec. 2.1 in order to demonstrate the procedure step by step. The layout of the two-atom system can be seen in Fig. 2.1. Analogous to the MCWF method, our adapted method consists of two steps. First, the wave-function $|\psi(t)\rangle$ is propagated in time by a time increment of δt using the non-Hermitian Hamiltonian \hat{H} from Eq. 3.3 and replacing the dissipation term by the effective dissipative potential $V_d^{(2)}(\{r_{ij}\})$:

$$\hat{H} = \hat{H}_{\text{kin}} - \frac{i\hbar}{2} V_d^{(2)}(r) |r\rangle \langle r| . \quad (3.9)$$

Here, the Hamiltonian $\hat{H}_{\text{kin}} = \hat{H}_s$ contains the unitary evolution without the inner energy-level structure, i.e., the kinetic energy of the two atoms. Timestep δt is chosen sufficiently small in order to drop terms of order $\mathcal{O}(\delta t^2)$ and higher. The time-evolved state $|\psi'(t + \delta t)\rangle$, which is not normalised, then writes as:

$$|\psi'(t + \delta t)\rangle = \left[1 - \frac{i\delta t}{\hbar} \left(\hat{H}_{\text{kin}} - \frac{i\hbar}{2} V_d^{(2)}(r) |r\rangle \langle r| \right) \right] |\psi(t)\rangle . \quad (3.10)$$

The leaking of population in the excited level is accounted for by the second term on the right hand side in Eq. (3.9). The effect of this term is shown schematically in Fig. 3.1. This step is equivalent to the step in Eq. (3.4). After dropping terms of order $\mathcal{O}(\delta t^2)$ and higher, the calculation for the squared norm of the time-evolved state $|\psi'(t + \delta t)\rangle$ can be written as:

$$\langle \psi'(t + \delta t) | \psi'(t + \delta t) \rangle = 1 - \delta t \int V_d^{(2)}(r) |\langle r | \psi(t) \rangle|^2 dr = 1 - \delta p \quad (3.11)$$

$$\text{with } \delta p = \delta t \int V_d^{(2)}(r) |\langle r | \psi(t) \rangle|^2 dr \geq 0 . \quad (3.12)$$

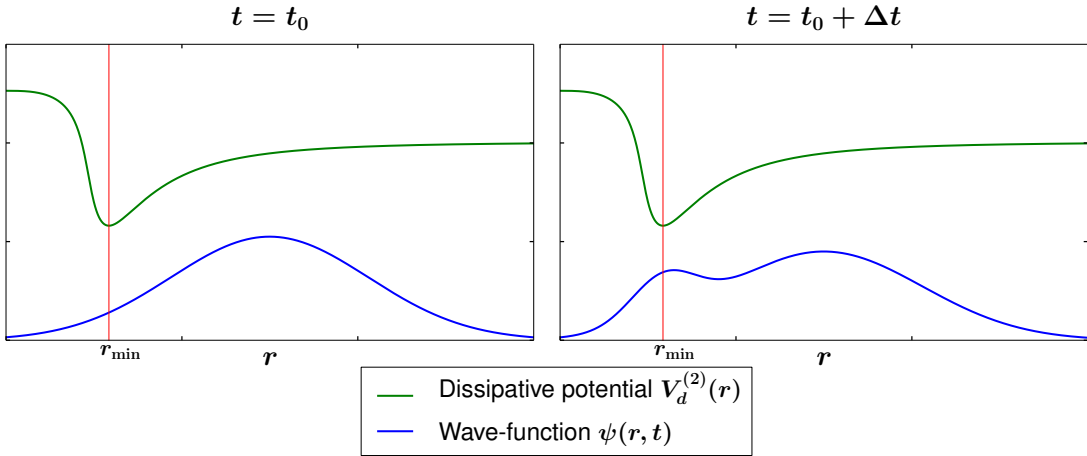


Figure 3.1.: The schematic outline of a two-atom wave-function in relative coordinates $\psi(r, t) = \langle r | \psi(t) \rangle$ is shown before and after some time Δt . Due to the distance-dependent population trapping discussed in Secs. 2.3 parts of the wave-function that are close to the dissipative minimum r_{min} will experience less decay and therefore less leaking of population and less photon scattering than parts further away from r_{min} . This is accounted for by Eq. (3.9) and accumulates over time, resulting in dissipative binding.

Because the effective dissipative potential $V_d^{(2)}(r)$ contains the photon absorption rate depending on the interatomic distance, integrating the wave-function over

this potential and multiplying the result by the increment δt yields a measure for the probability of decay. The dissipative potential, which corresponds to the dissipation rate at each distance, can not be negative ($V_d^{(2)}(r) \geq 0$).

Analogous to Sec. 3.1, in the second step a pseudo-random number ϵ distributed uniformly between 0 and 1 is generated and compared to δp :

- $\epsilon < \delta p$: In this case, no decay is happening. The majority of the time this case will occur, because of $\delta p \ll 1$.
- $\epsilon > \delta p$: In this case, decay occurs. A spontaneous photon is emitted. Because the energy-level structure is integrated out in this approach, the only consequence in this case is a momentum change of the wave-function due to the photon recoil. The emitting atom and the direction of the photon kick are chosen at random. The necessary optical properties of the transition are viewed in Tab. B.2 of Appendix B.

After this step, the wave-function is normalised according to Eq. (3.13) and the procedure is repeated from the beginning.

$$|\psi(t + \delta t)\rangle = |\psi'(t + \delta t)\rangle \cdot (1 - \delta p)^{-\frac{1}{2}} \quad (3.13)$$

It is important to note that while the dipole-dipole interaction $U^{(n_a)}(r)$ has an effect on the dissipation rate and therefore on the dissipative potential $V_d^{(n_a)}(r)$, it also exerts a force on the atoms by shifting the energy of state $|1\rangle_a$. This effect is not considered in the adapted MCWF algorithm, because it has no significant effect at the observed binding length scales.

The derivations of the dissipative potentials for two- and three-atom systems necessary for this algorithm are shown in the next sections.

3.3. Effective Dissipative Potentials for Two Atoms

After transforming to a suitable rotating frame and applying the rotating wave approximation, the unitary two-atom Hamiltonian $\hat{H}_0^{(2)}$, which does not account for decay, reads as:

$$\hat{H}_0^{(2)} = \hat{H}_{\text{kin}}^{(2)} + \hat{H}_{\text{int}}^{(2)} , \quad (3.14)$$

$$\text{with } \hat{H}_{\text{kin}}^{(2)} = \sum_{a=1,2} \sum_{\mathbf{k}} \frac{\hbar^2 \hat{\mathbf{k}}_a^2}{2m} |\mathbf{k}\rangle_a \langle \mathbf{k}|_a , \quad (3.15)$$

$$\begin{aligned}
 \text{and } \hat{H}_{\text{int}}^{(2)} = & U^{(2)}(|\hat{\mathbf{r}}_2 - \hat{\mathbf{r}}_1|) |1, 1\rangle \langle 1, 1| - \hbar \sum_{a=1,2} \left[\Delta_{21} |1\rangle_a \langle 1|_a \right. \\
 & + \Delta_{23} |3\rangle_a \langle 3|_a + \frac{\Omega_{21}}{2} (|2\rangle_a \langle 1|_a + |1\rangle_a \langle 2|_a) \\
 & \left. + \frac{\Omega_{23}}{2} (|2\rangle_a \langle 3|_a + |3\rangle_a \langle 2|_a) \right], \tag{3.16}
 \end{aligned}$$

where \hbar is the reduced Planck constant and m is the mass of caesium (see Tab. B.1 in Appendix B for relevant data on caesium). The wave vector operator $\hat{\mathbf{k}}_a$ and the position operator $\hat{\mathbf{r}}_a$ are both two-dimensional vector operators, which only act on atom a . The summation in Eq. (3.15) runs over all allowed values of wave-vector \mathbf{k} . Hamiltonian $\hat{H}_{\text{int}}^{(2)}$ describes the interactions of the atoms with each other and with the external laser fields. All these interactions are schematically shown in Fig. 3.2.

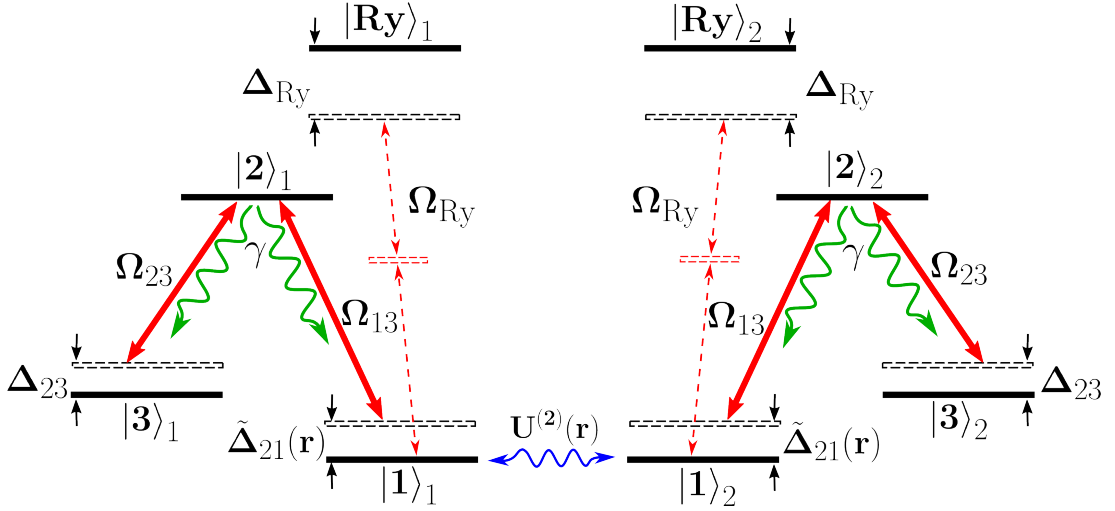


Figure 3.2.: The electronic energy structure of the two-atom system. The combination of detuning Δ_{21} and dipole-dipole interaction $U^{(2)}(r)$ yields a distance-dependent detuning $\tilde{\Delta}_{21}(r) = \Delta_{21} + U^{(2)}(r)$.

Inserting the Hamiltonian $\hat{H}_0^{(2)}$ as \hat{H}_s in Eq. (3.1) yields the quantum master equation for our system. In the Lindbladian term (Eq. (3.2)) the decay rates $\gamma_n = \gamma$ are without loss of generality assumed to be equal for all transitions. Furthermore, the jump operators $\hat{c}_n = \sum_{\mathbf{k}} |\mathbf{k} + \Delta\mathbf{k}_n\rangle_{a_n} \langle \mathbf{k}|_{a_n} \langle 2|_{a_n}$ are defined by the triple $(\Delta\mathbf{k}_n, i_n, a_n)$, where $\Delta\mathbf{k}_n$ determines energy and direction of the emitted photon and the indices $i_n = 1, 3$ and $a_n = 1, 2$ define the final states and the decaying atom, respectively [33].

Because solving the Lindblad equation for this system requires too much computational cost, as mentioned before, the time-evolution of the considered system was calculated using the adapted Monte Carlo method of Sec. 3.2. In the following the calculation of the effective dissipative two-atom potential $V_d^{(2)}(r)$, which is necessary for the adapted MCWF algorithm, is shown.

As the system is at ultracold temperatures complicating effects such as the Lamb shift can be ignored. Thus, kinetic part (Eq. 3.15) and interaction part (Eq. 3.16) of the Hamiltonian can be treated separately. Therefore, the jump operators \hat{c}_n in Eq. (3.1) reduce to $|j\rangle_a \langle 2|_a$, where index $j = 1, 3$ accounts for the two ground states. Additionally, the term $\hat{c}_n \hat{\rho} \hat{c}_n^\dagger$ of the sum in Eq. (3.2), i.e. the quantum jumps, can be neglected in the regime of weak dissipation, which is defined by the inequality in Eq. (3.17). By satisfying the inequality in Eq. (3.18) an EIT window and consequently a dissipation minimum are guaranteed to be observed when varying distance r .

$$\frac{\Omega_{2j}^2}{\gamma^2} \ll 1 \quad \text{with } j = 1, 3 \quad (3.17)$$

$$|\Delta_{2i}| \ll \frac{\Omega_{2j}^2}{\gamma} \quad \text{with } i = 1, 3 \text{ and } j = 1, 3 \quad (3.18)$$

Finally, the interatomic dipole-dipole interaction $U^{(2)}(r)$ between a pair of atoms caused by the effective dipole moment d (see Eq. (2.2)) is given by:

$$U^{(2)}(r) = \frac{d^2}{4\pi\epsilon_0 r^3} = \frac{\hbar\gamma}{\left(\frac{r}{r_0}\right)^3} \quad \text{with } r_0 = \left(\frac{d^2}{4\pi\epsilon_0 \hbar\gamma}\right)^{\frac{1}{3}}, \quad (3.19)$$

where ϵ_0 denotes the vacuum permittivity.

Now, that the two-body problem is fully formulated, the subsequent step is to obtain the composition of the two-atom grey state $|\psi_{\text{grey}}^{(2)}\rangle$ in order to calculate the photon absorption rate. Neglecting the quantum jumps allows for the introduction of an effective non-Hermitian Hamiltonian \hat{H}_{eff} [32, 33], thereby reducing the problem to the eigenproblem of H_{eff} and avoiding excessive computations:

$$\hat{H}_{\text{eff}}^{(2)} = \hat{H}_{\text{int}}^{(2)} - i\hat{V}_{\text{dis}}^{(2)} \quad (3.20)$$

$$\text{with } \hat{V}_{\text{dis}}^{(2)} = \frac{\hbar}{2} \sum_n \gamma_n \hat{c}_n^\dagger \hat{c}_n. \quad (3.21)$$

It is advantageous to construct a basis comprised of states $|i, i\rangle$ and symmetric and antisymmetric combinations of states $|i, j\rangle$ with $i \neq j$, where indices i and j run over the electronic energy levels 1, 2, 3. As the Hamiltonian \hat{H}_{eff} only connects states symmetric against particle exchange, states of

form $(|i, j\rangle - |j, i\rangle)/\sqrt{2}$ are decoupled from any possible excitation and therefore do not have to be considered. Therefore, a basis consisting of the six states $\{|1, 1\rangle, (|1, 2\rangle + |2, 1\rangle)/\sqrt{2}, (|1, 3\rangle + |3, 1\rangle)/\sqrt{2}, |2, 2\rangle, (|2, 3\rangle + |3, 2\rangle)/\sqrt{2}, |3, 3\rangle\}$ suffices to express the system's Hamiltonian in the matrix form of $H_{\text{eff}}^{(2)}$:

$$\frac{H_{\text{eff}}^{(2)}}{\hbar} = \begin{bmatrix} \frac{U^{(2)}}{\hbar} - 2\Delta_{21} & \frac{\Omega_{21}}{\sqrt{2}} & 0 & 0 & 0 & 0 \\ \frac{\Omega_{21}}{\sqrt{2}} & -\frac{i\gamma}{2} - \Delta_{21} & \frac{\Omega_{23}}{2} & \frac{\Omega_{21}}{\sqrt{2}} & 0 & 0 \\ 0 & \frac{\Omega_{23}}{2} & -\Delta_{21} - \Delta_{23} & 0 & \frac{\Omega_{21}}{2} & 0 \\ 0 & \frac{\Omega_{21}}{\sqrt{2}} & 0 & -i\gamma & \frac{\Omega_{23}}{\sqrt{2}} & 0 \\ 0 & 0 & \frac{\Omega_{21}}{2} & \frac{\Omega_{23}}{\sqrt{2}} & -\frac{i\gamma}{2} - \Delta_{23} & \frac{\Omega_{23}}{\sqrt{2}} \\ 0 & 0 & 0 & 0 & \frac{\Omega_{23}}{\sqrt{2}} & -2\Delta_{23} \end{bmatrix} \quad (3.22)$$

By solving the eigenproblem of $H_{\text{eff}}^{(2)}$ in Eq. (3.22) one can calculate the distance-dependent behaviour of the photon absorption rate, which can be interpreted as a dissipative potential $V_d^{(2)}(r)$. This is done by obtaining the ground state of $\hat{H}_{\text{eff}}^{(2)}$, which corresponds to the grey state $|\psi_{\text{grey}}^{(2)}\rangle$ and computing the coherences corresponding to transitions $|1\rangle_a \leftrightarrow |2\rangle_a$ and $|3\rangle_a \leftrightarrow |2\rangle_a$ in both particles from the density operator $\hat{\rho}_{\text{grey}} = |\psi_{\text{grey}}^{(2)}\rangle\langle\psi_{\text{grey}}^{(2)}|$. Summing up these matrix elements after multiplying them with \hbar and the according photon scattering rate Ω_{2j}^2/γ , with $j = 1, 3$, yields the photon absorption rate. In our chosen basis the calculation writes as:

$$\begin{aligned} V_d^{(2)} &= V_{|3\rangle_a \leftarrow |2\rangle_a}^{(2)} + V_{|1\rangle_a \leftarrow |2\rangle_a}^{(2)}, \\ \text{with } V_{|1\rangle_a \leftarrow |2\rangle_a}^{(2)} &= \frac{\hbar\Omega_{21}^2}{\gamma} \left(\rho_{\text{grey}}^{\{12\}}\sqrt{2} + \rho_{\text{grey}}^{\{24\}}\sqrt{2} + \rho_{\text{grey}}^{\{35\}} \right) \\ \text{and } V_{|3\rangle_a \leftarrow |2\rangle_a}^{(2)} &= \frac{\hbar\Omega_{23}^2}{\gamma} \left(\rho_{\text{grey}}^{\{65\}}\sqrt{2} + \rho_{\text{grey}}^{\{54\}}\sqrt{2} + \rho_{\text{grey}}^{\{32\}} \right). \end{aligned} \quad (3.23)$$

Here, $\rho_{\text{grey}}^{\{mn\}}$ represents the density matrix element $\langle m | \hat{\rho}_{\text{grey}} | n \rangle$, where $|m\rangle$ and $|n\rangle$ are basis states of our chosen basis. The factor $\sqrt{2}$ in Eq. (3.23) is a result of including symmetric combinations of states in our basis. A derivation of factor Ω_{2j}^2/γ can be seen in Appendix A. Due to the distance-dependent interaction $U^{(2)}(r)$ this calculation yields a different photon absorption rate for each distance r , resulting in the distance-dependent dissipative potential for two atoms $V_d^{(2)} = V_d^{(2)}(r)$.

For a simplified system, where $\Omega_{21} = \Omega_{23} = \Omega$, $\Delta_{23} = 0$, and $U^{(2)}(r)$ and $\Delta_{21} = \Delta$ are assumed to be perturbative, this dissipative potential can be approximated by the function given in Eq. (3.24) with C_0 , C_3 , and C_6 being real, dimensionless constants:

$$\frac{V_d^{(2)}(r)}{\hbar\gamma} = C_0 - \frac{C_3}{\left(\frac{r}{r_0}\right)^3} + \frac{C_6}{\left(\frac{r}{r_0}\right)^6}, \quad (3.24)$$

$$(3.25)$$

where $C_0 = \frac{\Delta^2}{\sqrt{2}\Omega\gamma}$, $C_3 = \frac{\Delta}{\sqrt{2}\Omega}$, and $C_6 = \frac{4+9\sqrt{2}}{64}\frac{\gamma}{\Omega} + \frac{8+6\sqrt{2}}{64}\frac{\Omega}{\gamma}$ [32, 33]. For a positive detuning $\Delta > 0$ the obvious minimum of this function legitimises the supposition that an EIT window can be observed at some distance $r = r_{min}$. The similarity of Eq. (3.24) to the Lennard-Jones potential [82] encourages the assumption that a bound state will be formed, bearing in mind, however, that $V_d^{(2)}(r)$ does not describe potential energy, but quantifies the rate of dissipation of the two atoms to the environment.

The shapes of the effective dissipative two-atom potential $V_d^{(2)}(r)$ for various sets of parameter values can be seen in Chap. 4.

3.4. Effective Dissipative Potentials for Three Atoms

The application of the approximations and transformations used in Sec. 3.3 yields the unitary three-atom Hamiltonian $\hat{H}_0^{(3)}$:

$$\hat{H}_0^{(3)} = \hat{H}_{kin}^{(3)} + \hat{H}_{int}^{(3)}, \quad (3.26)$$

$$\text{with } \hat{H}_{kin}^{(3)} = \sum_{a=1,2,3} \sum_{\mathbf{k}} \frac{\hbar^2 \mathbf{k}_a^2}{2m} |\mathbf{k}\rangle_a \langle \mathbf{k}|_a \quad (3.27)$$

$$\begin{aligned} \text{and } \hat{H}_{int}^{(3)} = & \sum_a \left[\sum_{b < a} [U^{(2)}(|\hat{\mathbf{r}}_a - \hat{\mathbf{r}}_b|) |1\rangle_a |1\rangle_b \langle 1|_a \langle 1|_b] \right. \\ & - \hbar \left[\frac{\Omega_{21}}{2} (|2\rangle_a \langle 1|_a + |1\rangle_a \langle 2|_a) + \frac{\Omega_{23}}{2} (|2\rangle_a \langle 3|_a + |3\rangle_a \langle 2|_a) \right. \\ & \left. \left. + \Delta_{21} |1\rangle_a \langle 1|_a + \Delta_{23} |3\rangle_a \langle 3|_a \right] \right]. \quad (3.28) \end{aligned}$$

Here, \hbar denotes the reduced Planck constant \hbar , whereas m denotes the caesium mass (see Tab. B.1 in Appendix B for relevant data on caesium). While $\hat{H}_{kin}^{(3)}$ contains the kinetic energy of the three-atom system, $\hat{H}_{int}^{(3)}$ describes the interactions, which are outlined in Fig. 2.3 for one of the three atoms.

The summation in Eq. (3.27) runs over all allowed values of wave-vector \mathbf{k} . Wave vector operator $\hat{\mathbf{k}}_{\mathbf{a}}$ in Eq. (3.27) and position operator $\hat{\mathbf{r}}_{\mathbf{a}}$ in Eq. (3.28) are both two-dimensional vector operators, which only act on atom a .

Calculating the system's dynamics could be done using Eqs. (3.1) and (3.2), where the three-atom jump operators $\hat{c}_n = \sum_{\mathbf{k}} |\mathbf{k} + \Delta\mathbf{k}_n\rangle_{a_n} |i_n\rangle_{a_n} \langle\mathbf{k}|_{a_n} \langle 2|_{a_n}$ are defined by the triple $(\Delta\mathbf{k}_n, i_n, a_n)$, $\Delta\mathbf{k}_n$ determines energy and direction of the emitted photon, and the indices $i_n = 1, 3$ and $a_n = 1, 2, 3$ account for the final states and the decaying atoms, respectively. Again, the effort of solving these equations can be avoided by introducing an effective non-Hermitian Hamiltonian $\hat{H}_{\text{eff}}^{(3)}$ analogously to Sec. 3.3, which we are allowed to do if the inequalities in Eqs. (3.17) and (3.18) are satisfied:

$$\hat{H}_{\text{eff}}^{(3)} = \hat{H}_{\text{int}}^{(3)} - i\hat{V}_{\text{dis}}^{(3)} , \quad (3.29)$$

$$\text{with } \hat{V}_{\text{dis}}^{(3)} = \frac{\hbar}{2} \sum_n \gamma_n \hat{c}_n^\dagger \hat{c}_n . \quad (3.30)$$

For the three-atom case it is not possible to construct a basis, where certain basis states are decoupled from any possible excitation like in Sec. 3.3. Therefore, a basis consisting of all possible state and atom permutations is used: $\{|1, 1, 1\rangle, |1, 1, 2\rangle, |1, 2, 1\rangle, |2, 1, 1\rangle, |1, 1, 3\rangle, |1, 3, 1\rangle, |3, 1, 1\rangle, |2, 2, 2\rangle, |2, 2, 1\rangle, |2, 1, 2\rangle, |1, 2, 2\rangle, |2, 2, 3\rangle, |2, 3, 2\rangle, |3, 2, 2\rangle, |3, 3, 3\rangle, |3, 3, 1\rangle, |3, 1, 3\rangle, |1, 3, 3\rangle, |3, 3, 2\rangle, |3, 2, 3\rangle, |2, 3, 3\rangle, |1, 2, 3\rangle, |1, 3, 2\rangle, |2, 1, 3\rangle, |3, 1, 2\rangle, |2, 3, 1\rangle, |3, 2, 1\rangle\}$. In this basis the matrix form of the system's Hamiltonian $H_{\text{eff}}^{(3)}$ reads as:

$$H_{\text{eff}}^{(3)} = H_{\text{eff}}^{(3)} + H_{\text{eff}}^{\prime\prime(3)} , \quad (3.31)$$

with $H_{\text{eff}}^{\prime(3)}$ and $H_{\text{eff}}^{\prime\prime(2)}$ given in Eqs. (3.33) and (3.34), respectively. In Eq. (3.34) U_{ij} represents the two-atom dipole-dipole interaction $U^{(2)}(r_{ij})$ between atoms i and j .

Analogous to Sec. 3.3, solving the eigenproblem of the three-atom Hamiltonian matrix $H_{\text{eff}}^{(3)}$ in Eq. (3.31) yields the three-atom state $|\psi_{\text{grey}}^{(3)}\rangle$. The next step is to compute the density operator $\hat{\rho}_{\text{grey}} = |\psi_{\text{grey}}^{(3)}\rangle \langle\psi_{\text{grey}}^{(3)}|$ and its coherences. Similarly to Eq. (3.23), these coherences are summed up and multiplied by the photon scattering rate Ω_{2j}^2/γ and \hbar :

$$V_{\text{d}}^{(3)} = \frac{\hbar\Omega_{21}^2}{\gamma} \sum_x \rho_{\text{grey}}^{\{x\}} + \frac{\hbar\Omega_{23}^2}{\gamma} \sum_y \rho_{\text{grey}}^{\{y\}} , \quad (3.32)$$

where indices x and y are chosen so that $\rho_{\text{grey}}^{\{x\}}$ and $\rho_{\text{grey}}^{\{y\}}$ only denote coherences corresponding to transitions $|1\rangle_a \leftrightarrow |2\rangle_a$ and $|3\rangle_a \leftrightarrow |2\rangle_a$, respectively.

Note that the summation in Eq. (3.32) contains 6 terms in the two-atom case, but consists of 54 terms in the three-atom case. This calculation is executed for all possible sets of interatomic distances r_{21} , r_{23} , and r_{13} and their corresponding eigenstates. The distance-dependent interaction $U^{(3)}(\{r_{ij}\})$ then results in a distance-dependent dissipative potential $V_d^{(3)} = V_d^{(3)}(\{r_{ij}\})$.

The resulting shapes of the dissipative potential for various sets of parameter values are shown in Chap. 5.

4. Dissipative Two-Atom Systems

*Smilet er den korteste afstand mellem to mennesker.
(The smile is the shortest distance between two persons.)*

—Victor Borge [83]

In recent papers by Lemeshko and Weimer [32, 33], a dissipatively bound state between pairs of ultracold atoms in an appropriate one-dimensional optical trap was predicted. This chapter presents the corresponding dissipatively bound dimer state in two dimensions. By using the dissipative binding method presented in Sec. 2.3 and implementing it in a two-dimensional two-atom system, which is schematically shown in Fig. 2.2(a), the existence of such a bound metastable state in two dimensions is proved. Varying the system parameter values and probing the properties of the resulting dissipative potential, as done in Sec. 4.1, gives rise to an improved two-atom grey state $|\psi_{\text{grey}}^{(2)}\rangle$ and therefore improved dissipative binding. Finally, in Sec. 4.2, the results of a simulation of a two-dimensional two-atom system using the adapted MCWF method introduced in Sec. 3.2 are presented.

4.1. Choosing the Parameter Values

In contrast to previous work [32, 33], the two electronic transitions $|1\rangle_a \leftrightarrow |2\rangle_a$ and $|3\rangle_a \leftrightarrow |2\rangle_a$ are not assumed to be driven with the same Rabi frequencies ($\Omega_{21} \neq \Omega_{23}$) and transition $|1\rangle_a \leftrightarrow |2\rangle_a$ is not assumed to be driven resonantly ($\Delta_{23} \neq 0$). The reader is referred to Fig. 3.2 for a full account of the electronic structure.

This section examines the influence of parameters Ω_{21} , Ω_{23} , Δ_{21} , and Δ_{23} on the shape of $V_d^{(2)}(r)$ and its figures of merit. By considering the effects of these parameters on the distance of the dissipation minimum r_{min} , the value $V_d^{(2)}(r_{\text{min}})$, the asymptotic values $V_d^{(2)}(\infty) = \lim_{r \rightarrow \infty} V_d^{(2)}(r)$ and $V_d^{(2)}(0) = \lim_{r \rightarrow 0} V_d^{(2)}(r)$, and the depth of the dissipative potential well $\Delta V_d^{(2)} = V_d^{(2)}(\infty) - V_d^{(2)}(r_{\text{min}})$, it was possible to determine a set of parameter values promising a strong dissipative bond between the atoms. The examined parameter values always satisfied the conditions of Eqs. (3.17) and (3.18). In experiment the parameter values can be tuned by modifying amplitudes and frequencies of the corresponding laser beams. Furthermore, dipole moment d and therefore the strength of $U^{(2)}(r)$ can

also be altered. This, however, only changes the characteristic length scale of the dipole-dipole interaction r_0 and therefore the overall shape of $V_d^{(2)}(r)$ stays the same when lengths are expressed in units of r_0 .

Varying detunings Δ_{21} and Δ_{23} :

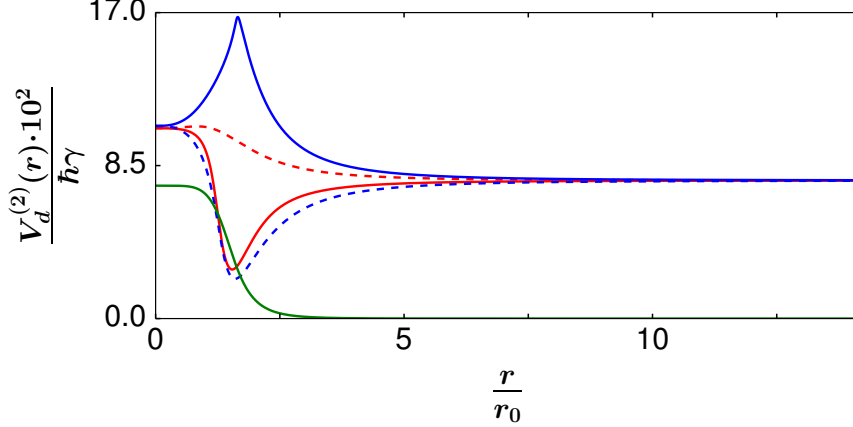


Figure 4.1.: The curve of $V_d^{(2)}(r)$ is shown for different sets of parameter values with varying detunings Δ_{21} and Δ_{23} . Parameter values for each graph are listed in Tab. 4.1.

Parameters Δ_{21} and Δ_{23} , which denote the detunings of the laser beams coupling state $|2\rangle_a$ to state $|1\rangle_a$ and state $|3\rangle_a$, respectively, have an essential effect on the qualitative appearance of $V_d^{(2)}(r)$. This can be explained by the aforementioned phenomenon of CPT, which was introduced in Sec. 2.2 and which only yields the desired two-atom grey state $|\psi_{\text{grey}}^{(2)}\rangle$ and the subsequent suppression of photon absorption if transitions $|2\rangle_a \leftrightarrow |1\rangle_a$ and $|2\rangle_a \leftrightarrow |3\rangle_a$ are being driven resonantly. This effect is demonstrated by the green graph viewed in Fig. 4.1: Because detunings Δ_{21} and Δ_{23} are equal to zero and detuning $\tilde{\Delta}_{21}$ decreases with increasing distance r , the transitions are being driven resonantly zero at asymptotically large distances.

	Ω_{21}	Ω_{23}	Δ_{21}	Δ_{23}	d
—	$0.5 \cdot \gamma$	$0.5 \cdot \gamma$	$0.2 \cdot \gamma$	0.	5.9 D
- - -	$0.5 \cdot \gamma$	$0.5 \cdot \gamma$	$-0.2 \cdot \gamma$	0.	5.9 D
—	$0.5 \cdot \gamma$	$0.5 \cdot \gamma$	0.	$0.2 \cdot \gamma$	5.9 D
- - -	$0.5 \cdot \gamma$	$0.5 \cdot \gamma$	0.	$-0.2 \cdot \gamma$	5.9 D
—	$0.5 \cdot \gamma$	$0.5 \cdot \gamma$	0.	0.	5.9 D

Table 4.1.: Parameter values for the different graphs of $V_d^{(2)}(r)$ shown in Fig. 4.1 and of $V_d^{(3)}(r)$ shown in Fig. 5.1.

A minimum of the effective dissipative potential $V_d^{(2)}(r)$ can only be observed when the system's lasers are detuned in such a way that the detuning due to the dipole-dipole interaction $U^{(2)}(r)$ in state $|1, 1\rangle$ renders the driving of transitions $|2\rangle_a \leftrightarrow |1\rangle_a$ and $|2\rangle_a \leftrightarrow |3\rangle_a$ more resonant at some distance r . This is the case for positive detuning Δ_{21} and/or negative detuning Δ_{23} , as can be inferred from Fig. 4.1. The opposite case, where detuning Δ_{21} is less than zero and/or detuning Δ_{23} is larger than zero, gives rise to a peak in dissipation at a certain distance r , where transitions $|2\rangle_a \leftrightarrow |1\rangle_a$ and $|2\rangle_a \leftrightarrow |3\rangle_a$ are being driven even less resonantly. For our purposes, the latter situation is disadvantageous.

Varying Rabi frequencies Ω_{21} and Ω_{23} :

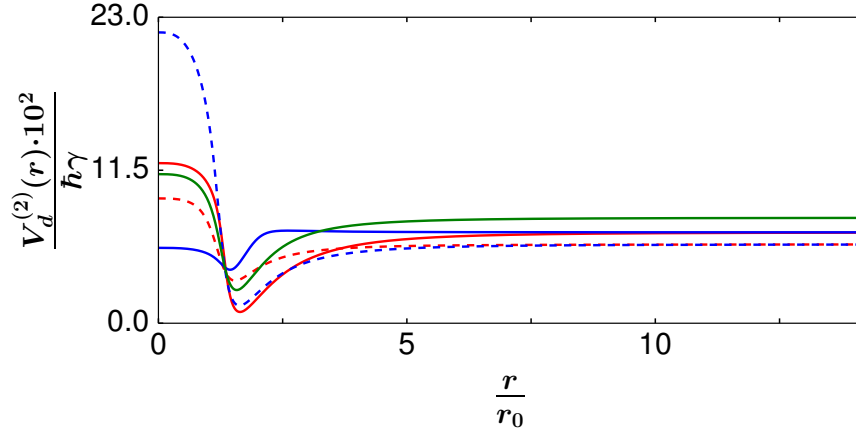


Figure 4.2.: The curve of $V_d^{(2)}(r)$ is shown for different sets of parameter values with varying Rabi frequencies Ω_{21} and Ω_{23} . Parameter values for each graph are listed in Tab. 4.2.

Previously, we have concluded that assigning a positive value to detuning Δ_{21} and a negative value to detuning Δ_{23} guarantees the existence of a minimum in the dissipative potential $V_d^{(2)}(r)$. Now, we show that manipulating Rabi frequencies Ω_{21} and Ω_{23} , which are a measure of population transport from state $|2\rangle_a$ to states $|1\rangle_a$ and $|3\rangle_a$, respectively, allows us to tune the qualitative properties of this dissipation minimum. It can be inferred from Fig. 4.2 and Tab. 4.2 that the ratio of these two parameters influences the skewness of the graph: reducing the ratio Ω_{21}/Ω_{23} decreases $V_d^{(2)}(\infty)$ while increasing $V_d^{(2)}(0)$ and vice versa.

The quantitative properties of the dissipative potential $V_d^{(2)}(r)$ are also affected by adjusting the Rabi frequencies Ω_{21} and Ω_{23} . The level of dissipation is reduced at most distances by raising frequency Ω_{21} . But the value of $V_d^{(2)}(\infty)$ falls more strongly than the value of $V_d^{(2)}(r_{\min})$ leading to a smaller quantity $\Delta V_d^{(2)}$, which is an important measure for the quality of the dissipative bond. Manipulating frequency Ω_{23} affects the value of $\Delta V_d^{(2)}$ in the same manner, but to a lesser extent.

	Ω_{21}	Ω_{23}	Δ_{21}	Δ_{23}	d
—	$0.35 \cdot \gamma$	$0.50 \cdot \gamma$	$0.1 \cdot \gamma$	$-0.1 \cdot \gamma$	5.9 D
- - -	$0.65 \cdot \gamma$	$0.50 \cdot \gamma$	$0.1 \cdot \gamma$	$-0.1 \cdot \gamma$	5.9 D
—	$0.50 \cdot \gamma$	$0.35 \cdot \gamma$	$0.1 \cdot \gamma$	$-0.1 \cdot \gamma$	5.9 D
- - -	$0.50 \cdot \gamma$	$0.65 \cdot \gamma$	$0.1 \cdot \gamma$	$-0.1 \cdot \gamma$	5.9 D
—	$0.50 \cdot \gamma$	$0.50 \cdot \gamma$	$0.1 \cdot \gamma$	$-0.1 \cdot \gamma$	5.9 D

Table 4.2.: Parameter values for the different graphs of $V_d^{(2)}(r)$ shown in Fig. 4.2 and of $V_d^{(3)}(r)$ shown in Fig. 5.2.

Generally, detunings Δ_{21} and Δ_{23} primarily determine the qualitative shape of $V_d^{(2)}(r)$, whereas Rabi frequencies Ω_{21} and Ω_{23} mainly affect quantitative parameters, such as the overall level of dissipation.

Optimised Parameter Values:

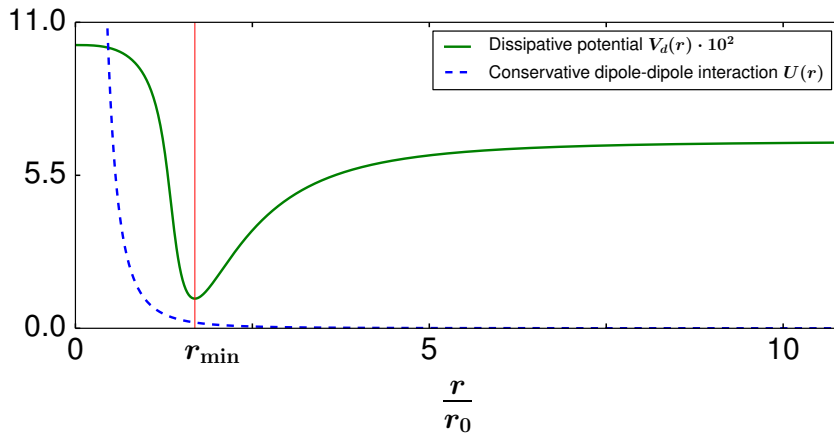


Figure 4.3.: The effective dissipative two-atom potential $V_d^{(2)}(r)$ with optimised parameter values and the conservative dipole-dipole interaction $U^{(2)}(r)$ are shown. Parameter values used for $V_d^{(2)}(r)$ are listed in Tab. 4.3.

By tuning the values of Rabi frequencies Ω_{21} and Ω_{23} and detunings Δ_{21} and Δ_{23} in order to reach a satisfying trade-off between maximising $\Delta V_d^{(2)}$ and minimising $V_d^{(2)}(r_{\min})$, a set of optimised parameter values was found.

Ω_{21}	Δ_{21}	Ω_{23}	Δ_{23}	d
$0.375 \cdot \gamma$	$0.1 \cdot \gamma$	$0.475 \cdot \gamma$	$-0.075 \cdot \gamma$	8.85 D

Table 4.3.: Optimised parameter values for the dimer state.

These parameter values are listed in Tab. 4.3, while the corresponding dissipation curve $V_d^{(2)}(r)$ is displayed in Fig. 4.3. The conditions of Eqs. (3.17) and (3.18) were taken into account when searching for this set of parameter values.

$\frac{r_{\min}}{r_0}$	$\frac{V_d^{(2)}(r_{\min})}{\hbar\gamma} \cdot 10^2$	$\frac{V_d^{(2)}(0)}{\hbar\gamma} \cdot 10^2$	$\frac{V_d^{(2)}(\infty)}{\hbar\gamma} \cdot 10^2$	$\frac{\Delta V_d^{(2)}}{\hbar\gamma} \cdot 10^2$
1.69	1.07	10.18	6.70	5.64

Table 4.4.: Important quantities of $V_d^{(2)}(r)$ with optimised parameter values.

In Tab. 4.4 the calculated figures of merit introduced at the beginning of this chapter are listed. These quantities allow for a quantitative judgement of the dissipative bond. The calculated values indicate that the dissipative curve with optimised parameter values has almost no dissipation at the minimum $V_d^{(2)}(r_{\min})$ while still maintaining a large depth of the potential well $\Delta V_d^{(2)}$. Due to the beneficial shape of the graph $V_d^{(2)}(r)$ in Fig. 4.3 to forming bound states, this optimised dissipative potential was used to simulate a two-dimensional two-atom system in Sec. 4.2.

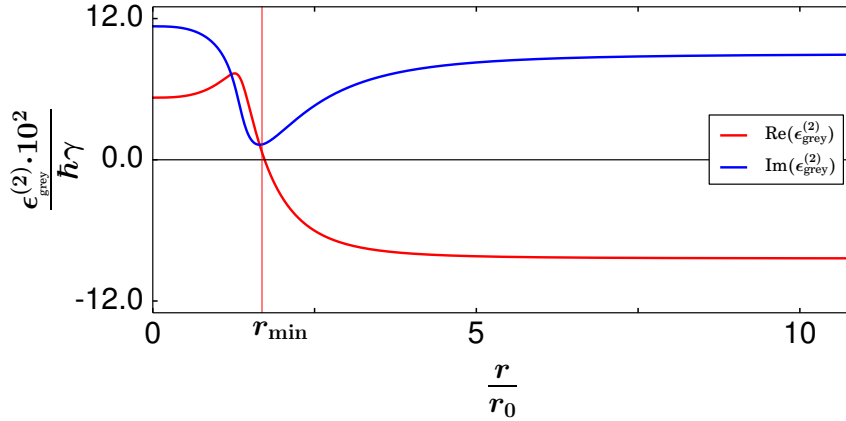


Figure 4.4.: Real and imaginary part of the two-atom grey states' eigenvalue $\epsilon_{\text{grey}}^{(2)}$ are shown.

In order to further examine the calculated dissipative potential, the distance-dependent behaviour of the two-atom grey states' eigenvalue $\epsilon_{\text{grey}}^{(2)}$ was examined. Figure 4.4 shows that the imaginary part and thus the population leaking out of the system is minimised at distance r_{\min} . The real part, on the other hand, converges to zero at r_{\min} , indicating that the system's two-atom grey state $|\psi_{\text{grey}}^{(2)}\rangle$ approaches a true dark state. A true dark state's eigenvalue must vanish, as it corresponds to a linear combination of ground states, whose eigenvalues are equal to zero after applying the rotating frame approximation.

Additionally, the difference between the distance-dependent behaviour of the population of excited states $(|1, 2\rangle + |2, 1\rangle)/\sqrt{2}$, $|2, 2\rangle$, and $(|2, 3\rangle + |3, 2\rangle)/\sqrt{2}$

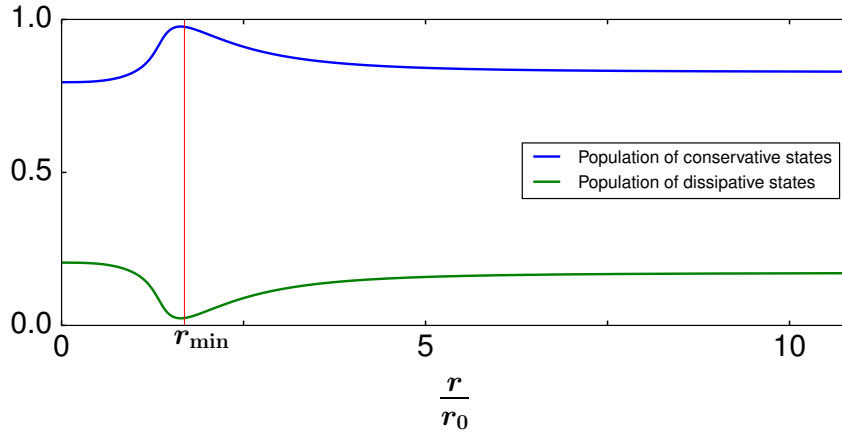


Figure 4.5.: Dissipative and conservative populations of the two-atom grey state $|\psi_{\text{grey}}^{(2)}\rangle$ are shown.

and the distance-dependent behaviour of the ground states' population ($|1, 1\rangle$, $(|1, 3\rangle + |3, 1\rangle)/\sqrt{2}$, and $|3, 3\rangle$) was investigated. The plot in Fig. 4.5 clearly shows that the dissipative states' population decreases, whereas the conservative states' population increases in the vicinity of r_{min} , almost reaching a true dark state. As only population in the excited states is able to decay, this indicates that dissipation is reduced at r_{min} .

4.2. Simulation of the Two-Atom System

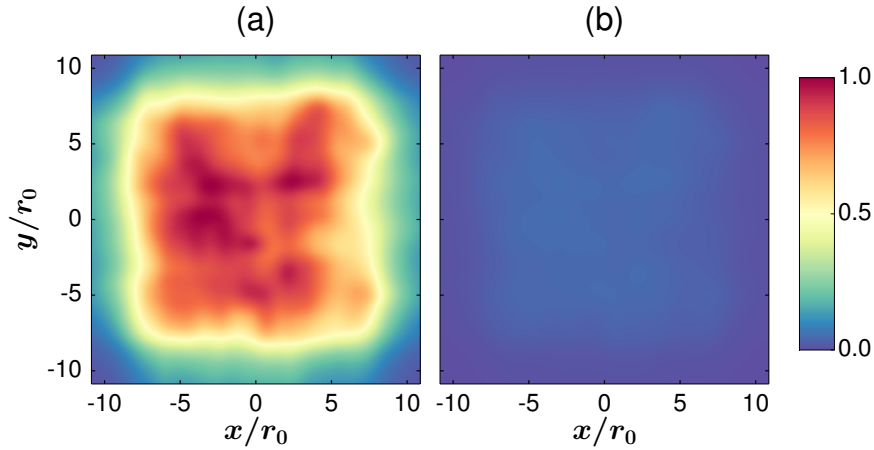


Figure 4.6.: The averaged two-atom probability distribution in relative x - and y -coordinates at time $t_{\text{init}} = 0 \cdot \gamma^{-1}$ is shown. The distribution is given in arbitrary units with the largest colour value corresponding to the largest peak of the atom distribution at time t_{init} in subpanel (a) and at time t_{fin} in subpanel (b).

In this section the results of a simulation of a two-dimensional two-atom system with optimised parameters listed in Tab. 4.3 are presented. The following plots were obtained by generating 1000 realisations of this two-atom system using the adapted MCWF simulation method described in Sec. 3.2. Each realisation was run for a total time of $t_{\text{fin}} = 200 \cdot \gamma^{-1} = 6.10 \mu\text{s}$ with 400 timesteps and a time increment of $\delta t = 0.5 \cdot \gamma^{-1} = 15.25 \text{ ns}$. The relative x- and y-coordinates of the simulation box, which were discretised by 201 gridpoints, ranged from $-10.82 \cdot r_0 = -2.65 \mu\text{m}$ to $+10.82 \cdot r_0 = +2.65 \mu\text{m}$. Therefore, the resulting grid stepsize calculates as $\delta r = 0.11 \cdot r_0 = 26.5 \text{ nm}$. The initial space and momentum distribution of the atoms in relative coordinates was chosen according to the Boltzmann distribution at the selected temperature of 20 nK, while the centers of the spatial distribution were distributed randomly within a range from $-8.65 \cdot r_0 = -2.12 \mu\text{m}$ to $+8.65 \cdot r_0 = +2.21 \mu\text{m}$ in both dimensions. State $|1\rangle_a$ was provided with a dipole moment $d = 8.85 \text{ D} = 2.95 \cdot 10^{-29} \text{ C} \cdot \text{m}$ to enable the distance-dependent population trapping. This value of the electric dipole moment d yields a characteristic interaction length $r_0 = 0.25 \mu\text{m}$ (see Eq. (3.19)).

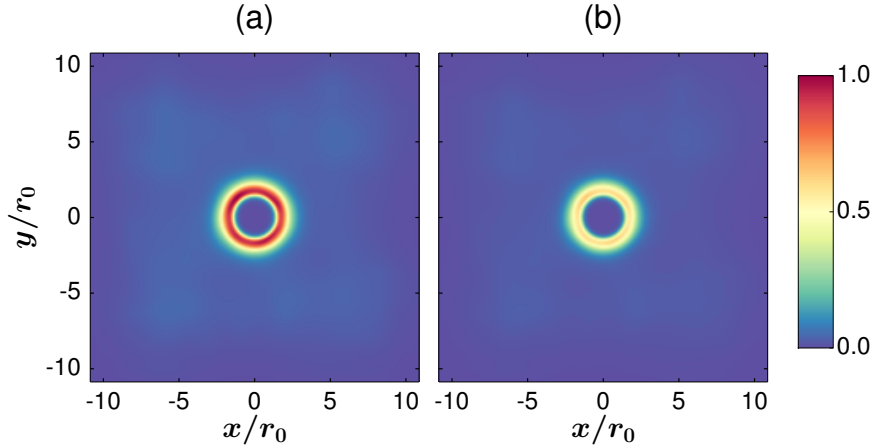


Figure 4.7.: The averaged two-atom probability distribution in relative x- and y-coordinates at time $t_{\text{itm}} = 100 \cdot \gamma^{-1}$ is shown. The distribution is given in arbitrary units with the largest colour value corresponding to the largest peak of the atom distribution at time t_{itm} in subpanel (a) and at time t_{fin} in subpanel (b).

Averaging over all 1000 realisations of the simulation yielded the distributions viewed in Figs. 4.6 to 4.8. Initially, the distribution is quasi-homogenous and does not exhibit any distinctive characteristics, as shown in Figs. 4.6(a) and 4.6(b). By comparing Figs. 4.6(a) and 4.6(b), it can be seen that the maximum of the distribution at time t_{fin} is many times larger than the maximum at time t_{init} . In Figs. 4.7(a) and 4.7(b) the averaged two-particle distribution at intermediate time $t_{\text{itm}} = 100 \cdot \gamma^{-1}$ is visualised. There, a definite trend in the time evolution of the two-atom system can be observed: a hole emerges in the center of the plot,

which corresponds to both atoms being at the same location. This indicates that the two-atoms avoid getting too close to each other, a consequence of the dipole-dipole interaction and the distance-dependent CPT. Around this hole the population accumulates over time, whereas the rest of the plot undergoes relatively little change, except for a general decrease in population. The observed trend continues and results in the final distribution at time $t_{\text{fin}} = 200 \cdot \gamma^{-1}$, which is displayed in Fig. 4.8(b). Comparing the initial distribution in Fig. 4.8(a) to the final distribution in Fig. 4.8(b) shows that the system evolves from a quasi-uniform distribution, where all interatomic distances are equally likely, to a distribution, where interatomic distance $r = (1.70 \pm 0.11) \cdot r_0$ is many times more likely than any other distance. The reader is referred to Fig. C.1 in Appendix C for a more detailed account of the two-atom distribution's time evolution.

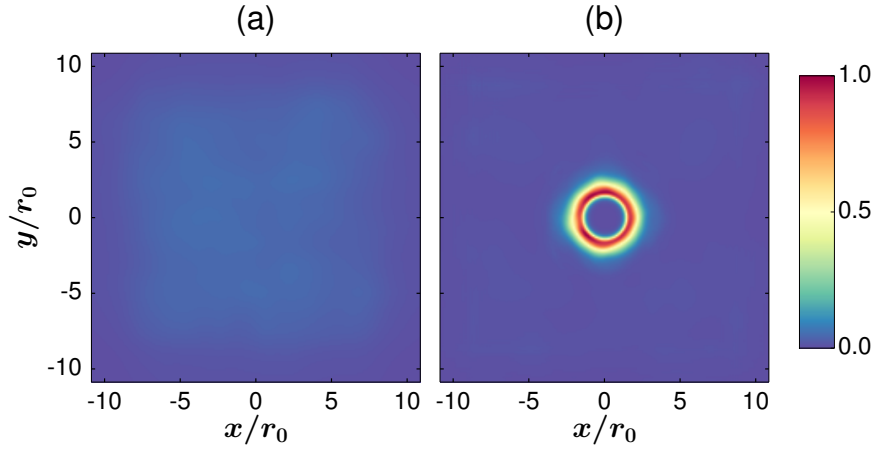


Figure 4.8.: The averaged two-atom probability distributions in relative x- and y-coordinates (a) at time $t_{\text{init}} = 0 \cdot \gamma^{-1}$ and (b) at time $t_{\text{fin}} = 200 \cdot \gamma^{-1}$ are shown. The distributions are given in arbitrary units with the largest colour value corresponding to the largest peak of the atom distribution at time t_{fin} in both subpanels.

Furthermore, the two-atom pair correlation function $g^{(2)}(r)$, which contains the probability of finding the two atoms at an interatomic distance r , was calculated. The time evolution of $g^{(2)}(r)$ is displayed in Fig. 4.9, where the emergence of a maximum is clearly visible. The graphs in Fig. 4.9 were obtained using interpolation of the originally calculated data over distance r in order to achieve additional smoothness. The maximum of $g^{(2)}(r)$ at time $t_{\text{fin}} = 200 \cdot \gamma^{-1}$ is situated at $r = (1.73 \pm 0.11) \cdot r_0$, which is consistent with the position of the ringlike peak in the final distribution at time t_{fin} and with distance r_{min} in Tab. 4.4. The distinct ringlike peak in Fig. 4.8(b) and the maximum of $g^{(2)}(r)$ at t_{fin} in Fig. 4.9 are clear evidence for a dissipative two-atom bound state in the examined two-dimensional two-atom system with optimised parameters.

Analogous to conservatively bound particles, where the amount of energy re-

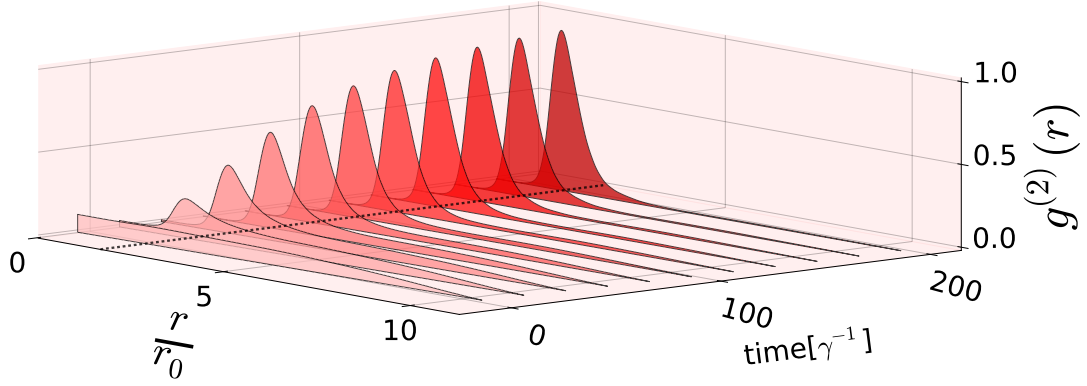


Figure 4.9.: The two-atom pair correlation function $g^{(2)}(r)$ of the simulated two-atom system is shown with optimised parameters at increasing times. The dotted black line indicates the most probable interatomic distance.

quired for dissociation defines the strength of the bond, the strength of the dissipative bond can be characterised by an imaginary binding energy $E_b^{(2)}$. This energy is a measure for the amount of dissipation that has to be added to the system for dissociation to occur. It is defined as the depth of the dissipative potential well $\Delta V_d^{(2)} = V_d^{(2)}(\infty) - V_d^{(2)}(r_{\min})$ and amounts to $E_b^{(2)} = \Delta V_d^{(2)} = 5.64 \cdot 10^{-2} \cdot \hbar\gamma$ for the two-atom bond with optimised parameters.

5. Dissipative Three-Atom Systems

*Ich sei, gewährt mir die Bitte,
In eurem Bunde der Dritte!
(Tis mine your suppliant now to be,
Ah, let the band of love - be three!))*

—Friedrich Schiller, *Die Bürgschaft* [84]

Now, after examining the metastable dimer state in one- and two-dimensional systems, we extend the dissipative binding method of Sec. 2.3 in order to find an equivalent trimer state in two dimensions. In this chapter the three-atom system of Sec. 2.1, which is shown in Fig. 2.2(b), is used. The existence of such a dissipatively bound three-body state is proved in Sec. 5.1 and its properties are probed by varying the system parameter values analogously to Sec. 4.1. Additionally, the results of a simulation of a two-dimensional three-atom system with optimised parameter values using the adapted MCWF method introduced in Sec. 3.2 are presented in Sec. 5.2.

5.1. Choosing the Parameter Values

Similarly to Sec. 4.1, the effect of parameters Ω_{21} , Ω_{23} , Δ_{21} , and Δ_{23} on the shape of the effective dissipative three-atom potential $V_d^{(3)}(r_{21}, r_{23}, \Theta)$ is examined in this section. Each of the parameters can be seen in the representative electronic energy structure of one individual atom shown in Fig. 2.3. The examined parameter values always satisfied the conditions of Eqs. (3.17) and (3.18).

We also introduce the following quantities of the dissipative three-atom bond: the distance of the dissipation minimum r_{\min} , the value $V_d^{(3)}(r_{\min})$, the asymptotic values $V_d^{(3)}(\infty) = \lim_{r \rightarrow \infty} V_d^{(3)}(r)$ and $V_d^{(3)}(0) = \lim_{r \rightarrow 0} V_d^{(3)}(r)$, and the depth of the dissipative potential well $\Delta V_d^{(3)} = V_d^{(3)}(\infty) - V_d^{(3)}(r_{\min})$. The interatomic distances used to search for a set of optimised parameter values are all measured in the equilateral triangle configuration ($r_{21} = r_{31} = r_{23} = r$ and $\Theta = 60^\circ$). Once such a set of optimised parameter values was found, other constellations were investigated.

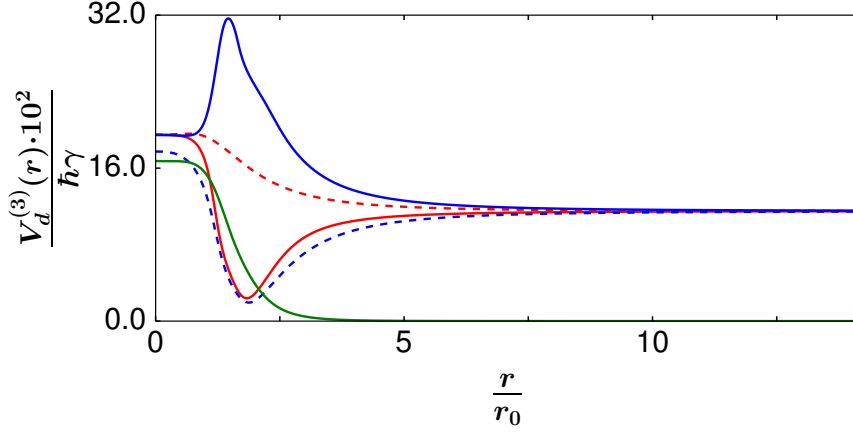
Varying detunings Δ_{21} , Δ_{23} and Rabi frequencies Ω_{21} , Ω_{23} :


Figure 5.1.: The curve of $V_d^{(3)}(r)$ is shown for different sets of parameter values with varying detunings Δ_{21} and Δ_{23} . Parameter values for each graph are listed in Tab. 4.1.

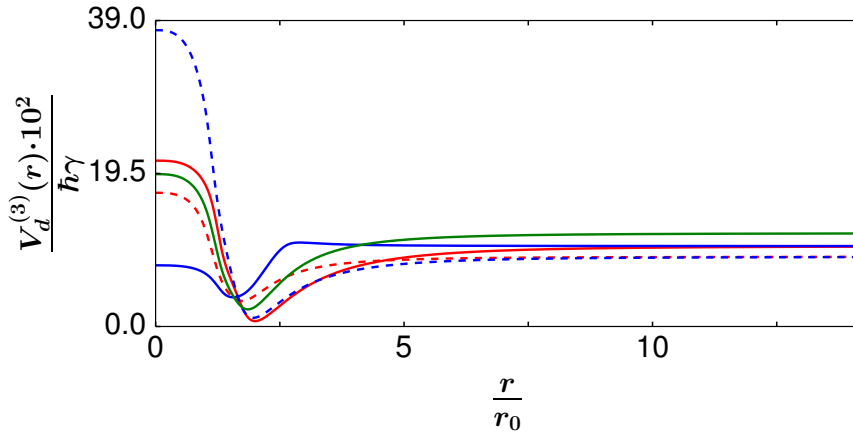


Figure 5.2.: The curve of $V_d^{(3)}(r)$ is shown for different sets of parameter values with varying Rabi frequencies Ω_{21} and Ω_{23} . Parameter values for each graph are listed in Tab. 4.2.

Manipulation of detunings Δ_{21} and Δ_{23} and of Rabi frequencies Ω_{21} and Ω_{23} yields qualitatively the same results as in Sec. 4.1, indicating that the dissipative three-atom potential $V_d^{(3)}(r)$ in the equilateral triangle configuration behaves qualitatively the same as the dissipative two-atom potential $V_d^{(2)}(r)$. Therefore, the conclusions of Sec. 4.1 are also applicable here. The resulting graphs are viewed in Figs. 5.1 and 5.2.

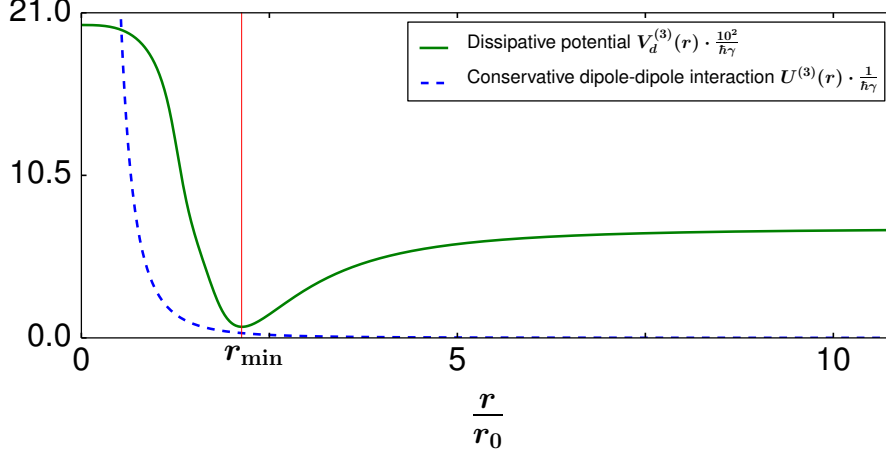
Optimised Parameter Values:

Figure 5.3.: The effective dissipative potential $V_d^{(3)}(r)$ for the optimised parameter values and the conservative dipole-dipole interaction $U^{(3)}(r)$ are shown. We assume an equilateral triangle configuration ($r_{21} = r_{31} = r_{23} = r$ and $\Theta = 60^\circ$). Parameter values used for $V_d^{(3)}(r)$ are listed in Tab. 5.1.

Ω_{21}	Ω_{23}	Δ_{21}	Δ_{23}	d
$0.4 \cdot \gamma$	$0.1 \cdot \gamma$	$0.5 \cdot \gamma$	$-0.05 \cdot \gamma$	8.85 D

Table 5.1.: Optimised parameter values for the trimer state.

The optimised parameters values, which guarantee optimal trade-off between maximising $\Delta V_d^{(3)}$ and minimising $V_d^{(3)}(r_{\min})$, are listed in Tab. 5.1. The parameter values satisfy the conditions of Eqs. (3.17) and (3.18). In Fig. 5.3 the resulting dissipation curve $V_d^{(3)}(r)$ for the equilateral triangle configuration compared to the total dipole-dipole interaction $U^{(3)}(r)$ is displayed. The dipole-dipole interaction $U^{(3)}(r)$ is calculated by summing up all pairwise interactions $U^{(2)}(r)$, which, in the equilateral triangle configuration, corresponds to multiplying $U^{(2)}(r)$ by a factor of 3.

$\frac{r_{\min}}{r_0}$	$\frac{V_d^{(3)}(r_{\min})}{\hbar\gamma} \cdot 10^2$	$\frac{V_d^{(3)}(0)}{\hbar\gamma} \cdot 10^2$	$\frac{V_d^{(3)}(\infty)}{\hbar\gamma} \cdot 10^2$	$\frac{\Delta V_d^{(3)}}{\hbar\gamma} \cdot 10^2$
2.13	0.71	20.21	6.96	6.25

Table 5.2.: Important quantities of $V_d^{(3)}(r)$ with optimised parameter values.

In order to measure the capability of the system with optimised parameter values to give rise to a dissipative bond, we calculate the aforementioned quantities,

which are listed in Tab. 5.2. The low dissipation at r_{\min} and the large depth of the dissipative potential well $\Delta V_d^{(3)}$ indicate that these parameter values are highly suitable for a trimer state. When comparing the quantities of Tab. 5.2 to the ones of Tab. 4.4, one has to bear in mind that this comparison is done between systems with different numbers of atoms. A more correct comparison can be done by using per-atom properties, which will be done in Chap. 6.

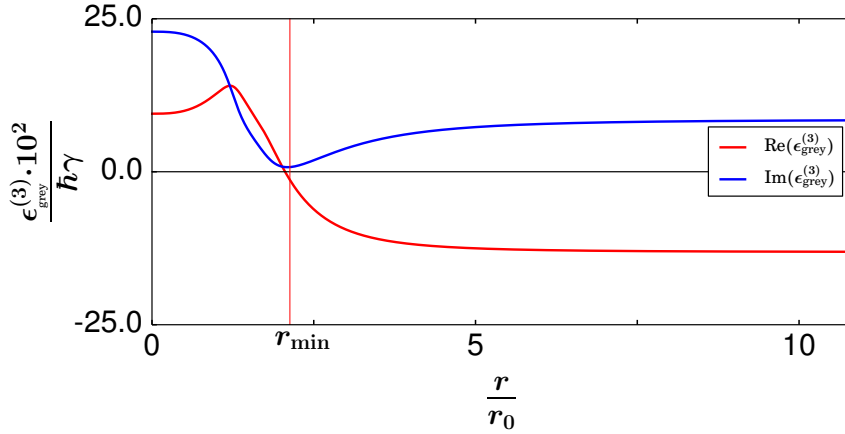


Figure 5.4.: Real and imaginary part of the three-atom grey states' eigenvalue $\epsilon_{\text{grey}}^{(3)}$ are shown.

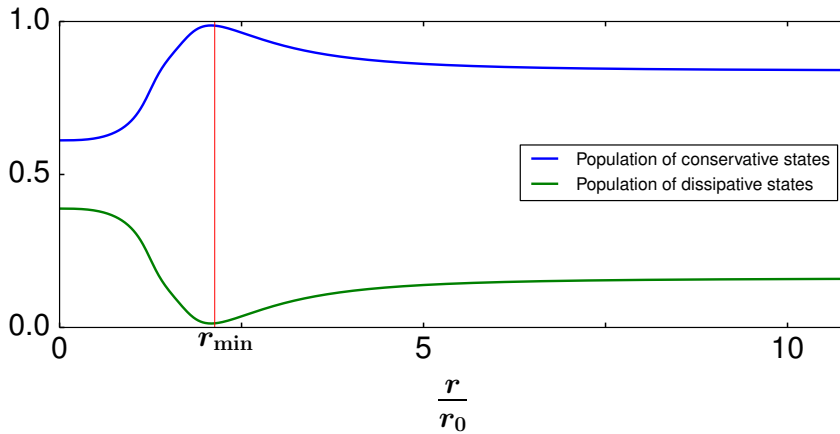


Figure 5.5.: Dissipative and conservative population of the three-atom grey state $|\psi_{\text{grey}}^{(3)}\rangle$ are shown.

Furthermore, the distance-dependent behaviour of the eigenvalue $\epsilon_{\text{grey}}^{(3)}$ and of the populations in dissipative and conservative states of the three-atom grey state $|\psi_{\text{grey}}^{(3)}\rangle$ in the equilateral triangle configuration are shown Figs. 5.4(a) and 5.4(b). Again, there are strong qualitative similarities to Figs. 4.4 and 4.5 and the same conclusions apply.

Because the atoms are not confined to an equilateral triangle constellation, other configurations also have to be taken into account. In the following examples configurations with different opening angles Θ , which are assumed to be fixed, are considered. The resulting geometry is outlined in Fig. 2.2(b). It is assumed that symmetric constellations yield the lowest dissipation minima. An obvious consequence of this assumption is that the minimum will always be at an isosceles triangle configuration ($r_{21} = r_{31}$ and $\Theta \neq 60^\circ$) or at an equilateral triangle configuration ($r_{21} = r_{31}$ and $\Theta = 60^\circ$). To prove this supposition plots of the dissipative potential $V_d^{(3)}(r_{21}, r_{31}, \Theta)$ for a range of fixed opening angles Θ are viewed in Figs. 5.6 and 5.7.

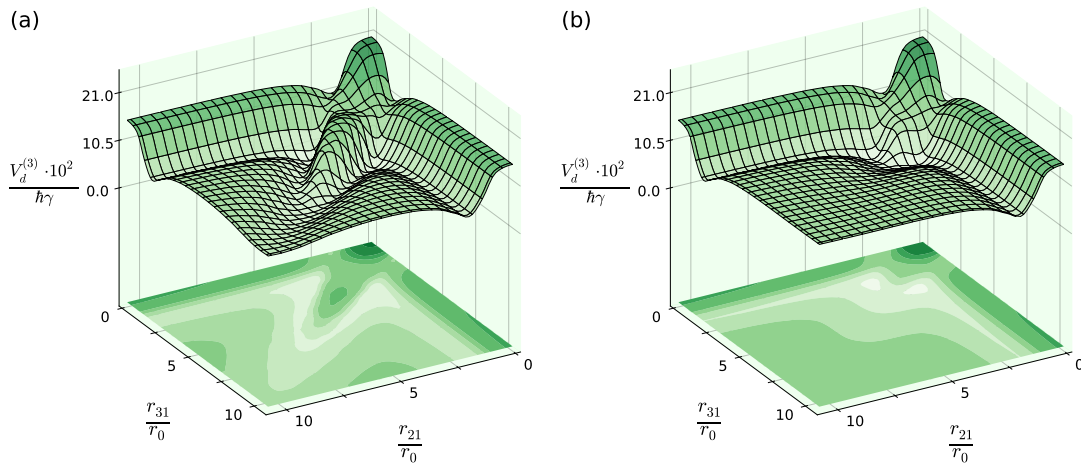


Figure 5.6.: The effective dissipative three-atom potential $V_d^{(3)}(r_{21}, r_{31}, \Theta)$: sub-panel (a) corresponds to a fixed value of opening angle $\Theta = 15^\circ$, whereas subpanel (b) corresponds to a fixed value of opening angle $\Theta = 30^\circ$.

The acute-angled triangle configurations with $\Theta = 15^\circ$ and $\Theta = 30^\circ$ in Figs. 5.6(a) and 5.6(b) both display minima which do not satisfy the isosceles condition $r_{21} = r_{31}$. Furthermore, these plots not only display one minimum, but two minima, which are symmetric with respect to the $r_{21} = r_{31}$ diagonal. The seeming disagreement of these graphs with the assumption of an isosceles triangle configuration can be solved when considering the other angles of the triangle: The two minima in Fig. 5.6(a) are at positions corresponding to isosceles triangles with $r_{21} = r_{23}$, $r_{31} = r_{23}$, and a vertex angle of 150° . Similarly, the minima positions in Fig. 5.6(b) characterise isosceles triangles with $r_{21} = r_{23}$, $r_{31} = r_{23}$, and a vertex angle of 120° . The contour plots depicted Figs. 5.7(a) and 5.7(b) exhibit only one minimum at $r_{21} = r_{31}$ due to the opening angle Θ being equal or larger than 60° . The overall minimum of dissipation of all possible geometries is found at the equilateral triangle configuration with $r_{21} = r_{31} = r_{23} = 2.13 \cdot r_0$ and $\Theta = 60^\circ$, which is supported by the data of Tab. 5.2.

Generally, the minimum of dissipation is at an isosceles triangle geometry

with $\Theta \geq 60^\circ$. If the opening angle Θ is fixed to a value smaller than 60° , the resulting minima are at positions corresponding to isosceles triangles, where one of the remaining angles is as large as Θ , while the other remaining angle has the value $180^\circ - 2\Theta$.

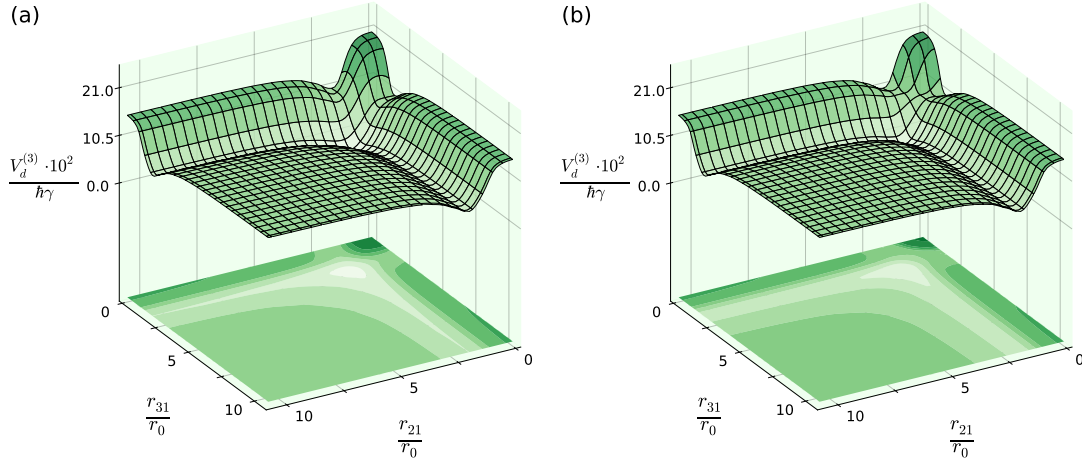


Figure 5.7.: The effective dissipative three-atom potential $V_d^{(3)}(r_{21}, r_{31}, \Theta)$: sub-panel (a) corresponds to a fixed value of opening angle $\Theta = 60^\circ$, whereas subpanel (b) corresponds to a fixed value of opening angle $\Theta = 120^\circ$.

Therefore, we have found the geometry resulting in the total minimum of dissipation for the three-atom system with optimised parameters and expect that the dissipatively bound trimer state has the highest probability to occur at this equilateral triangle configuration. In the next section the results of a two-dimensional three-atom system with optimised parameters will be presented and examined.

5.2. Simulation of the Three-Atom System

After obtaining a set of optimised parameters (see Tab. 5.1), a corresponding two-dimensional three-atom system was simulated using the adapted MCWF method introduced in Sec. 3.2. The results were obtained by averaging over 1000 realisations of the system at a temperature of 20 nK. Each realisation started at time $t_{\text{init}} = 0 \cdot \gamma^{-1} = 0 \mu\text{s}$ and was simulated to its final state at time $t_{\text{fin}} = 200 \cdot \gamma^{-1} = 6.10 \mu\text{s}$ in 200 timesteps of length $\delta t = \gamma^{-1} = 30.5 \text{ ns}$. The probability distributions at selected simulation times are depicted in Figs. 5.8 to 5.10. Figures C.2 to C.6 in Appendix C show the results of the same simulation with higher time resolution.

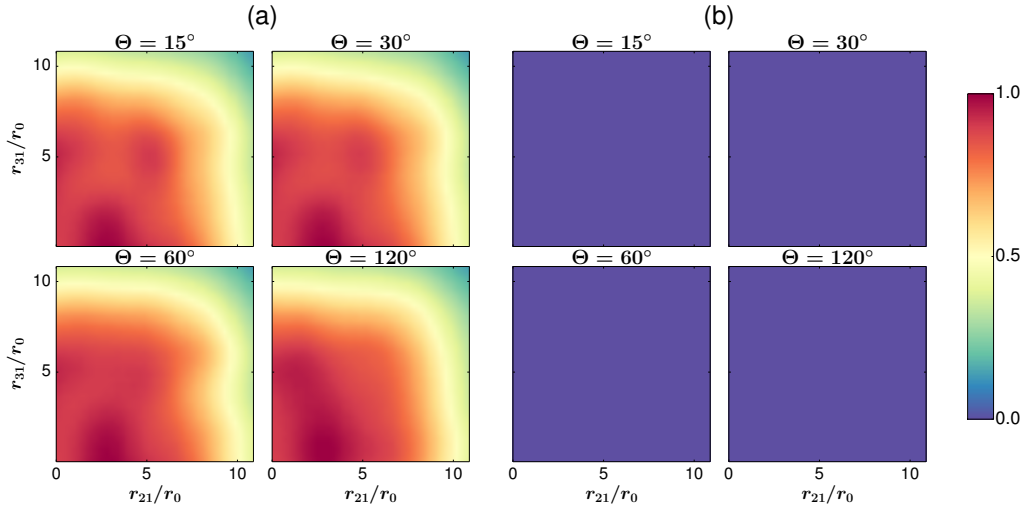


Figure 5.8.: The averaged three-atom probability distribution at time t_{init} is shown. The coordinates of the axes represent interatomic distances r_{21} and r_{31} . The distribution is given in arbitrary units with the largest value corresponding to the largest peak of the atom distribution at time t_{init} in subpanel (a) and at time t_{fin} in subpanel (b).

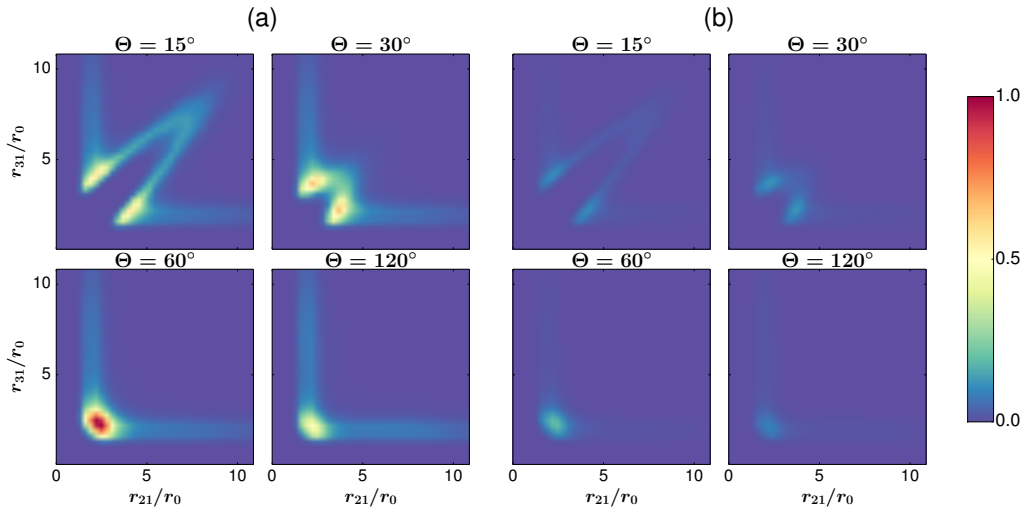


Figure 5.9.: The averaged three-atom probability distribution at time t_{itm} is shown. The coordinates of the axes represent interatomic distances r_{21} and r_{31} . The distribution is given in arbitrary units with the largest value corresponding to the largest peak of the atom distribution at time t_{itm} in subpanel (a) and at time t_{fin} in subpanel (b).

In order to render the problem numerically tractable, the relative coordinates were discretised by 75 gridpoints in both spatial dimensions. The relative x - and y -coordinates of the simulation box ranged from $-10.82 \cdot r_0 = -2.65 \mu\text{m}$ to $+10.82 \cdot r_0 = +2.65 \mu\text{m}$ with a grid stepsize $\delta r = 0.29 \cdot r_0$. The initial momentum distribution and the extent of the initial space distribution were chosen according to the Boltzmann distribution at the selected system temperature of 20 nK. Moreover, the position in relative x - and y -coordinates of the initial spatial distribution's center was randomly placed in a range from $-8.65 \cdot r_0 = -2.12 \mu\text{m}$ to $+8.65 \cdot r_0 = +2.21 \mu\text{m}$. Distance-dependent population trapping was enabled by providing state $|1\rangle_a$ with an electric dipole moment of $d = 8.85 \text{ D} = 2.95 \cdot 10^{-29} \text{ C m}$. Assigning a value to the dipole moment d also determines the characteristic interaction length r_0 , as defined in Eq. (3.19), which has the value $r_0 = 0.25 \mu\text{m}$ for our system.

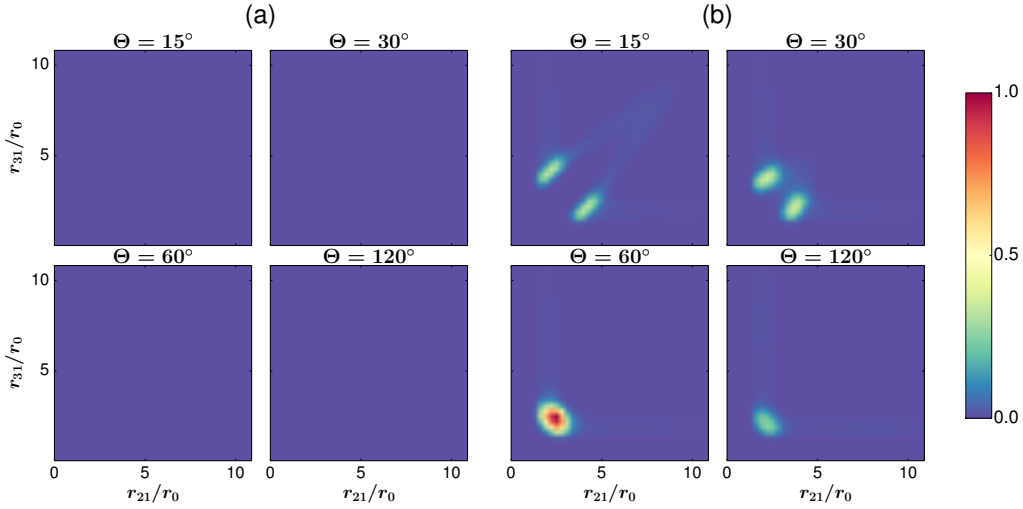


Figure 5.10.: The averaged three-atom probability distributions (a) at time $t_{\text{init}} = 0 \cdot \gamma^{-1}$ and (b) at time $t_{\text{fin}} = 200 \cdot \gamma^{-1}$ are shown. The coordinates of the axes represent interatomic distances r_{21} and r_{31} . The distributions are given in arbitrary units with the largest value corresponding to the largest peak of the atom distribution at time t_{fin} .

The averaged three-atom probability distributions with selected opening angles Θ at the initial simulation time t_{init} are shown in Figs. 5.8(a) and 5.8(b). As it can be observed in Fig. 5.8, the distribution appears to be of quasi-uniform shape and it is centered around $r_{21} = r_{31} = 0$, where initial placement is most likely. Due to the strong localisation of the distribution at time t_{fin} , its maximum is much larger than any value of the distribution time t_{init} . Therefore, all values of the initial distribution in Fig. 5.8(b) are close to zero when the distribution's largest peak at time t_{fin} is taken as a benchmark. As shown in Figs. 5.9(a) and 5.9(b) peaks corresponding to bound states have already started to develop at intermediate time $t_{\text{itm}} = t_{\text{fin}}/2$. The form of the probability distribution agrees with the

dissipative potentials of Figs. 5.6 and 5.7. Comparing the different benchmarked plots in Figs. 5.9(a) and 5.9(b) reveals once again how strongly localised the distribution at time t_{fin} is. This trend of emerging peaks in the distribution continues and results in the final distribution at time t_{fin} , which is shown in Fig. 5.10(b). Again, the development of the probability distribution agrees with the dissipative potentials of Figs. 5.6 and 5.7. Like the two-atom distributions in Fig. 4.8, the three-atom distributions at times t_{init} and t_{fin} in Fig. 5.10 show that the system starts as quasi-uniform distribution, where all atomic configurations are equally likely, and arrives at a distribution, where the equilateral triangle constellation with $r_{21} = r_{31} = (2.34 \pm 0.29) \cdot r_0$ and $\Theta = 60^\circ$ is most probable.

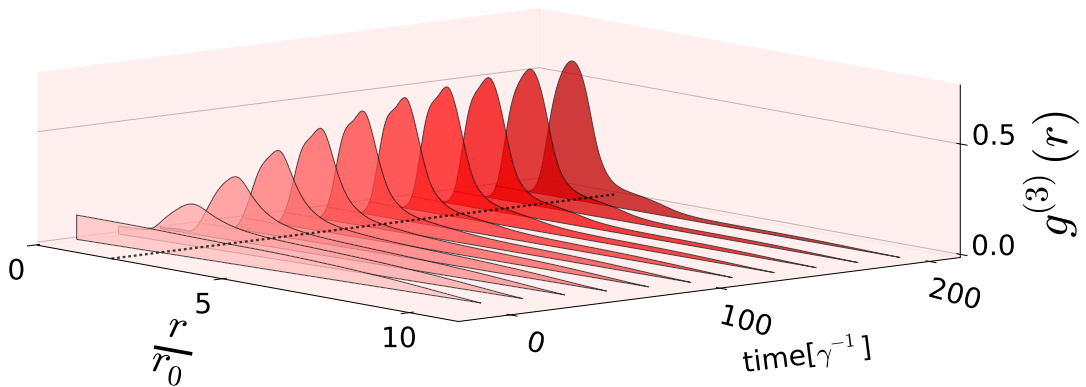


Figure 5.11.: The function $g^{(3)}(r)$ of the simulated three-atom system with optimised parameters at increasing times is shown. The dotted black line indicates the most probable interatomic distance at an equilateral triangle configuration with $r_{21} = r_{31} = r_{23} = r$ and $\Theta = 60^\circ$.

The function $g^{(3)}(r)$ yields the probability of finding the three-atom system at interatomic distance r , when the three-atoms are confined to an equilateral triangle configuration with $r_{21} = r_{31} = r_{23} = r$ and $\Theta = 60^\circ$. While, in a certain sense, it is the extension of the two-atom pair correlation function $g^{(3)}(r)$, which defines the probability of finding two atoms at an interatomic distance r , to three atoms, it must not be confused with the three-atom pair correlation function. In Fig. 5.11 the evolution of function $g^{(3)}(r)$ in time is depicted. The graphs in Fig. 5.11 were plotted using interpolation of the originally calculated data over distance r . Similarly to Fig. 4.9 a distinct maximum emerges during the course of the simulation. The location of the maximum of function $g^{(3)}(r)$ at $r = (2.10 \pm 0.29) \cdot r_0$ agrees with the position of the peaks in Fig. 5.10(b) at opening angle $\Theta = 60^\circ$.

Additionally, in order to prove that the atomic configuration with the highest probability actually is at $\Theta = 60^\circ$, the three-atom probability distribution of the isosceles triangle constellation with $r = r_{21} = r_{31}$ and variable Θ was calculated. The resulting plots at times t_{init} , t_{itm} , and t_{fin} are displayed in Fig. 5.12. These plots indicate a time evolution of the three-atom system from a quasi-uniform

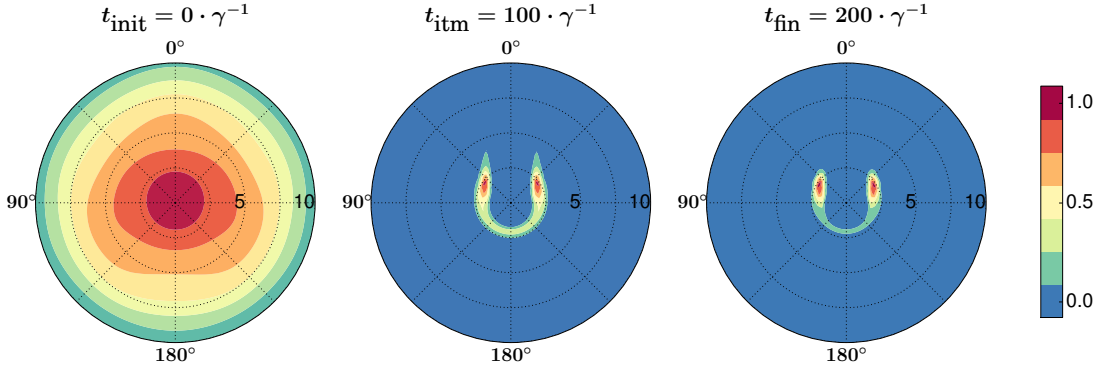


Figure 5.12.: The plots of the averaged three-atom probability distribution with optimised parameter values are shown in the isosceles configuration at times t_{init} , t_{itm} , and t_{fin} . The radial axis represents interatomic distances $r_{21} = r_{31} = r$ divided by r_0 , whereas the polar axis indicates opening angle Θ . The distributions are given in arbitrary units with the largest value corresponding to the largest peak of the atom distribution at the respective time.

distribution, where all opening angles Θ are equally likely, to a distribution, where only a certain range of r is probable and the total maxima of the probability distribution are situated at $\Theta = \pm 60^\circ$. While the probability of finding the atoms at interatomic distance $r_{21} = r_{31} = r$ is only significant in a confined range, opening angle Θ of the distribution at time t_{fin} has non-negligible probability in a range between 45° and 90° , with 60° being the aforementioned maximum. The broadness of this distribution in comparison to the two-atom distribution in Sec. 4.2 is a consequence of more geometric configurations being available due to the additional third atom.

The peak of the distribution at $\Theta = 60^\circ$ in Fig. 5.10, the emerging maximum of function $g^{(3)}(r)$ in Fig. 5.11, and the final state at time t_{fin} in Fig. 5.12 all clearly prove that the examined two-dimensional three-atom system exhibits dissipatively bound trimer states. Again, we can define an imaginary binding energy $E_b^{(3)} = \Delta V_d^{(3)} = 6.25 \cdot 10^{-2} \cdot \hbar\gamma$, which determines the amount of dissipation required in order to dissociate the three-atom bond. Whereas the total three-atom binding energy $E_b^{(3)}$ for optimised parameter values is larger than in the two-atom case, the two-atom binding energy per atom $e_b^{(2)} = E_b^{(2)}/2$ is larger than the three-atom binding energy per-atom $e_b^{(3)} = E_b^{(3)}/3$ by a factor of $e_b^{(2)}/e_b^{(3)} = 1.35$.

6. Dissipative Borromean States

*But I always say,
one's company,
two's a crowd,
and three's a party.*

—Andy Warhol

Now, after finding metastable dissipatively bound states for two atoms (see Chap. 4) and three atoms (see Chap. 5), the goal of this chapter is to find a Borromean state, which is also a trimer state. This state, however, whose name derives from the aristocratic Borromeo family in Northern Italy [51], is characterised by the fact that the bound state only forms for three atoms, whereas removing one of them leads to an unbound state. A famous example of such a Borromean state is the Efimov state, which is caused by the effect of the same name [52]. While the concept of Borromean states is introduced in Sec. 6.1, our efforts of finding a dissipative analogon of such a state are discussed in Secs. 6.2 and 6.3.

6.1. Borromean States

The concept of Borromean states derives from a special kind of topological link in mathematics. This link connects three rings, known as Borromean rings, together in such a way that removing any ring results in two unlinked rings. Put differently, although all three rings are linked together, no two of the three rings are linked. An exemplary depiction of Borromean rings is shown in Fig. 6.1(a). It is important to note that the perception of three flat rings in this image is an optical illusion, it is actually impossible to connect three flat rings in such a way. The name of Borromean rings and therefore of Borromean states stems from the aristocratic Borromeo family in Northern Italy [51], who used the three rings as a symbol to express their strength through unity.

In physics, Borromean states are the physical analogon of Borromean rings, i.e., bound trimer states of atoms or molecules that do not exhibit any dimer state, when one of the binding partners is removed. This few-body phenomenon has been studied in a wide variety of classical scientific disciplines. In chemistry, it is possible to interlock three cyclic macromolecules in order to form molecular Borromean rings. One example, which can be seen in Fig. 6.1(b), is the so-called

Borromeate, which consists of three interpenetrated macrocycles formed from the reaction between 2,6-diformylpyridine and diamine compounds, complexed with zinc. It was first synthesised in 2004 by Sir James Fraser Stoddart [50], who, among others, was awarded the Nobel Prize in Chemistry 2016 for the design and synthesis of molecular machines.

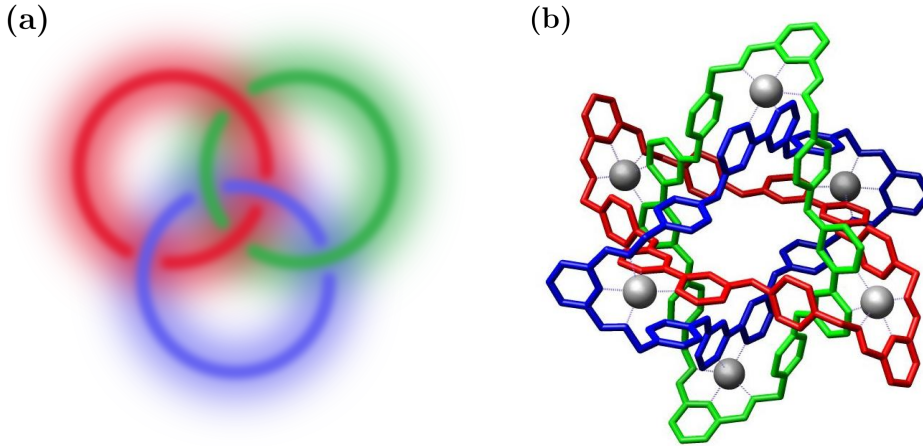


Figure 6.1.: Subpanel (a) depicts a set of Borromean rings. It is important to note that three flat circles can actually not be constructed in this way. Subpanel (b) shows the crystal structure of a set of molecular Borromean rings, known as Borromeate, which was taken from [85].

In quantum physics, Borromean states appear as well, but in contrast to the classical regime, they are based on quantum few-body effects, as opposed to physical or topological restriction. A well-known example in atomic physics is the Efimov state, a novel and exotic state of matter, which was theoretically proposed by Vitaly N. Efimov in 1970 [52]. Not only does this state constitute a Borromean state of three identical bosons, but it also exhibits an infinite series of excited states, whose energy levels converge towards the dissociation threshold. These states are completely identical except that their binding lengths and energy levels scale by a universal factor, which, in the case of three identical bosons, is approximately 22.7.

Due to the efforts of experimentalists in the field, it was possible to experimentally prove the existence of the Efimov state and find its first excited state in a cloud of caesium atoms [53]. Furthermore, the observation of Efimov states in an ultracold mixture of lithium and caesium atoms extended Efimov's original picture of three identical bosons [55].

While many few-body phenomena, which were originally found in closed systems in equilibrium settings, have been studied and discovered in the context of open quantum systems [44–46], a dissipative analogon of the Borromean state remains to be found. In the next section, we will discuss the search for parameter

values, which potentially could give rise to a Borromean state using the binding method proposed by Lemeshko and Weimer.

6.2. Finding Borromean Parameter Values

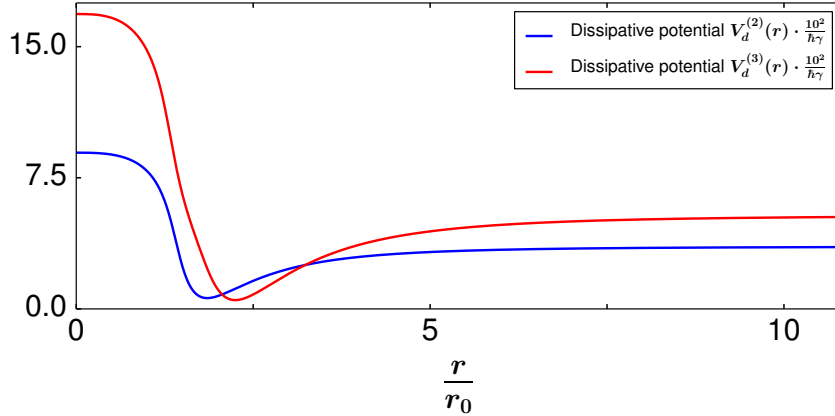


Figure 6.2.: The effective dissipative n -atom potentials $V_d^{(n)}(r)$ with Borromean parameter values are displayed for $n = 2$ and $n = 3$. $V_d^{(3)}(r)$ was calculated assuming an equilateral triangle configuration. Parameter values used are listed in Tab. 6.1.

In order to prove that a dissipative Borromean state exists, we need to find a set of values for parameters Ω_{21} , Ω_{23} , Δ_{21} , and Δ_{23} that, when applied to a two-dimensional three-atom system leads to a dissipatively bound trimer state, but yields no bound state when applied to a two-dimensional two-atom system. In this section a potential set of such parameter values, which was achieved in a similar fashion to Secs. 4.1 and 5.1, is presented and the resulting effective dissipative potentials $V_d^{(n)}(r)$ are analysed. $V_d^{(3)}(r)$ was calculated assuming an equilateral triangle configuration. By continuously removing one atom, the equivalence of $V_d^{(3)}(r)$ and $V_d^{(2)}(r)$ is shown in Fig. C.14 of Appendix C.

Ω_{21}	Ω_{23}	Δ_{21}	Δ_{23}	d
$0.375 \cdot \gamma$	$0.05 \cdot \gamma$	$0.475 \cdot \gamma$	$-0.08 \cdot \gamma$	8.85 D

Table 6.1.: Parameter values optimised for the Borromean state.

The Borromean parameter values should yield a dissipative two-atom potential $V_d^{(2)}(r)$, which does not exhibit any minimum, such as the green graph in Fig. 4.1, but still maintain a minimum for the dissipative three-atom potential $V_d^{(3)}(r)$. This proved to be impossible, as the only way to achieve such a dissipative two-atom potential is to drive the transitions resonantly. This, however, always

results in both dissipative potentials, $V_d^{(2)}(r)$ and $V_d^{(3)}(r)$, being without any minimum. Furthermore, as discussed in Sec. 5.2, the two-atom bond seems to be at least as strong as the three-atom bond, complicating our endeavour of finding a dissipative Borromean state.

n	$\frac{r_{\min}}{r_0}$	$\frac{V_d^{(n)}(r_{\min})}{\hbar\gamma} \cdot 10^2$	$\frac{V_d^{(n)}(0)}{\hbar\gamma} \cdot 10^2$	$\frac{V_d^{(n)}(\infty)}{\hbar\gamma} \cdot 10^2$	$\frac{\Delta V_d^{(n)}}{\hbar\gamma} \cdot 10^2$
2	1.85	0.62	8.94	3.54	2.92
3	2.25	0.50	16.87	5.26	4.75

Table 6.2.: Important quantities of $V_d^{(2)}(r)$ and $V_d^{(3)}(r)$ for Borromean parameter values.

Therefore, the Borromean parameter values were achieved by finding the best trade-off between minimising the potential depth $\Delta V_d^{(2)}$ and still maintaining some minimum in $V_d^{(3)}(r)$. The most suitable parameter values for these conditions are shown in Tab. 6.1 and the corresponding dissipative potentials $V_d^{(n)}(r)$ are shown in Fig. 6.2. While both $V_d^{(3)}(r)$ and $V_d^{(2)}(r)$ in Fig. 6.2 exhibit a minimum that could lead to binding, the small depth $\Delta V_d^{(2)}$ leaves room for the supposition, that kicks due to photon scattering might prevent a metastable dimer state. The difference between $V_d^{(3)}(r_{\min})$ and $V_d^{(3)}(\infty)$, on the other hand, is noticeably larger as can be seen in Tab. 6.2. However, if one considers the quantities calculated per atom, which are listed in Tab. 6.3, both systems have fairly similar properties, weakening the validity of our assumption that a Borromean state will form. The effective dissipative potentials per atom $\frac{1}{n}V_d^{(n)}(r)$, whose properties differ only marginally, are viewed in Fig. C.13 in Appendix C.

n	$\frac{1}{n} \frac{V_d^{(n)}(r_{\min})}{\hbar\gamma} \cdot 10^2$	$\frac{1}{n} \frac{V_d^{(n)}(0)}{\hbar\gamma} \cdot 10^2$	$\frac{1}{n} \frac{V_d^{(n)}(\infty)}{\hbar\gamma} \cdot 10^2$	$\frac{1}{n} \frac{\Delta V_d^{(n)}}{\hbar\gamma} \cdot 10^2$
2	0.31	4.47	1.77	1.46
3	0.17	5.62	1.75	1.58

Table 6.3.: Important quantities of $V_d^{(2)}(r)$ and $V_d^{(3)}(r)$ calculated per atom for Borromean parameter values.

In the next section the simulations of two- and three-atom systems are presented in order to examine the obtained parameter values' ability to give rise to a Borromean state.

6.3. Simulation

In this section the results of a simulation of a two-dimensional two-atom system and of a two-dimensional three-atom system are presented. Both systems were simulated using the parameter values from Tab. 6.1 in order to prove that these

parameters lead to binding in the three-atom case, while not exhibiting any bound state in the two-atom case. The following plots were obtained by generating 1000 realisations of each system using the adapted MCWF simulation method described in Sec. 3.2. The reader is referred to Fig. C.12 in Appendix C for a more thorough account of the two-atom simulation's results. Likewise, the three-atom simulation is displayed with a higher time-resolution in Figs. C.7 to C.11 of Appendix C.

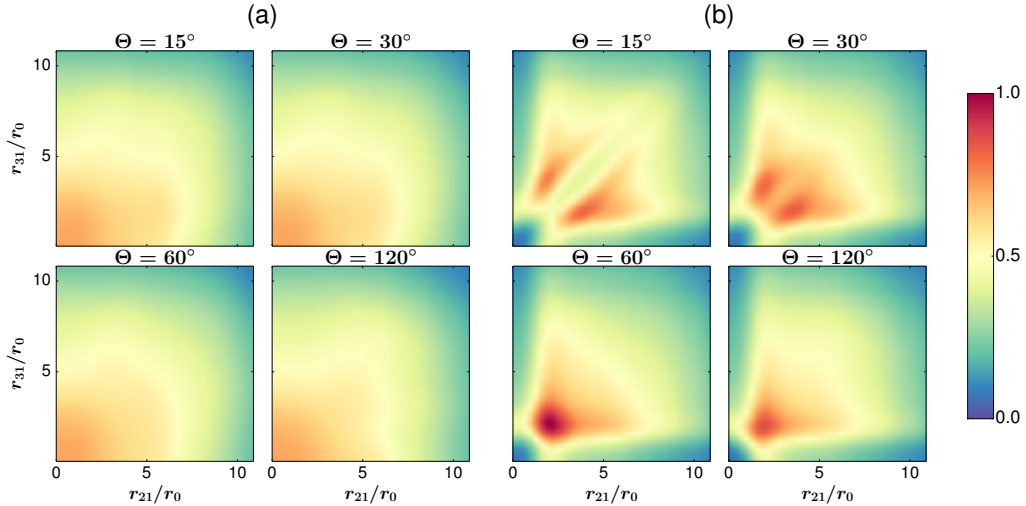


Figure 6.3.: The averaged three-atom probability distributions (a) at time $t_{\text{init}} = 0 \cdot \gamma^{-1}$ and (b) at time $t_{\text{fin}} = 200 \cdot \gamma^{-1}$ are shown. The coordinates of the axes represent interatomic distances r_{21} and r_{31} . The distributions are given in arbitrary units with the largest value corresponding to the largest peak of the atom distribution at time t_{fin} .

The simulation for the two-atom system was performed under the identical conditions and with the same discretisations as the simulation in Sec. 4.2, whereas the simulation for the three-atom system was done using the conditions of Sec. 5.2. Figures 6.3(a) and 6.3(b) show the averaged three-atom probability distribution at time $t_{\text{init}} = 0 \cdot \gamma^{-1}$ and at time $t_{\text{fin}} = 200 \cdot \gamma^{-1}$, respectively. The distribution evolves from a quasi-uniform distribution to a distribution exhibiting a pronounced peak at an equilateral triangle configuration with $\Theta = 60^\circ$. While it is obvious that a three-atom bound state has formed at time t_{fin} , comparing it to the distribution in Fig. 5.10(b) reveals that the peak is less pronounced, which can be explained by the less favourable dissipative three-atom potential $V_d^{(3)}$ in Fig. 6.2. This can also be seen by examining the plots of three-atom distributions with optimised parameters in the isosceles configuration in Fig. 5.12 and the analogous plots with Borromean parameters in Fig. C.15 of Appendix C.

The averaged probability distribution of the two-atom system with Borromean parameter values is displayed at time t_{init} in Fig. 6.4(a) and at time t_{fin} in Fig. 6.4(b). Again, the evolution from a quasi-uniform distribution to a ring-

like peak can be observed. Although the ringlike peak is less pronounced than the peak in Fig. 4.8(b), a dimer state still has formed at time t_{fin} .

Therefore, our efforts of finding parameter values that yield a dissipative Borromean state were not successful. This leads to the conclusion that the dissipative binding method used in this thesis is not able to form Borromean states.

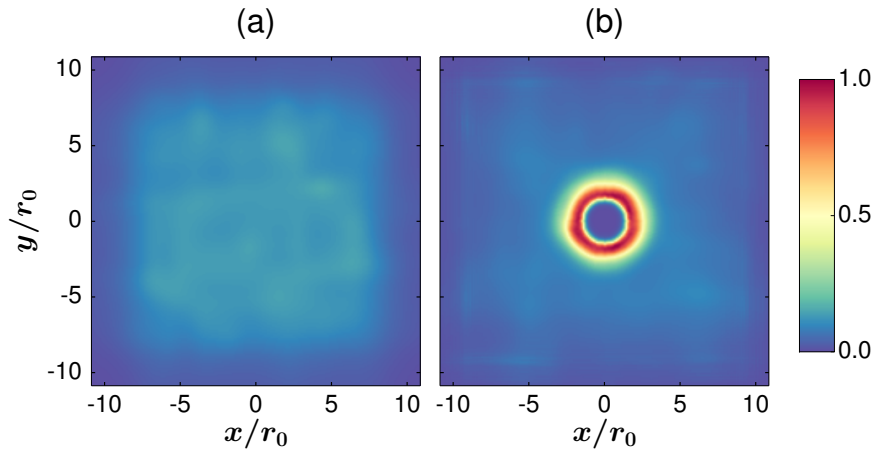


Figure 6.4.: The averaged two-atom probability distributions in relative x - and y -coordinates (a) at time $t_{\text{init}} = 0 \cdot \gamma^{-1}$ and (b) at time $t_{\text{fin}} = 200 \cdot \gamma^{-1}$ are shown. The distributions are given in arbitrary units with the largest colour value corresponding to the largest peak of the atom distribution at time t_{fin} in both subpanels.

7. Conclusion

*Ende und Ziel: Nicht jedes Ende ist das Ziel. Das Ende der Melodie ist nicht deren Ziel; aber trotzdem: hat die Melodie ihr Ende nicht erreicht, so hat sie auch ihr Ziel nicht erreicht. Ein Gleichnis.
(End and Goal: Not every end is a goal. The end of a melody is not its goal; but nonetheless, if the melody had not reached its end it would not have reached its goal either. A parable.)*

—Friedrich Nietzsche, *Der Wanderer und sein Schatten*[86]

Within the scope of this thesis, the dissipative binding method proposed by Lemeshko and Weimer [32, 33] was extended and improved. Furthermore, a novel simulation technique, which is based on the MCWF method, was developed specifically for the examined systems. This adapted MCWF method reduces the size of the Hilbert space and therefore the necessary computing power by integrating out the internal electronic energy structure and replacing the relevant details by the effective dissipative n -atom potential $V_d^{(n)}(\{r_{ij}\})$.

Using this new technique, we successfully extended the dissipative binding method to dimer and trimer states in two dimensions. The system parameter values were optimised in order to maximise the strength of the dissipatively bound metastable states. These dissipative bonds arise even though only repulsive forces are present in our setup. One of the initial goals, finding a dissipatively bound Borromean state, could not be achieved via the presented approach. A more complicated setup, which lends more importance to inherent three-body effects, might show more promise in achieving this goal.

The experimental implementation of the proposed systems can be done using techniques well-established in the area of ultracold quantum gases. The difficulty of realising the setups lies in correctly tuning the dipole-dipole interaction to avoid undesired mixing of state $|1\rangle_a$ with the highly excited Rydberg state $|\text{Ry}\rangle_a$. One appropriate setup would be a many-body system with initially uncorrelated atoms. By choosing the correct atom density, an average interatomic distance larger than the binding distance is guaranteed and few-body interactions higher than the three-body interaction can be ignored. The usual densities of ultracold Rydberg gases created with current experimental methods [66–72] are exactly such that only few-body processes play a significant role. Thus, these techniques supply us with perfectly suitable Rydberg samples. The resulting dissipative bonds are not fragile, since they are prepared as an attractor of the driven-dissipative dynamics. They emerge irrespectively of the initial conditions.

These bound states can be detected by measuring the pair correlation function using present-day spectroscopic methods. Finally, a significant advantage of our method, in contrast to other proposals, is that preservation of coherence is not needed.

As in closed systems, the potential extension to four [87] or more [88] particles is an intriguing venue. This way, the transition from few- to many-body systems can be explored, similarly to closed systems [89–91]. The shape of the dissipatively bound three-atom state indicates that an appropriate many-body state can form a triangular lattice, which would correspond to a dissipatively bound crystal [31]. This type of binding mechanism enables cooling to a strongly interacting phase without the use of an optical lattice and therefore preserving translational symmetry.

A. Supplementary Theory

A.1. Rabi Oscillations

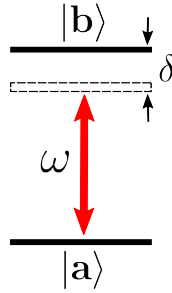


Figure A.1.: Two-level system driven with frequency ω and detuning δ .

When considering the interaction of a two-level atom with an incident light field of frequency ω , it is intuitive to split the Hamiltonian into an unperturbed part \hat{H}_0 and an interaction part \hat{H}_I . A depiction of an exemplary two-level system is displayed in Fig. A.1. The free Hamiltonian \hat{H}_0 consists of the respective eigenstates and energy eigenvalues:

$$\hat{H}_0 = \hbar\omega_a |a\rangle \langle a| + \hbar\omega_b |b\rangle \langle b| . \quad (\text{A.1})$$

Assuming that the light field is linearly polarised along the x -axis and using the dipole approximation, we can write the operator for the interaction energy between the atom and the field as:

$$\begin{aligned} \hat{H}_I &= -\hat{\mathbf{d}}\mathbf{E} = -e\hat{x}E = -eE \sum_{i=a,b} \sum_{j=a,b} |i\rangle \langle i| \hat{x} |j\rangle \langle j| \\ &= -d_x E (|a\rangle \langle b| + |b\rangle \langle a|) , \end{aligned} \quad (\text{A.2})$$

where e denotes the elementary charge and $d_x = x_{ab} = x_{ba}$ is the matrix element of the atomic dipole moment, which is assumed to be real in this case. By introducing the electric component of the light field $E(t) = E_0 (e^{i\omega t} + e^{-i\omega t}) / 2$, we can write:

$$\begin{aligned}
 \hat{H}_I &= -\frac{\Omega\hbar}{2} (e^{i\omega t} + e^{-i\omega t}) (|a\rangle\langle b| + |b\rangle\langle a|) \\
 &= -\frac{\Omega\hbar}{2} (|a\rangle\langle b| e^{-i\omega t} + |b\rangle\langle a| e^{i\omega t}) , \\
 &\text{with } \Omega = \frac{d_x E_0}{\hbar} .
 \end{aligned} \tag{A.3}$$

Here, we applied the so-called rotating-wave approximation and neglected terms, which rotate fast with frequency $\omega + \omega_{ab}$ in the expectation value, while leaving terms that vary slowly with frequency $\omega - \omega_{ab}$. Frequency ω_{ab} is defined by the energy difference of states $|a\rangle$ and $|b\rangle$: $\omega_{ab} = \omega_a - \omega_b$.

Therefore, we have derived the full Hamiltonian $\hat{H} = \hat{H}_0 + \hat{H}_I$ in the dipole approximation and the rotating-wave approximation. Assuming an arbitrary wave-function $|\psi(t)\rangle = \alpha(t)|a\rangle + \beta(t)|b\rangle$, we now want to solve the Schrödinger equation:

$$i\hbar \frac{d}{dt} |\psi(t)\rangle = \hat{H} |\psi(t)\rangle . \tag{A.4}$$

By applying the substitutions $A(t) = \alpha(t)e^{i\omega_a t}$ and $B(t) = \beta(t)e^{i\omega_b t}$, we find the following differential equations:

$$\begin{aligned}
 \dot{A}(t) &= \frac{i\Omega}{2} e^{-i\delta t} B(t) , \\
 \dot{B}(t) &= \frac{i\Omega}{2} e^{i\delta t} A(t) ,
 \end{aligned} \tag{A.5}$$

with detuning $\delta = \omega_{ab} - \omega$. In the resonant case ($\delta = 0$), the general solutions with initial conditions $A(0)$ and $B(0)$ can be written as:

$$\begin{aligned}
 A(t) &= A(0) \cos\left(\frac{\Omega t}{2}\right) + iB(0) \sin\left(\frac{\Omega t}{2}\right) , \\
 B(t) &= B(0) \cos\left(\frac{\Omega t}{2}\right) + iA(0) \sin\left(\frac{\Omega t}{2}\right) .
 \end{aligned} \tag{A.6}$$

The populations of states $|a\rangle$ and $|b\rangle$, which are described by $p_a(t) = |\alpha(t)|^2 = |A(t)|^2$ and $p_b(t) = |\beta(t)|^2 = |B(t)|^2$, respectively, oscillate in time with Rabi frequency Ω :

$$\begin{aligned}
 p_a(t) &= |\alpha(0)|^2 \cos\left(\frac{\Omega t}{2}\right) + |\beta(0)|^2 \sin\left(\frac{\Omega t}{2}\right) , \\
 p_b(t) &= |\beta(0)|^2 \cos\left(\frac{\Omega t}{2}\right) + |\alpha(0)|^2 \sin\left(\frac{\Omega t}{2}\right) , \\
 &\text{with } p_a(t) + p_b(t) = 1 .
 \end{aligned} \tag{A.7}$$

These so-called Rabi oscillations are caused by the driving light field and their frequency Ω is proportional to the electric field amplitude E_0 . As $p_a(t)$ and $p_b(t)$ describe the probability of finding the atom in state $|a\rangle$ or state $|b\rangle$, respectively, the oscillations mean that atom jumps back and forth between the ground state and the excited state. These oscillations are not to be confused with the optical oscillations occurring with frequency ω .

The reader is referred to the literature [62, 76] for a derivation of the general solution including non-zero detuning δ .

B. Caesium Data

Atomic Number	Z	55
Total Nucleons	$Z + N$	133
Relative Natural Abundance	$\eta(^{133}\text{Cs})$	100%
Atomic Mass	m	132.905451931(27) u $2.20694650(17) \cdot 10^{-25}$ kg
Nuclear Lifetime	τ_n	(stable)
Density at 25°C	ρ_m	1.93 g/cm ³
Melting Point	T_M	28.44°C
Boiling Point	T_B	671°C
Nuclear Spin	I	7/2

Table B.1.: Essential caesium properties taken from [92].

Frequency	ω_0	$2\pi \cdot 351.72571850(11)$ THz
Transition Energy	$\hbar\omega_0$	1.454620542(53) eV
Wavelength (Vacuum)	λ	852.34727582(27) nm
Lifetime	τ	30.473(39) ns
Decay Rate/ Natural Line Width (FWHM)	Γ	$32.815(41) \cdot 10^6$ s ⁻¹ $2\pi \cdot 5.2227(66)$ MHz
Recoil Velocity	v_r	3.5225 mm/s
Recoil Energy	ω_r	$2\pi \cdot 2.0663$ kHz
Recoil Temperature	T_r	198.34 nK

Table B.2.: Optical properties of the caesium D₂ transition ($6^2\text{S}_{1/2} \rightarrow 6^2\text{P}_{3/2}$) taken from [92].

C. Supplementary Results

This part of the appendix contains supplementary results for two- and three-atom systems with optimised parameter values (see Tabs. 4.3 and 5.1) and Borromean parameter values (see Tab. 6.1). The axes of plots in Figs. C.1 to C.12 indicate relative distances and are given in units of the characteristic dipole-dipole interaction length r_0 from Eq. (3.19). The three-atom distributions in Figs. C.2 to C.11 are displayed at various opening angles Θ , whose geometric position is shown in Fig. 2.2(b).

A detailed account of the averaged two-atom distribution's change in time from initial time $t_{\text{init}} = 0 \cdot \gamma^{-1}$ to time $t_9 = 180 \cdot \gamma^{-1}$ is shown in Figs. C.1 and C.12 for optimised parameter values and for Borromean parameter values, respectively. Similarly, the evolution of the averaged three-atom distributions with optimised parameter values from initial time $t_{\text{init}} = 0 \cdot \gamma^{-1}$ to time $t_9 = 180 \cdot \gamma^{-1}$ can be seen in detail in Figs. C.2 to C.6, while the same time evolution of the averaged three-atom distributions with Borromean parameter values is displayed in Figs. C.7 to C.11. The averaged few-atom probability distributions at final time $t_{\text{fin}} = 200 \cdot \gamma^{-1}$ are not included in this part of the appendix. For the final two-atom distributions with optimised and Borromean parameter values the reader is referred to Figs. 4.8 and 6.4, respectively, whereas the final three-atom distributions with optimised and Borromean parameter values are given in Figs. 5.10 and 6.3, respectively.

Furthermore, the effective dissipative n -atom potentials calculated per atom are shown for $n = 2$ and $n = 3$ in Fig. C.13, whereas plots of the averaged three-atom probability distribution in the isosceles configuration are displayed at times t_{init} , t_{itm} , and t_{fin} in Fig. C.15. The plots in both figures were calculated using the Borromean parameter values of Tab. 6.1. Finally, the equivalence of two- and three-atom potentials is shown by continuously removing one atom in the three-atom case in Fig. C.14.

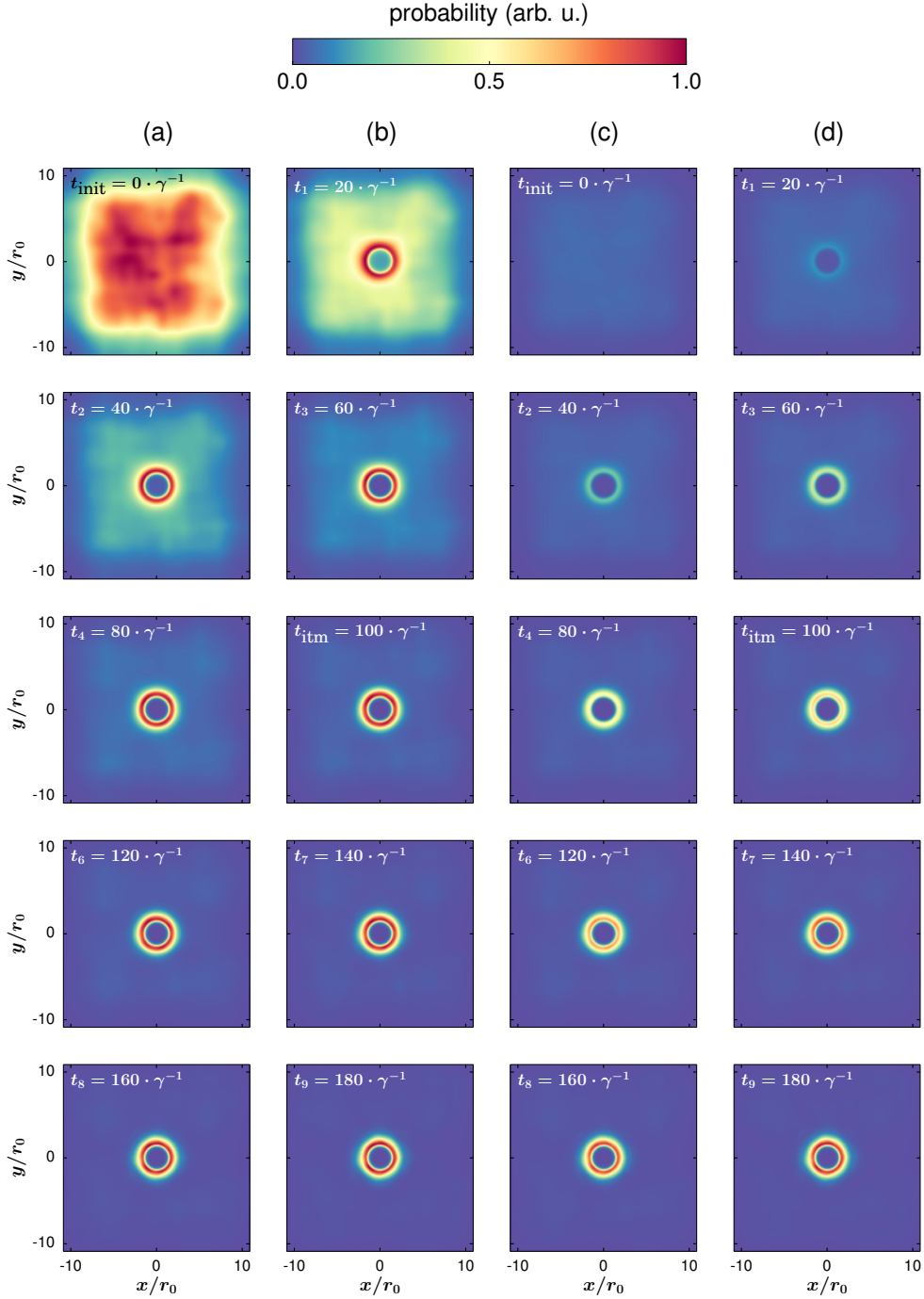


Figure C.1.: The two-atom probability distribution with optimised parameter values (see Tab. 4.3) is shown at increasing times t_n . The distributions are given in arbitrary units with the largest colour value corresponding to the largest peak at respective time t_n in columns (a) and (b), while the largest colour value in columns (c) and (d) corresponds to the largest peak at time $t_{\text{fin}} = 200 \cdot \gamma^{-1}$.

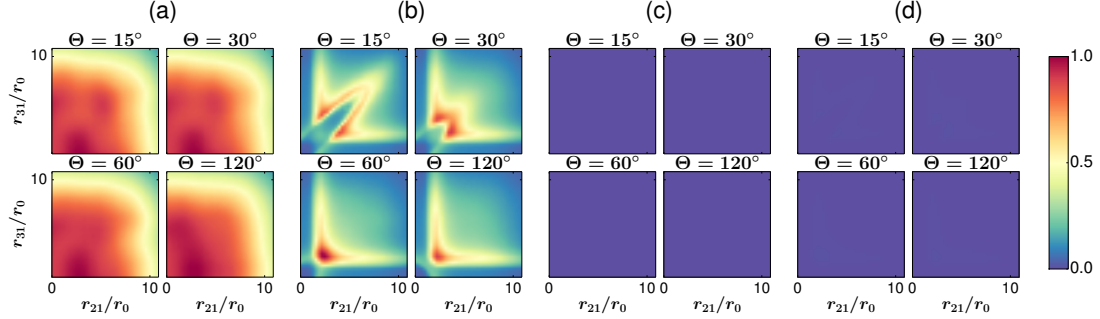


Figure C.2.: The three-atom probability distributions with optimised parameter values (see Tab. 5.1) are shown at initial time $t_{\text{init}} = 0 \cdot \gamma^{-1}$ (subpanels (a) and (c)) and at time $t_1 = 20 \cdot \gamma^{-1}$ (subpanels (b) and (d)). The distributions are given in arbitrary units with the largest colour value corresponding to the largest peak at times t_{init} and t_1 in subpanels (a) and (b), respectively, whereas the largest colour value in subpanels (c) and (d) corresponds to the largest peak at time $t_{\text{fin}} = 200 \cdot \gamma^{-1}$.

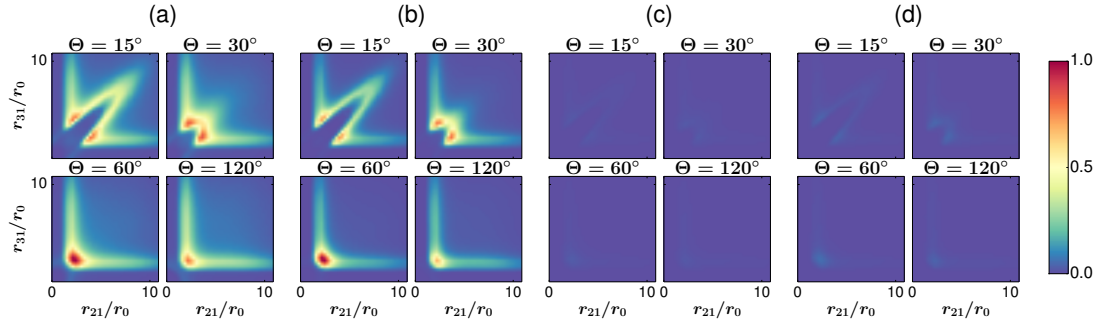


Figure C.3.: The three-atom probability distributions with optimised parameter values (see Tab. 5.1) are shown at time $t_2 = 40 \cdot \gamma^{-1}$ (subpanels (a) and (c)) and at time $t_3 = 60 \cdot \gamma^{-1}$ (subpanels (b) and (d)). The distributions are given in arbitrary units with the largest colour value corresponding to the largest peak at times t_2 and t_3 in subpanels (a) and (b), respectively, whereas the largest colour value in subpanels (c) and (d) corresponds to the largest peak at time $t_{\text{fin}} = 200 \cdot \gamma^{-1}$.

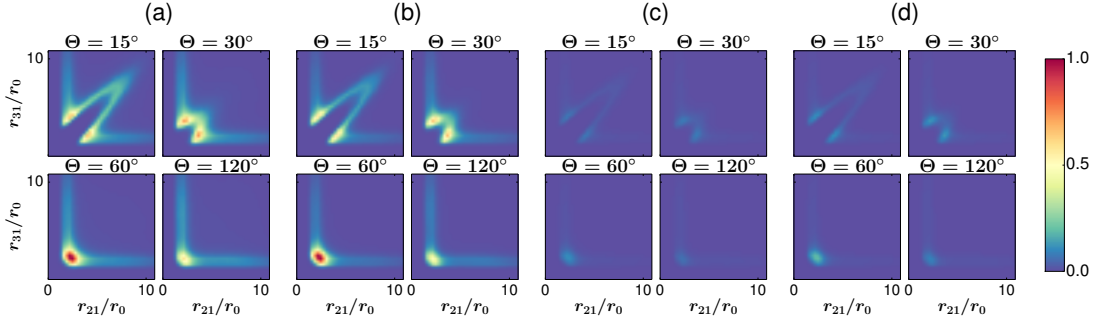


Figure C.4.: The averaged three-atom probability distributions with optimised parameter values (see Tab. 5.1) are shown at time $t_4 = 80 \cdot \gamma^{-1}$ (subpanels (a) and (c)) and at intermediate time $t_{\text{itm}} = 100 \cdot \gamma^{-1}$ (subpanels (b) and (d)). The distributions are given in arbitrary units with the largest colour value corresponding to the largest peak at times t_4 and t_{itm} in subpanels (a) and (b), respectively, whereas the largest colour value in subpanels (c) and (d) corresponds to the largest peak at time $t_{\text{fin}} = 200 \cdot \gamma^{-1}$.

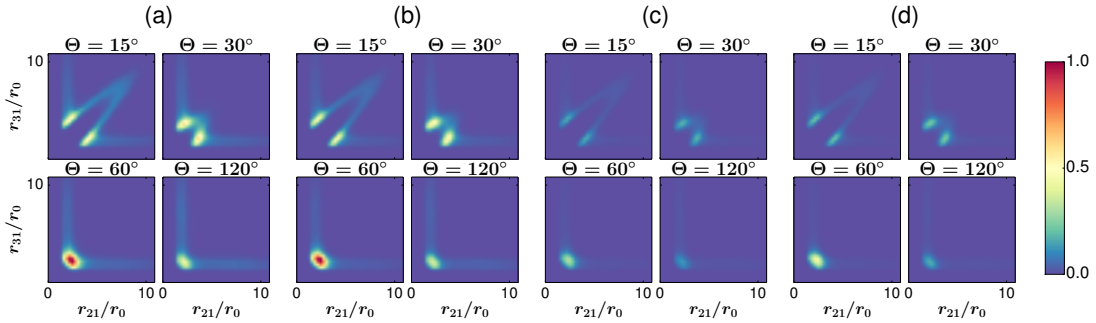


Figure C.5.: The three-atom probability distributions with optimised parameter values (see Tab. 5.1) are shown at time $t_6 = 120 \cdot \gamma^{-1}$ (subpanels (a) and (c)) and at time $t_7 = 140 \cdot \gamma^{-1}$ (subpanels (b) and (d)). The distributions are given in arbitrary units with the largest colour value corresponding to the largest peak at times t_6 and t_7 in subpanels (a) and (b), respectively, whereas the largest colour value in subpanels (c) and (d) corresponds to the largest peak at time $t_{\text{fin}} = 200 \cdot \gamma^{-1}$.

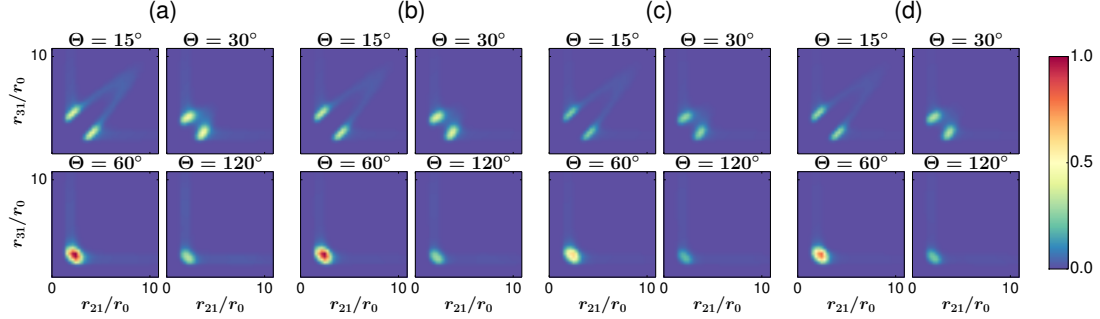


Figure C.6.: The three-atom probability distributions with optimised parameter values (see Tab. 5.1) are shown at time $t_8 = 160 \cdot \gamma^{-1}$ (subpanels (a) and (c)) and at time $t_9 = 180 \cdot \gamma^{-1}$ (subpanels (b) and (d)). The distributions are given in arbitrary units with the largest colour value corresponding to the largest peak at times t_8 and t_9 in subpanels (a) and (b), respectively, whereas the largest colour value in subpanels (c) and (d) corresponds to the largest peak at time $t_{\text{fin}} = 200 \cdot \gamma^{-1}$.

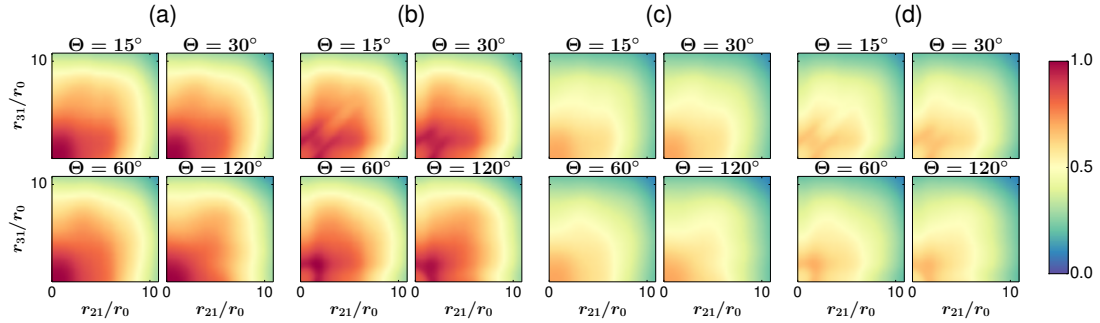


Figure C.7.: The three-atom probability distributions with Borromean parameter values (see Tab. 6.1) are shown at initial time $t_{\text{init}} = 0 \cdot \gamma^{-1}$ (subpanels (a) and (c)) and at time $t_1 = 20 \cdot \gamma^{-1}$ (subpanels (b) and (d)). The distributions are given in arbitrary units with the largest colour value corresponding to the largest peak at times t_{init} and t_1 in subpanels (a) and (b), respectively, whereas the largest colour value in subpanels (c) and (d) corresponds to the largest peak at time $t_{\text{fin}} = 200 \cdot \gamma^{-1}$.

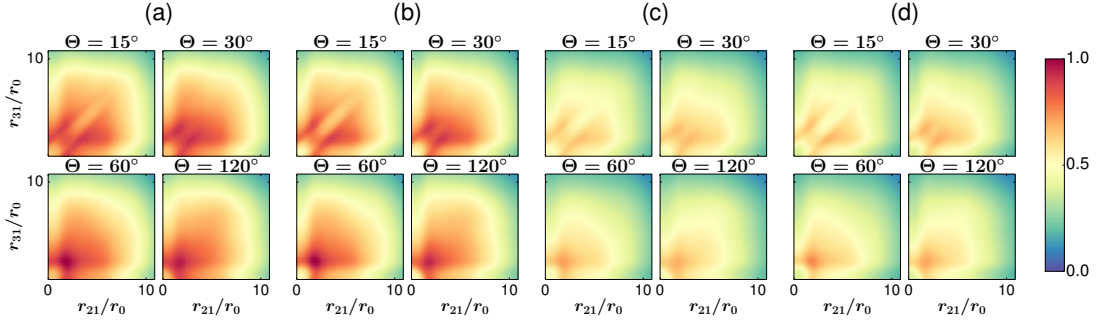


Figure C.8.: The three-atom probability distributions with Borromean parameter values (see Tab. 6.1) are shown at time $t_2 = 40 \cdot \gamma^{-1}$ (subpanels (a) and (c)) and at time $t_3 = 60 \cdot \gamma^{-1}$ (subpanels (b) and (d)). The distributions are given in arbitrary units with the largest colour value corresponding to the largest peak at times t_2 and t_3 in subpanels (a) and (b), respectively, whereas the largest colour value in subpanels (c) and (d) corresponds to the largest peak at time $t_{\text{fin}} = 200 \cdot \gamma^{-1}$.

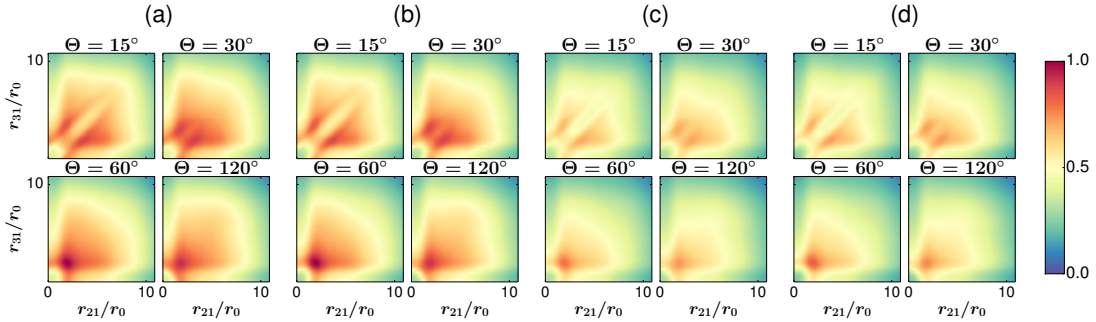


Figure C.9.: The averaged three-atom probability distributions with Borromean parameter values (see Tab. 6.1) are shown at time $t_4 = 80 \cdot \gamma^{-1}$ (subpanels (a) and (c)) and at intermediate time $t_{\text{itm}} = 100 \cdot \gamma^{-1}$ (subpanels (b) and (d)). The distributions are given in arbitrary units with the largest colour value corresponding to the largest peak at times t_4 and t_{itm} in subpanels (a) and (b), respectively, whereas the largest colour value in subpanels (c) and (d) corresponds to the largest peak at time $t_{\text{fin}} = 200 \cdot \gamma^{-1}$.

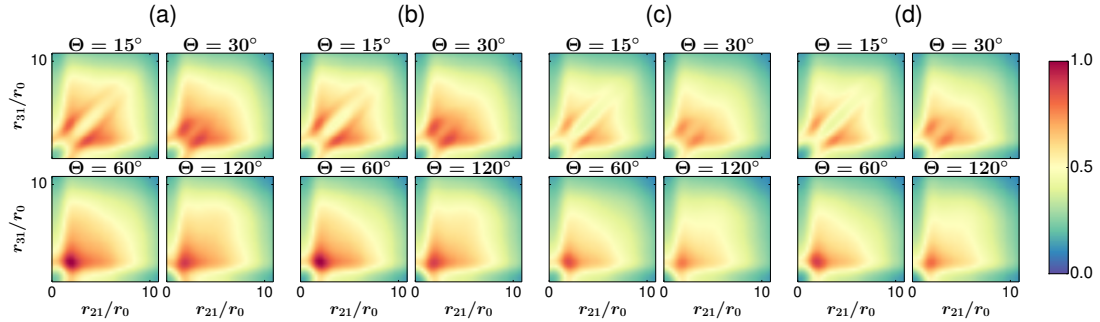


Figure C.10.: The three-atom probability distributions with Borromean parameter values (see Tab. 6.1) are shown at time $t_6 = 120 \cdot \gamma^{-1}$ (subpanels (a) and (c)) and at time $t_7 = 140 \cdot \gamma^{-1}$ (subpanels (b) and (d)). The distributions are given in arbitrary units with the largest colour value corresponding to the largest peak at times t_6 and t_7 in subpanels (a) and (b), respectively, whereas the largest colour value in subpanels (c) and (d) corresponds to the largest peak at time $t_{\text{fin}} = 200 \cdot \gamma^{-1}$.

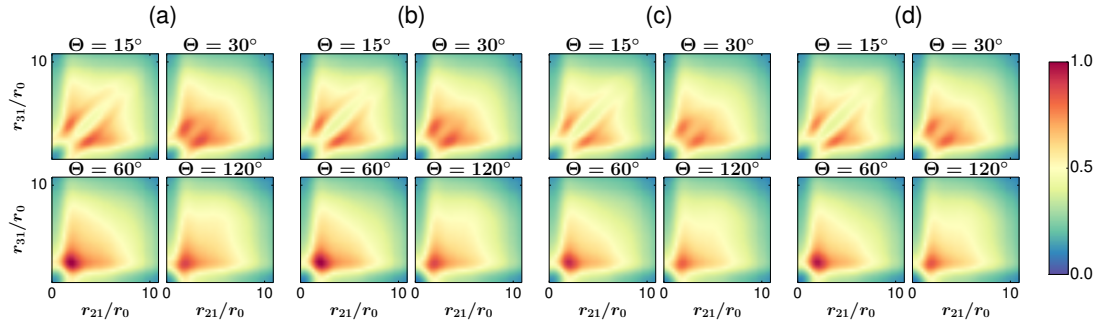


Figure C.11.: The three-atom probability distributions with Borromean parameter values (see Tab. 6.1) are shown at time $t_8 = 160 \cdot \gamma^{-1}$ (subpanels (a) and (c)) and at time $t_9 = 180 \cdot \gamma^{-1}$ (subpanels (b) and (d)). The distributions are given in arbitrary units with the largest colour value corresponding to the largest peak at times t_8 and t_9 in subpanels (a) and (b), respectively, whereas the largest colour value in subpanels (c) and (d) corresponds to the largest peak at time $t_{\text{fin}} = 200 \cdot \gamma^{-1}$.

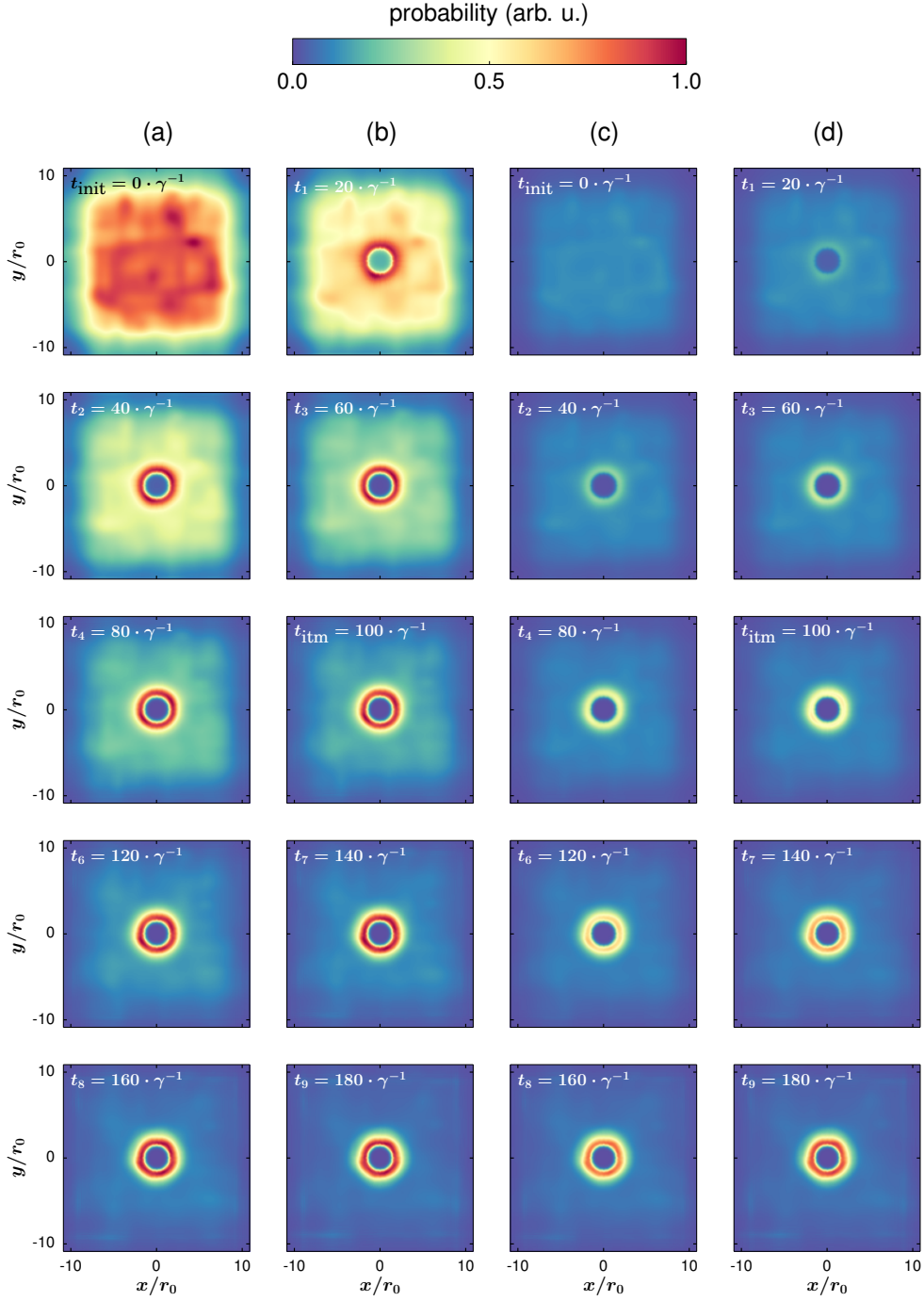


Figure C.12.: The two-atom probability distribution with Borromean parameter values (see Tab. 6.1) is shown at increasing times t_n . The distributions are given in arbitrary units with the largest colour value corresponding to the largest peak at respective time t_n in columns (a) and (b), while the largest colour value in columns (c) and (d) corresponds to the largest peak at time $t_{\text{fin}} = 200 \cdot \gamma^{-1}$.

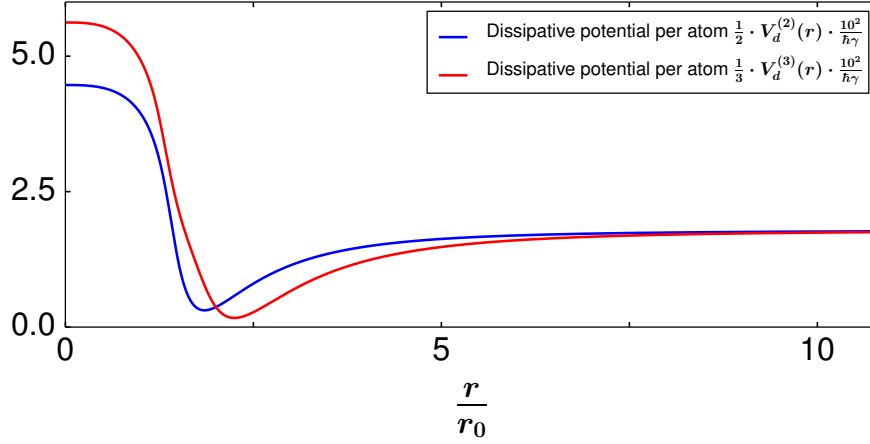


Figure C.13.: The effective dissipative n -atom potentials per atom $\frac{1}{n}V_d^{(n)}(r)$ with Borromean parameter values are displayed for $n = 2$ and $n = 3$. $\frac{1}{3}V_d^{(3)}(r)$ was calculated assuming an equilateral triangle configuration. Parameter values used are listed in Tab. 6.1.

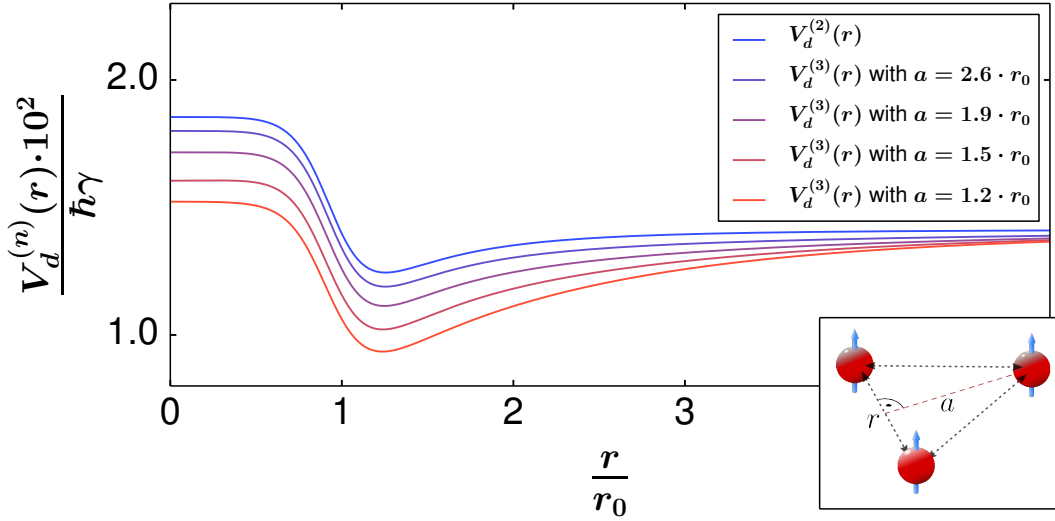


Figure C.14.: The effective dissipative n -atom potentials $V_d^{(n)}(r)$ are displayed for $n = 2$ and $n = 3$ with restricted geometric configurations. While the blue curve shows $V_d^{(2)}(r)$ for two atoms separated by distance r , the other curves show $V_d^{(3)}(r)$ for three atoms in the constellation indicated in the bottom right image. For better comparison, all curves of $V_d^{(3)}(r)$ are shifted by an isolated atom's dissipation rate $-V_d^{(3)}(\infty)/3$. The following parameter values were used: $\Omega_{21} = 0.75 \cdot \gamma$, $\Delta_{21} = 0.15 \cdot \gamma$, $\Omega_{23} = 0.35 \cdot \gamma$, $\Delta_{23} = 0$, and $d = 5.9$ D.

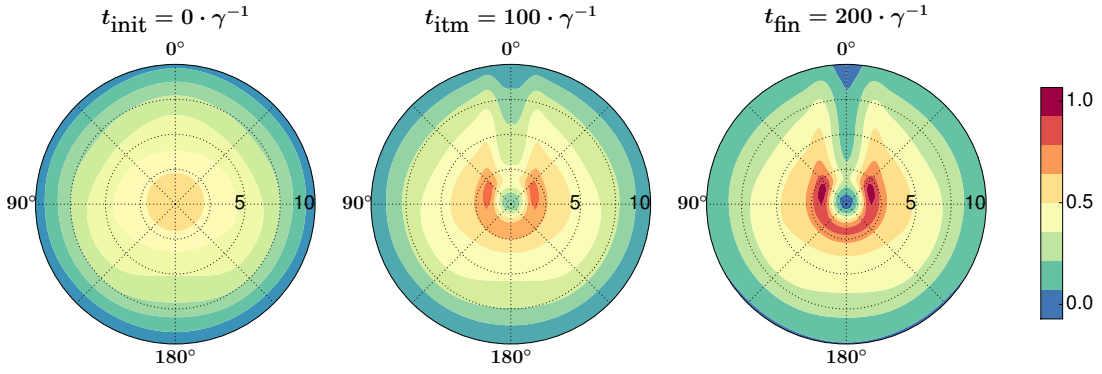


Figure C.15.: The plots of the averaged three-atom probability distribution with Borromean parameter values (see Tab. 6.1) are shown in the isosceles configuration at times t_{init} , t_{itm} , and t_{fin} . The radial axis represents interatomic distances $r_{21} = r_{31} = r$ divided by r_0 , whereas the polar axis indicates opening angle Θ . The distributions are given in arbitrary units with the largest value corresponding to the largest peak of the distribution at time t_{fin} .

List of Symbols and Abbreviations

\hbar	Planck constant
ϵ_0	vacuum permittivity
m	caesium mass
n_a	number of atoms in the examined system
d	electric dipole moment
r_0	characteristic length of the dipole-dipole interaction
$U^{(n_a)}$	n_a -atom dipole-dipole interaction
r_{ij}	distance between atoms i and j
Θ	opening angle of the triangular atom-configuration
$\hat{\mathbf{r}}_a$	position operator of atom a
$\hat{\mathbf{k}}_a$	momentum operator of atom a
$ x\rangle_a$	representation of atom a being in state x
$ x, y\rangle$	representation of atoms a, b being in states x, y
$ x, y, z\rangle$	representation of atoms a, b, c being in states x, y, z
ω	frequency of a transition
Ω	Rabi frequency of a transition
Δ	laser detuning of a transition
γ	rate of decay of a transition
$\hat{H}^{(n_a)}$	n_a -atom Hamiltonian operator
$H^{(n_a)}$	n_a -atom Hamiltonian matrix
$\hat{\rho}$	density operator
ρ	density matrix
\hat{c}_n	jump operator of decay channel n
$\mathcal{L}(\hat{\rho})$	Lindbladian superoperator

$V_d^{(n_a)}$	effective dissipative n_a -atom potential
$\Delta V_d^{(n_a)}$	depth of the dissipative n_a -atom potential
$V_d^{(n_a)}(0)$	asymptotic value of $V_d^{(n_a)}$ at 0
$V_d^{(n_a)}(\infty)$	asymptotic value of $V_d^{(n_a)}$ at ∞
δt	time-increment in the MC algorithm
δp	decay probability in the MC algorithm
t_{init}	initial time of the simulation
t_{itm}	intermediate time of the simulation
t_{fin}	final time of the simulation
CPT	C oherent P opulation C ontrol
EIT	E lectromagnetically I nduced T ransparency
MC	M onte C arlo
MCWF	M onte C arlo W ave- F unction

List of Figures

2.1.	Schematics of the one-dimensional two-atom system: two atoms in an optical trap while laser beams drive the electronic transitions.	4
2.2.	(a) Representation of the two-atom system in two dimensions. (b) Representation of the three-atom system in two dimensions . .	4
2.3.	The electronic energy structure of one of the atoms arranged in a Λ -system with all relevant system parameters.	6
2.4.	Three-level atom in a Λ -configuration interacting with two resonant fields of frequencies ω_1 and ω_2	7
3.1.	A generic two-atom wave-function $\psi(r, t) = \langle r \psi(t) \rangle$ is shown before and after a some time Δt	15
3.2.	The electronic energy structure for two-atoms: Dipole-dipole interaction $U^{(2)}(r)$ results in a distance-dependent detuning $\tilde{\Delta}_{21}(r)$.	17
4.1.	The curve of $V_d^{(2)}(r)$ is shown for different sets of parameter values with varying detunings Δ_{21} and Δ_{23}	26
4.2.	The curve of $V_d^{(2)}(r)$ is shown for different sets of parameter values with varying Rabi frequencies Ω_{21} and Ω_{23}	27
4.3.	The dissipative two-atom potential $V_d^{(2)}(r)$ with optimised parameter values and the conservative dipole-dipole interaction $U^{(2)}(r)$ are shown.	28
4.4.	Real and imaginary part of the two-atom grey states' eigenvalue $\epsilon_{\text{grey}}^{(2)}$ are shown.	29
4.5.	Dissipative and conservative populations of the two-atom grey state $ \psi_{\text{grey}}^{(2)}\rangle$ are shown.	30
4.6.	The averaged two-atom probability distribution in relative x- and y-coordinates at time $t_{\text{init}} = 0 \cdot \gamma^{-1}$ is shown.	30
4.7.	The averaged two-atom probability distribution in relative x- and y-coordinates at time $t_{\text{itm}} = 100 \cdot \gamma^{-1}$ is shown.	31
4.8.	The averaged two-atom probability distributions in relative x- and y-coordinates at time t_{init} and at time t_{fin} are shown.	32
4.9.	The two-atom pair correlation function $g^{(2)}(r)$ of the two-atom system is shown with optimised parameters at increasing times. .	33
5.1.	The curve of $V_d^{(3)}(r)$ is shown for different sets of parameter values with varying detunings Δ_{21} and Δ_{23}	36

5.2.	The curve of $V_d^{(3)}(r)$ is shown for different sets of parameter values with varying Rabi frequencies Ω_{21} and Ω_{23}	36
5.3.	The dissipative potential $V_d^{(3)}(r)$ for the optimised parameter values and the conservative dipole-dipole interaction $U^{(3)}(r)$ are shown.	37
5.4.	Real and imaginary part of the three-atom grey states' eigenvalue $\epsilon_{\text{grey}}^{(3)}$ are shown.	38
5.5.	Dissipative and conservative population of the three-atom grey state $ \psi_{\text{grey}}^{(3)}\rangle$ are shown.	38
5.6.	The dissipative potential $V_d^{(3)}(r_{21}, r_{31}, \Theta)$: subpanel (a) corresponds to $\Theta = 15^\circ$, while subpanel (b) corresponds to $\Theta = 30^\circ$	39
5.7.	The dissipative potential $V_d^{(3)}(r_{21}, r_{31}, \Theta)$: subpanel (a) corresponds to $\Theta = 60^\circ$, while subpanel (b) corresponds to $\Theta = 120^\circ$	40
5.8.	The averaged three-atom probability distribution in absolute interatomic distances at time t_{init} is shown.	41
5.9.	The averaged three-atom probability distribution in absolute interatomic distances at time t_{itm} is shown.	41
5.10.	The averaged three-atom probability distributions in absolute interatomic distances at times t_{init} and time t_{fin} are shown.	42
5.11.	The function $g^{(3)}(r)$ of the simulated three-atom system with optimised parameters at increasing times is shown.	43
5.12.	The plots of the averaged three-atom probability distribution with optimised parameter values are shown in the isosceles configuration at times t_{init} , t_{itm} , and t_{fin}	44
6.1.	Subpanel (a) depicts a set of Borromean rings. Subpanel (b) shows the crystal structure of a set of molecular Borromean rings.	46
6.2.	The effective dissipative n -atom potentials $V_d^{(n)}(r)$ with Borromean parameter values are displayed for $n = 2$ and $n = 3$	47
6.3.	The averaged three-atom probability distributions in absolute interatomic distances at times t_{init} and time t_{fin} are shown.	49
6.4.	The averaged two-atom probability distributions in relative x- and y-coordinates at time t_{init} and at time t_{fin} are shown.	50
A.1.	Two-level system driven with frequency ω and detuning δ	53
C.1.	The two-atom probability distribution with optimised parameter values is shown at increasing times t_n	60
C.2.	The three-atom probability distributions with optimised parameter values are shown at initial time t_{init} and at time t_1	61
C.3.	The three-atom probability distributions with optimised parameter values are shown at time t_2 and at time t_3	61
C.4.	The three-atom probability distributions with optimised parameter values are shown at time t_4 and at intermediate time t_{itm}	62

C.5. The three-atom probability distributions with optimised parameter values are shown at time t_6 and at time t_7	62
C.6. The three-atom probability distributions with optimised parameter values are shown at time t_8 and at time t_9	63
C.7. The three-atom probability distributions with Borromean parameter values are shown at initial time t_{init} and at time t_1	63
C.8. The three-atom probability distributions with Borromean parameter values are shown at time t_2 and at time t_3	64
C.9. The three-atom probability distributions with Borromean parameter values are shown at time t_4 and at intermediate time t_{itm} . . .	64
C.10. The three-atom probability distributions with Borromean parameter values are shown at time t_6 and at time t_7	65
C.11. The three-atom probability distributions with Borromean parameter values are shown at time t_8 and at time t_9	65
C.12. The two-atom probability distribution with Borromean parameters is shown at increasing times t_n	66
C.13. The effective dissipative n -atom potentials per atom $\frac{1}{n}V_d^{(n)}(r)$ with Borromean parameter values are displayed for $n = 2$ and $n = 3$. . .	67
C.14. The effective dissipative n -atom potentials $V_d^{(n)}(r)$ are displayed at restricted geometric configurations.	67
C.15. The plots of the averaged three-atom probability distribution with Borromean parameter values are shown in the isosceles configuration at times t_{init} , t_{itm} , and t_{fin}	68

List of Tables

4.1.	Parameter values for the different graphs of $V_d^{(2)}(r)$ shown in Fig. 4.1 and of $V_d^{(3)}(r)$ shown in Fig. 5.1.	26
4.2.	Parameter values for the different graphs of $V_d^{(2)}(r)$ shown in Fig. 4.2 and of $V_d^{(3)}(r)$ shown in Fig. 5.2.	28
4.3.	Optimised parameter values for the dimer state.	28
4.4.	Important quantities of $V_d^{(2)}(r)$ with optimised parameter values.	29
5.1.	Optimised parameter values for the trimer state.	37
5.2.	Important quantities of $V_d^{(3)}(r)$ with optimised parameter values.	37
6.1.	Parameter values optimised for the Borromean state.	47
6.2.	Important quantities of $V_d^{(2)}(r)$ and $V_d^{(3)}(r)$ for Borromean parameter values.	48
6.3.	Important quantities of $V_d^{(2)}(r)$ and $V_d^{(3)}(r)$ calculated per atom for Borromean parameter values.	48
B.1.	Essential caesium properties.	57
B.2.	Optical properties of the caesium D_2 transition.	57

Bibliography

- [1] J. D. Hunter. „Matplotlib: A 2D graphics environment“. In: *Computing In Science & Engineering* 9.3 (2007), pp. 90–95.
- [2] L. Carroll. *Alice’s Adventures in Wonderland and Through the Looking-Glass*. London: Penguin Classics, 2003.
- [3] I. Bloch, J. Dalibard, and W. Zwerger. „Many-body physics with ultracold gases“. In: *Rev. Mod. Phys.* 80 (3 July 2008), pp. 885–964. DOI: 10.1103/RevModPhys.80.885.
- [4] S. Diehl et al. „Quantum states and phases in driven open quantum systems with cold atoms“. In: *Nat. Phys.* 4.11 (Nov. 2008), pp. 878–883. DOI: 10.1038/nphys1073.
- [5] M. J. Kastoryano, F. Reiter, and A. S. Sørensen. „Dissipative Preparation of Entanglement in Optical Cavities“. In: *Phys. Rev. Lett.* 106 (9 Feb. 2011), p. 090502. DOI: 10.1103/PhysRevLett.106.090502.
- [6] Jan Carl Budich, Peter Zoller, and Sebastian Diehl. „Dissipative preparation of Chern insulators“. In: *Phys. Rev. A* 91 (4 Apr. 2015), p. 042117. DOI: 10.1103/PhysRevA.91.042117.
- [7] Frank Verstraete, Michael M. Wolf, and J. Ignacio Cirac. „Quantum computation and quantum-state engineering driven by dissipation“. In: *Nat. Phys.* 5 (2009), p. 633. DOI: 10.1038/nphys1342.
- [8] Hendrik Weimer et al. „A Rydberg quantum simulator“. In: *Nat. Phys.* 6 (2010), p. 382. DOI: 10.1038/nphys1614.
- [9] S. Diehl et al. „Dissipation-Induced d -Wave Pairing of Fermionic Atoms in an Optical Lattice“. In: *Phys. Rev. Lett.* 105 (22 Nov. 2010), p. 227001. DOI: 10.1103/PhysRevLett.105.227001.
- [10] A. F. Alharbi and Z. Ficek. „Deterministic creation of stationary entangled states by dissipation“. In: *Phys. Rev. A* 82 (5 Nov. 2010), p. 054103. DOI: 10.1103/PhysRevA.82.054103.
- [11] Hanna Krauter et al. „Entanglement Generated by Dissipation and Steady State Entanglement of Two Macroscopic Objects“. In: *Phys. Rev. Lett.* 107 (8 Aug. 2011), p. 080503. DOI: 10.1103/PhysRevLett.107.080503.
- [12] Gentaro Watanabe and Harri Mäkelä. „Dissipation-induced squeezing“. In: *Phys. Rev. A* 85 (2 Feb. 2012), p. 023604. DOI: 10.1103/PhysRevA.85.023604.

- [13] D. D. Bhaktavatsala Rao and Klaus Mølmer. „Dark Entangled Steady States of Interacting Rydberg Atoms“. In: *Phys. Rev. Lett.* 111 (3 July 2013), p. 033606. DOI: 10.1103/PhysRevLett.111.033606.
- [14] A. W. Carr and M. Saffman. „Preparation of Entangled and Antiferromagnetic States by Dissipative Rydberg Pumping“. In: *Phys. Rev. Lett.* 111 (3 July 2013), p. 033607. DOI: 10.1103/PhysRevLett.111.033607.
- [15] Hendrik Weimer. „Quantum simulation of many-body spin interactions with ultracold polar molecules“. In: *Mol. Phys.* 111.12-13 (2013), pp. 1753–1758. DOI: 10.1080/00268976.2013.789567.
- [16] B. Kraus et al. „Preparation of entangled states by quantum Markov processes“. In: *Phys. Rev. A* 78 (4 Oct. 2008), p. 042307. DOI: 10.1103/PhysRevA.78.042307.
- [17] D. Witthaut, F. Trimborn, and S. Wimberger. „Dissipation Induced Coherence of a Two-Mode Bose-Einstein Condensate“. In: *Phys. Rev. Lett.* 101 (20 Nov. 2008), p. 200402. DOI: 10.1103/PhysRevLett.101.200402.
- [18] Sebastian Diehl et al. „Topology by dissipation in atomic quantum wires“. In: *Nat. Phys.* 7.12 (Dec. 2011), pp. 971–977. DOI: 10.1038/nphys2106.
- [19] G. Kordas, S. Wimberger, and D. Witthaut. „Dissipation-induced macroscopic entanglement in an open optical lattice“. In: *Europhys. Lett.* 100.3 (2012), p. 30007.
- [20] A. Bermudez, T. Schaetz, and M. B. Plenio. „Dissipation-Assisted Quantum Information Processing with Trapped Ions“. In: *Phys. Rev. Lett.* 110 (11 Mar. 2013), p. 110502. DOI: 10.1103/PhysRevLett.110.110502.
- [21] Angelo Lucia et al. „Rapid mixing and stability of quantum dissipative systems“. In: *Phys. Rev. A* 91 (4 Apr. 2015), p. 040302. DOI: 10.1103/PhysRevA.91.040302.
- [22] Julio T. Barreiro et al. „An open-system quantum simulator with trapped ions“. In: *Nature* 470.7335 (Feb. 24, 2011), pp. 486–491. DOI: 10.1038/nature09801.
- [23] Julio T. Barreiro et al. „Experimental multiparticle entanglement dynamics induced by decoherence“. In: *Nat. Phys.* 6.12 (Dec. 2010), pp. 943–946. DOI: 10.1038/nphys1781.
- [24] R. Gommers, S. Bergamini, and F. Renzoni. „Dissipation-Induced Symmetry Breaking in a Driven Optical Lattice“. In: *Phys. Rev. Lett.* 95 (7 Aug. 2005), p. 073003. DOI: 10.1103/PhysRevLett.95.073003.
- [25] Hanna Krauter et al. „Entanglement Generated by Dissipation and Steady State Entanglement of Two Macroscopic Objects“. In: *Phys. Rev. Lett.* 107 (8 Aug. 2011), p. 080503. DOI: 10.1103/PhysRevLett.107.080503.

-
- [26] P. Schindler et al. „Quantum simulation of dynamical maps with trapped ions“. In: *Nat. Phys.* 9.6 (June 2013), pp. 361–367. DOI: 10.1038/nphys2630.
- [27] Philipp Schindler et al. „A quantum information processor with trapped ions“. In: *New J. Phys.* 15.12 (2013), p. 123012.
- [28] Y. Lin et al. „Dissipative production of a maximally entangled steady state of two quantum bits“. In: *Nature* 504.7480 (Dec. 19, 2013), pp. 415–418. DOI: 10.1038/nature12801.
- [29] S. Shankar et al. „Autonomously stabilized entanglement between two superconducting quantum bits“. In: *Nature* 504.7480 (Dec. 19, 2013), pp. 419–422. DOI: 10.1038/nature12802.
- [30] C. Ates et al. „Dissipative Binding of Lattice Bosons through Distance-Selective Pair Loss“. In: *Phys. Rev. Lett.* 109 (23 Dec. 2012), p. 233003. DOI: 10.1103/PhysRevLett.109.233003.
- [31] Johannes Otterbach and Mikhail Lemeshko. „Dissipative Preparation of Spatial Order in Rydberg-Dressed Bose-Einstein Condensates“. In: *Phys. Rev. Lett.* 113 (7 Aug. 2014), p. 070401. DOI: 10.1103/PhysRevLett.113.070401.
- [32] M. Lemeshko and H. Weimer. „Dissipative Binding of Atoms by Non-Conservative Forces“. In: *Nat. Commun.* 4 (2013), p. 2230. DOI: 10.1038/ncomms3230.
- [33] M. Lemeshko. „Manipulating Scattering of Ultracold Atoms with Light-Induced Dissipation“. In: *Front. Phys.* 1.17 (2013), pp. 1–6. DOI: 10.3389/fphy.2013.00017.
- [34] I. Newton. *Philosophiae Naturalis Principia Mathematica*. Ed. by I. B. Cohen and A. Whitman. 3rd. Berkeley, CA: University of California Press, 1726.
- [35] H.-W. Hammer, A. Nogga, and A. Schwenk. „Colloquium: Three-body forces: From cold atoms to nuclei“. In: *Rev. Mod. Phys.* 85 (1 Jan. 2013), pp. 197–217. DOI: 10.1103/RevModPhys.85.197.
- [36] D. Blume. „Few-body physics with ultracold atomic and molecular systems in traps“. In: *Rep. Prog. Phys.* 75.4 (2012), p. 046401.
- [37] E. Epelbaum, H.-W. Hammer, and Ulf-G. Meißner. „Modern theory of nuclear forces“. In: *Rev. Mod. Phys.* 81 (4 Dec. 2009), pp. 1773–1825. DOI: 10.1103/RevModPhys.81.1773.
- [38] J. Dobnikar et al. „Three-body interactions in colloidal systems“. In: *Phys. Rev. E* 69 (3 Mar. 2004), p. 031402. DOI: 10.1103/PhysRevE.69.031402.
- [39] Henning Heiselberg and Morten Hjorth-Jensen. „Phases of dense matter in neutron stars“. In: *Physics Reports* 328.5–6 (2000), pp. 237–327. DOI: [http://dx.doi.org/10.1016/S0370-1573\(99\)00110-6](http://dx.doi.org/10.1016/S0370-1573(99)00110-6).

- [40] E. Fradkin et al. „A Chern-Simons effective field theory for the Pfaffian quantum Hall state“. In: *Nuclear Physics B* 516.3 (1998), pp. 704–718. DOI: [http://dx.doi.org/10.1016/S0550-3213\(98\)00111-4](http://dx.doi.org/10.1016/S0550-3213(98)00111-4).
- [41] N. R. Cooper. „Exact Ground States of Rotating Bose Gases Close to a Feshbach Resonance“. In: *Phys. Rev. Lett.* 92 (22 June 2004), p. 220405. DOI: [10.1103/PhysRevLett.92.220405](https://doi.org/10.1103/PhysRevLett.92.220405).
- [42] Arkadiusz Wójs, Csaba Tóke, and Jainendra K. Jain. „Global Phase Diagram of the Fractional Quantum Hall Effect Arising from Repulsive Three-Body Interactions“. In: *Phys. Rev. Lett.* 105 (19 Nov. 2010), p. 196801. DOI: [10.1103/PhysRevLett.105.196801](https://doi.org/10.1103/PhysRevLett.105.196801).
- [43] Chetan Nayak et al. „Non-Abelian anyons and topological quantum computation“. In: *Rev. Mod. Phys.* 80 (3 Sept. 2008), pp. 1083–1159. DOI: [10.1103/RevModPhys.80.1083](https://doi.org/10.1103/RevModPhys.80.1083).
- [44] H. P. Buchler, A. Micheli, and P. Zoller. „Three-body interactions with cold polar molecules“. In: *Nat. Phys.* 3.10 (Oct. 2007), pp. 726–731. DOI: [10.1038/nphys678](https://doi.org/10.1038/nphys678).
- [45] Xinhua Peng et al. „Quantum Simulation of a System with Competing Two- and Three-Body Interactions“. In: *Phys. Rev. Lett.* 103 (14 Sept. 2009), p. 140501. DOI: [10.1103/PhysRevLett.103.140501](https://doi.org/10.1103/PhysRevLett.103.140501).
- [46] A. Bermudez, D. Porras, and M. A. Martin-Delgado. „Competing many-body interactions in systems of trapped ions“. In: *Phys. Rev. A* 79 (6 June 2009), p. 060303. DOI: [10.1103/PhysRevA.79.060303](https://doi.org/10.1103/PhysRevA.79.060303).
- [47] R. Faoro et al. „Borromean three-body FRET in frozen Rydberg gases“. In: *Nat. Commun.* 6 (Sept. 8, 2015). Article. DOI: [10.1038/ncomms9173](https://doi.org/10.1038/ncomms9173).
- [48] M. Kiffner, W. Li, and D. Jaksch. „Three-body Bound States in Dipole-Dipole Interacting Rydberg Atoms“. In: *Phys. Rev. Lett.* 111 (2013), pp. 1–5. DOI: [10.1103/PhysRevLett.111.233003](https://doi.org/10.1103/PhysRevLett.111.233003).
- [49] C. Mao, W. Sun, and N. C. Seeman. „Assembly of Borromean rings from DNA“. In: *Nature* 386.6621 (Mar. 13, 1997), pp. 137–138. DOI: [10.1038/386137b0](https://doi.org/10.1038/386137b0).
- [50] K. S. Chichak et al. „Molecular Borromean Rings“. In: *Science* 304.5675 (2004), pp. 1308–1312. DOI: [10.1126/science.1096914](https://doi.org/10.1126/science.1096914).
- [51] P. Cromwell, E. Beltrami, and M. Rampichini. „The Borromean Rings“. In: *Math. Intelligencer* 20.1 (1998), pp. 53–62.
- [52] V. Efimov. „Energy levels arising from resonant two-body forces in a three-body system“. In: *Phys. Lett. B* 33 (Dec. 1970), pp. 563–564. DOI: [10.1016/0370-2693\(70\)90349-7](https://doi.org/10.1016/0370-2693(70)90349-7).
- [53] T. Kraemer et al. „Evidence for Efimov quantum states in an ultracold gas of caesium atoms“. In: *Nature* 440.7082 (Mar. 16, 2006), pp. 315–318. DOI: [10.1038/nature04626](https://doi.org/10.1038/nature04626).

-
- [54] M. Kunitski et al. „Observation of the Efimov state of the helium trimer“. In: *Science* 348.6234 (2015), pp. 551–555. DOI: 10.1126/science.aaa5601.
- [55] Shih-Kuang Tung et al. „Geometric Scaling of Efimov States in a ${}^6\text{Li}$ - ${}^{133}\text{Cs}$ Mixture“. In: *Phys. Rev. Lett.* 113 (24 Dec. 2014), p. 240402. DOI: 10.1103/PhysRevLett.113.240402.
- [56] R. Pires et al. „Observation of Efimov Resonances in a Mixture with Extreme Mass Imbalance“. In: *Phys. Rev. Lett.* 112 (25 June 2014), p. 250404. DOI: 10.1103/PhysRevLett.112.250404.
- [57] B. Huang, L. A. Sidorenkov, and R. Grimm. „Finite-temperature effects on a triatomic Efimov resonance in ultracold cesium“. In: *Phys. Rev. A* 91 (6 June 2015), p. 063622. DOI: 10.1103/PhysRevA.91.063622.
- [58] A. Zenesini et al. „Resonant atom-dimer collisions in cesium: Testing universality at positive scattering lengths“. In: *Phys. Rev. A* 90 (2 Aug. 2014), p. 022704. DOI: 10.1103/PhysRevA.90.022704.
- [59] Bo Huang et al. „Observation of the Second Triatomic Resonance in Efimov’s Scenario“. In: *Phys. Rev. Lett.* 112 (19 May 2014), p. 190401. DOI: 10.1103/PhysRevLett.112.190401.
- [60] E. A. Abbott. *Flatland*. Minelva, NY: Dover Publications, 1992.
- [61] M. Fleischhauer, A. Imamoglu, and J. Marangos. „Electromagnetically Induced Transparency: Optics in Coherent Media“. In: *Rev. Mod. Phys.* 77.1997 (2005), pp. 633–673. DOI: 10.1103/RevModPhys.77.633.
- [62] M. O. Scully and M. S. Zubairy. *Quantum Optics*. 6th ed. Cambridge: Cambridge University Press, 2008.
- [63] L. E. Ballentine. *Quantum Mechanics. A Modern Development*. 2nd ed. Singapore: World Scientific, 2014.
- [64] C Cohen-Tannoudji, B. Diu, and F. Laloe. *Quantum Mechanics. Volume One*. 1st ed. Weinheim: Wiley-VCH, 1991.
- [65] C Cohen-Tannoudji, B. Diu, and F. Laloe. *Quantum Mechanics. Volume Two*. 1st ed. Weinheim: Wiley-VCH, 1991.
- [66] H. Schempp et al. „Coherent Population Trapping with Controlled Interparticle Interactions“. In: *Phys. Rev. Lett.* 104 (17 Apr. 2010), p. 173602. DOI: 10.1103/PhysRevLett.104.173602.
- [67] J. D. Pritchard et al. „Cooperative Atom-Light Interaction in a Blockaded Rydberg Ensemble“. In: *Phys. Rev. Lett.* 105 (19 Nov. 2010), p. 193603. DOI: 10.1103/PhysRevLett.105.193603.
- [68] J. Nipper et al. „Highly Resolved Measurements of Stark-Tuned Förster Resonances between Rydberg Atoms“. In: *Phys. Rev. Lett.* 108 (11 Mar. 2012), p. 113001. DOI: 10.1103/PhysRevLett.108.113001.

- [69] Robert Löw et al. „An experimental and theoretical guide to strongly interacting Rydberg gases“. In: *Journal of Physics B: Atomic, Molecular and Optical Physics* 45.11 (2012), p. 113001.
- [70] Thibault Peyronel et al. „Quantum nonlinear optics with single photons enabled by strongly interacting atoms“. In: *Nature* 488.7409 (Aug. 2012), pp. 57–60. DOI: 10.1038/nature11361.
- [71] Peter Schausz et al. „Observation of spatially ordered structures in a two-dimensional Rydberg gas“. In: *Nature* 491.7422 (Nov. 1, 2012), pp. 87–91. DOI: 10.1038/nature11596.
- [72] Y. O. Dudin and A. Kuzmich. „Strongly Interacting Rydberg Excitations of a Cold Atomic Gas“. In: *Science* 336.6083 (2012), pp. 887–889. DOI: 10.1126/science.1217901.
- [73] N. Henkel, R. Nath, and T. Pohl. „Three-Dimensional Roton Excitations and Supersolid Formation in Rydberg-Excited Bose-Einstein Condensates“. In: *Phys. Rev. Lett.* 104 (19 May 2010), p. 195302. DOI: 10.1103/PhysRevLett.104.195302.
- [74] G. Pupillo et al. „Strongly Correlated Gases of Rydberg-Dressed Atoms: Quantum and Classical Dynamics“. In: *Phys. Rev. Lett.* 104 (22 June 2010), p. 223002. DOI: 10.1103/PhysRevLett.104.223002.
- [75] J. Honer et al. „Collective Many-Body Interaction in Rydberg Dressed Atoms“. In: *Phys. Rev. Lett.* 105 (16 Oct. 2010), p. 160404. DOI: 10.1103/PhysRevLett.105.160404.
- [76] A. Rauschenbeutel et al. *FUNDAMENTALS OF QUANTUM OPTICS: Interaction of light with atoms*. University Lecture. 2013.
- [77] B. Russell. *An Outline of Philosophy*. 1st ed. London/New York: Routledge, 2009.
- [78] F. Schwabl. *Statistische Mechanik*. 3rd ed. Berlin: Springer, 2006.
- [79] Philip Pearle. „Simple derivation of the Lindblad equation“. In: *European Journal of Physics* 33.4 (2012), p. 805.
- [80] Klaus Mølmer, Yvan Castin, and Jean Dalibard. „Wave-function approach to dissipative processes in quantum optics“. In: *Phys. Rev. Lett.* 68 (5 Feb. 1992), pp. 580–583. DOI: 10.1103/PhysRevLett.68.580.
- [81] Klaus Mølmer, Yvan Castin, and Jean Dalibard. „Monte Carlo wave-function method in quantum optics“. In: *J. Opt. Soc. Am. B* 10.3 (Mar. 1993), pp. 524–538. DOI: 10.1364/JOSAB.10.000524.
- [82] J. E. Lennard-Jones. „On the Determination of Molecular Fields. II. From the Equation of State of a Gas“. In: *Proc. Roy. Soc. A* 106 (1924), pp. 463–477. DOI: 10.1098/rspa.1924.0082.
- [83] V. Borge. *Smilet er den korteste afstand...* Copenhagen: Gyldendal, 2001.

-
- [84] F. Schiller. *Gedichte*. Leipzig: Reclam-Verlag, 1999.
- [85] Wikipedia. *Molecular Borromean rings* — *Wikipedia, The Free Encyclopedia*. Accessed: 2016-09-01. 2016. URL: https://en.wikipedia.org/wiki/Borromean_rings.
- [86] F. Nietzsche. *Der Wanderer und sein Schatten*. Paderborn: Salzwasser Verlag, 2011.
- [87] Scott E. Pollack, Daniel Dries, and Randall G. Hulet. „Universality in Three- and Four-Body Bound States of Ultracold Atoms“. In: *Science* 326.5960 (2009), pp. 1683–1685. DOI: 10.1126/science.1182840.
- [88] Amy N. Nicholson. „*N*-Body Efimov States from Two-Particle Noise“. In: *Phys. Rev. Lett.* 109 (7 Aug. 2012), p. 073003. DOI: 10.1103/PhysRevLett.109.073003.
- [89] A. N. Wenz et al. „From Few to Many: Observing the Formation of a Fermi Sea One Atom at a Time“. In: *Science* 342.6157 (2013), pp. 457–460. DOI: 10.1126/science.1240516.
- [90] NikolajThomas Zinner. „Few-Body Physics in a Many-Body World“. English. In: *Few-Body Systems* 55.8-10 (2014), pp. 599–604. DOI: 10.1007/s00601-014-0802-x.
- [91] N. T. Zinner. „Exploring the few- to many-body crossover using cold atoms in one dimension“. In: *ArXiv e-prints* (Oct. 2015). arXiv: 1510.03619 [quant-ph].
- [92] Daniel Steck. *Cesium D line data*. <http://steck.us/alkalidata/cesiumnumbers.1.6.pdf>. Accessed: 2016-09-01.

